THERMAL FE ANALYSIS OF POWDER BED FUSION PROCESS: POWER INPUT EVALUATION AND PARAMETER SENSITIVITY

DIEGO AUGUSTO DE MORAES

A THESIS SUBMITTED TO THE FACULTY OF GRADUATE STUDIES

IN PARTIAL FULFILLMENT OF THE REQUIREMENTS

FOR THE DEGREE OF MASTER OF SCIENCE

GRADUATE PROGRAM IN MECHANICAL ENGINEERING

YORK UNIVERSITY

TORONTO, ONTARIO

August 2018

ABSTRACT

We investigated the thermal behavior of the powder bed fusion (PBF) manufacturing process. Specifically, a finite element thermal analysis procedure was developed to simulate selective laser melting, one of several PBF processes available on the market. The primary objective was to study how selected parameters of the PBF process affect temperature distributions, since a high temperature gradient and cooling rate are associated with residual stress and deformation in the built part. Since it was difficult to devise an analytical solution for this transient thermal problem, commercially available finite element analysis software, Abaqus, was employed. Sensitivity analysis was undertaken to analyze the impact of powder diameter, packing density, and substrate temperature on the overall temperature distributions. Finally, verification and validation were performed via experimental setup and data from the literature. The samples built were characterized by residual stress measurements, porosity, and relative density to further validate the model.

ACKNOWLEDGEMENTS

I am grateful that I had the opportunity to be part of the IDEA-Lab team for the past 2 years. First, I would like to thank Dr. Czekanski for selecting me in 2016, for trusting my work and competence, and for providing his financial support and supervision. Without him, I would not have been able to achieve success. Thanks to Claudia Bennett and Julian Bennett for the astonishing work they did editing my manuscripts as well for helping with pretty much anything else. I also thank my fellow graduate friends for the amazing time I had and for their support. I will always remember the joy of being part of graduate office room 403.

I appreciate my collaboration with Dr. Elbestawi and Mr. Yakout of McMaster University, as they both played an extremely important role in my experimental setup.

I spiritually dedicate this thesis to my dear father, Milton Geraldo de Moraes, whose inspiration has driven me throughout my career and studies. May he rest in peace. My mother and sister, Maria de Moraes and Jacqueline Moraes, lent me their strength and supported me during my stay in Canada, as did my dear members of the Moraes family and relatives in Brazil. I am grateful for my beloved friends, especially Ademar Lara, Luiz Otávio, and Iaponaíra de Abreu, for listening to my struggles and giving me golden words of advice, as well for the good old days we enjoyed back in Brazil. Thanks to the members of Casa da Dalva and Diadorim 2.0 for the good (... and bad) jokes. Last but not least, thank you to Wenjuan Li for the love and care you have given through good times and bad.

Finally, I would like to express my gratitude to the Lassonde School of Engineering and the Natural Sciences and Engineering Research Council (NSERC)/Quanser Chair in Design Engineering Program for providing financial support.

TABLE OF CONTENTS

Abstract ii
Acknowledgements iii
Table of Contents v
List of Tables viii
List of Figures ix
Acronyms and Notations xv

1 INTRODUCTION AND JUSTIFICATION 1
1.1 Technological Gap and Justification of the Study 2
1.2 Research Objectives 2
1.3 Methodology 4
1.4 Layout of the Thesis 5

2 BACKGROUND AND LITERATURE REVIEW 6
2.1 Additive Manufacturing of Metallic Alloys — An Overview 6
2.2 Selective Laser Melting and Direct Metal Laser Sintering 10
2.3 Limitations of and Technological Gaps in Powder Bed Fusion Processes 12
2.4 The Finite Element Model of Powder Bed Fusion and Experimental Approaches 14

3 POWDER THERMAL PROPERTIES 19
3.1 Powder Packing Density 19
3.1.1 Packing structures 20
3.2 Contact Area and Porosity of the Powder Bed 21
3.3 Material Properties 23
3.4 Powder Emissivity 25
3.5 Effective Thermal Conductivity of Powders 26
3.6 Verification and Conclusions 29

4 FINITE ELEMENT THERMAL MODELING OF SELECTIVE LASER MELTING 31
4.1 Governing Equations 31
4.2 Thermal Model Domain and Finite Element Model 32
4.3 Modeling of Selective Laser Melting Heat Source 34
4.4 Phase Transformation 37
4.5 Parameters of the Simulation 38
4.6 Results 39
4.6.1 Longitudinal and cross-sectional temperature distributions 39
4.6.2 Melt pool behavior for T_0 = 643 K 47
4.6.3 Sensitivity analysis of substrate temperature 51
4.7 Verification and Conclusions 55

5 DIRECT METAL LASER SINTERING EXPERIMENTAL SETUP 59
5.1 Stainless Steel 316L Powder 59
5.2 Designing the Experimental Setup 61
5.2.1 Samples placement in the substrate plate 63
5.3 Manufacturing Process 65
5.4 Density Analysis 68
5.4.1 Results of relative density and porosity analysis 70
5.5 Surface Micrographs 75
5.6 Residual Stress Analysis 81
5.6.1 Results for residual stress analysis 82
5.7 Microstructural Analysis 85
5.8 Conclusion and Discussion 89

6 THESIS SUMMARY AND FUTURE WORK 92
6.1 Thesis Summary and Research Contribution 92
6.2 Research Contributions 96
6.3 Future Research 96

BIBLIOGRAPHY 98

APPENDIX 109
Abaqus Subroutine DFLUX and FILM 109
Input File of Abaqus 110

LIST OF TABLES

Table 2.1. Tensile strength of selected metal alloys produced by SLM [9]. 10

Table 2.2. Configuration of three single laser melting machines (SLM Solutions) [10]..... 11

Table 2.3. Configuration of four direct metal laser sintering machines (EOS GmbH) [17]..... 11

Table 3.1. Comparison of effective thermal conductivity from Kovalev and Gusarov [50], Alkahari et al. [60], and the current work. 30

Table 4.1. Parameters of the selective laser melting simulation. 38

Table 4.2. Temperature in the last five time increments at –75 μm and P = 200 W for simple cubic (SC) packing density. 43

Table 4.3. Temperature gradients (∇T) and maximum temperature (T_{Max}; in kelvin) for all simulated substrate and power conditions. 55

Table 5.1. Chemical composition of EOS stainless steel 316L [17]. 59

Table 5.2. Range of parameters for the EOS M280 3D printer [17]. 62

Table 5.3. Common parameters applied for SS-316L using direct metal laser sintering. 62

Table 5.4. Designed range of parameters and groups. 63

LIST OF FIGURES

Figure 2.1. Selective laser sintering method patented in 1990 by C. Deckard [8]. 7

Figure 2.2. Schematic of selective laser melting. 8

Figure 2.3. Applications of the powder bed fusion process. (a) Research using metal printed metamaterials. Reused with permission of IOP Publishing: *Society of Photo-optical Instrumentation Engineers* [14], Copyright © 2015; (b) GE fuel nozzle [15]; (c) RAMLAB ship propeller [16]; (d) EOS pelvis replacement [17]; (e) tool and die maker with conformal cooling [18]; (f) Siemens turbine blade [19]..... 9

Figure 2.4. The laser heats the powder bed (a) and subsequent cooling occurs (b). Reused by permission from Emerald Publishing Limited: *Rapid Prototyping Journal* [31]. Copyright © 2006. Delamination and cracking observed on printed samples (c). Reused by permission from AIP Publishing: *Applied Physics Review* [9]. Copyright © 2015. 13

Figure 3.1. Simple cube (SC) packing structure (a), body-centered cubic (BCC) packing structure (b), and face-centered cubic (FCC) packing structure (c)..... 21

Figure 3.2. Particles in the contact region (left) and in the contact radius in detail (right). 22

Figure 3.3. Temperature-dependent density (a), thermal conductivity (b), and specific heat (c) of stainless steel 304L. 24

Figure 3.4. Porosity-dependent emissivity of simple cubic (SC) packing structure, body-centered cubic (BCC) packing structure, and face-centered cubic (FCC) packing structure..... 26

Figure 3.5. Effective thermal conductivity of powder in simple cubic (SC) packing structure, body-centered cubic (BCC) packing structure, and face-centered cubic (FCC) packing structure, with powder particles of 20, 60, and 100 μm diameter..... 28

Figure 4.1. Three-dimensional domain of the model..... 33

Figure 4.2. Different transverse electromagnetic modes for lasers. Reused by permission from Elsevier: *International Journal of Machine Tools and Manufacturing* [71], Copyright © 2009. 35

Figure 4.3. Double-ellipsoidal heat source model. Adapted by permission from Springer Nature: *Metallurgical and Materials Transactions* B [72], Copyright © 1984. 36

Figure 4.4. Static heat flux distribution modeled as a Gaussian profile using the Goldak formulation..... 37

Figure 4.5. Nodal acquisition scheme..... 40

Figure 4.6. Temperature distribution at a power input (*P*) of 100 W during one scan in the scanning direction. 41

Figure 4.7. Temperature distribution at a power input (*P*) of 100 W at the cross-section perpendicular to the laser scanning direction..... 42

Figure 4.8. Temperature distribution at a power input (*P*) of 200 W during one scan in the scanning direction. 44

Figure 4.9. Temperature distribution at a power input (*P*) of 200 W at the cross-section perpendicular to the laser scanning direction..... 45

Figure 4.10. Temperature distribution at a power input (P) of 400 W during one scan in the scanning direction. 46

Figure 4.11. Temperature distribution at a power input (P) of 400 W at the cross-section perpendicular to the laser scanning direction..... 47

Figure 4.12. X–Z cross-section (top) and Y–Z cross-section (bottom)..... 48

Figure 4.13. Melt pool area at 1.5 ms for P = 200 W (a) and P = 400 W (b)..... 48

Figure 4.14. Melt pool dimensions in the last time increment for P = 200 W. X–Y plane (a), X–Z plane (b), and Y–Z plane (c). 49

Figure 4.15. Melt pool dimensions in the last time increment for P = 400 W. X–Z plane (a), X–Y plane (b), and Y–Z plane (c). 50

Figure 4.16. Temperature distribution for T_0 = 298 K at P = 100 W (a), P = 200 W (c), and P =400 W (e) and their corresponding cross-sections in (b), (d), and (f). 53

Figure 4.17. Temperature distribution for T_0 = 373 K at P = 100 W (a), P = 200 W (c), and P =400 W (e) and their corresponding cross-sections in (b), (d), and (f). 54

Figure 5.1. Thermal properties of SS-304L and SS-316L [56]. 60

Figure 5.2. Laser energy density of each sample and layout. 64

Figure 5.3. Set of samples being programmed using EOS 3D printing system (a), the printing process taking place with the laser scanning at the centre (b), and the finished direct metal laser sintering samples on the substrate..... 66

Figure 5.4. Low energy density samples (a), high energy density samples (b), and "bumper" detail on the high energy density samples (c). 67

Figure 5.5. High laser energy density sample with surface deformation and oxide layer on samples G4A1 (a) and G1B3 (b); normal surface printed sample G3B2 with lower laser energy density (c). 68

Figure 5.6. Scale used to measure the mass of the samples and consequently their densities. 69

Figure 5.7. Relative density of the samples versus the laser energy density. 70

Figure 5.8. Relative density of the samples varied according to laser energy density. Samples were grouped according to power input, with groups designated as 1 (P = 150 W) (a), 2 (P = 200 W) (b), and 3 (P = 250 W) (c)..... 71

Figure 5.9. Relative density of the samples varied according to laser energy density. Samples were grouped according to scanning speed, with groups designated as A (v = 250 mm/s) (a), B (v = 750 mm/s) (b), C (v = 1250 mm/s) (c), and D (v = 1750 mm/s) (d). 71

Figure 5.10. Relative density of the samples varied according to laser energy density. Samples were grouped according to hatching distance, with groups designated as G1 (s = 80 µm) (a), G2 (s = 100 µm) (b), G3 (s = 120 µm) (c), and G4 (s = 140 µm) (d). 72

Figure 5.11. Relative density versus laser energy density for hatch distance (a), scanning speed (b), and power input (c). 73

Figure 5.12. Micrographs of the top surface after polishing samples G1B1 (a) and G4D1 (b). 74

Figure 5.13. Porosity versus laser energy density of the samples. 75

Figure 5.14. As-built micrographs of the top surface with same scanning speed (750 mm/s) and power input (250 W), varying the hatch distance from 80 to 140 µm..... 76

Figure 5.15. As-built micrographs of the top surface with same scanning speed (1250 mm/s) and hatch distance (100 µm), varying the power input from 150 to 250 W..... 77

Figure 5.16. As-built micrographs of the top surface with same power input (150 W) and hatch distance (120 µm), varying the scanning speed from 250 to 1750 mm/s. 79

Figure 5.17. As-built micrographs of the top surface with same power input (200 W) and scanning speed (1750 mm/s), varying the hatch distance from 80 to 140 µm..... 80

Figure 5.18. Measurement location of residual stresses in a sample. 82

Figure 5.19. Residual stresses measured at the side of the sample's surface versus laser energy density. 83

Figure 5.20. Residual stress measurements for scanning speed groups versus hatch distance. Maximum principal stresses (a) and minimum principal stresses (b)..... 83

Figure 5.21. Residual stress measurements for hatch distance groups versus scanning speed. Maximum principal stresses (a) and minimum principal stresses (b)..... 84

Figure 5.22. Residual stress measurements for hatch distance groups versus power input. Maximum principal stresses (a) and minimum principal stresses (b)..... 84

Figure 5.23. Micrograph (magnification 40×) of sample G1B3, with austenite and martensite areas highlighted. 86

Figure 5.24. Micrograph (magnification 40×) of sample G2C2, with austenite and martensite areas highlighted. 87

Figure 5.25. Laser track observed at top surface of sample G2B3. 88

Figure 5.26. Melt pool track observed at side surface of sample G4B1. 88

Figure 5.27. The relationship between relative density behavior and laser energy density. Adapted by permission from Springer Nature: *The International Journal of Advanced Manufacturing Technology* [34], Copyright © 2017. 90

ACRONYMS AND NOTATIONS

AFP	Atomic packing factor
AM	Additive manufacturing
BCC	Body-centered cubic
DMD	Direct metal deposition
DMLS	Direct metal laser sintering
DEM	Discrete element method
EBM	Electron beam melting
FCC	Face-centered cubic
FEM	Finite element model
FDM	Fused deposition modeling
HAZ	Heat affected zone
PBF	Power bed fusion
SLM	Selective laser melting
SLS	Selective laser sintering
SC	Simple cubic
SS-304L	Stainless steel 304L
SS-316L	Stainless steel 316L
P	Power input
v	Scan speed
h	Layer thickness
s	Hatch distance

n_{particle}	Number of particles per unit cell
V_{particle}	Volume of each corresponding particle
$V_{\text{unit cell}}$	Volume of the unit cell
φ	Powder porosity
φ_{final}	Porosity of the built part
N	Coordination number
M	Total number of particles in a domain
k_j	Number of contacts
a	Contact radius
E	Young's modulus
v	Poisson's ratio
F_{N}	Load applied by a roller or scraper
E^*	Material properties constant
x_r	Powder diameter
r	Powder radius
ε_{p}	Effective powder emissivity
ε_{s}	Solid emissivity
ε_{H}	Gap emissivity
A_{H}	Area fraction of the powder surface
k_{eff}	Effective powder thermal conductivity
k_{contact}	Thermal conductivity due to contact between particles
k_{g}	Gas thermal conductivity

k_{s}	Solid thermal conductivity
k_{R}	Thermal conductivity due to radiation
T_{solidus}	Solidus temperature
T_{liquidus}	Liquidus temperature
Λ	Contact fraction
B	Deformation parameter
T	Temperature
$\rho(T)$	Temperature-dependent density
$C_{\mathrm{p}}(T)$	Temperature-dependent heat capacity
$q(r,t)$	Flow rate of heat energy per unit area
$Q(r,t)$	Volumetric heat flux
h_{c}	Convective coefficient
T_0	Substrate temperature
σ	Stefan–Boltzmann constant
q_{rad}	Thermal radiation
q_{conv}	Thermal convection
h	Radiation and convection combined thermal coefficient
$\dot{Q}_{\mathrm{f}(x,y,z)}$	Front volumetric heat flux
$\dot{Q}_{\mathrm{r}(x,y,z)}$	Rear volumetric heat flux
f_{f}	Front heat fraction
f_{r}	Rear heat fraction
a_{f}	Front ellipsoidal parameter

a_{r}	Rear ellipsoidal parameter
b	Side ellipsoidal parameter
c	Depth ellipsoidal parameter
L_{f}	Latent heat of fusion
Δl	Mesh element size
η_{abs}	Absorption coefficient
d_0	Laser spot diameter
t	Time step
E_{v}	Laser energy density
$\nabla T_{x \to y}$	Temperature gradient from x to y
M_1	Sample of mass in air
M_2	Sample of mass immersed in distilled water
ρ_{r}	Relative density
σ_1	Maximum principal residual stresses
σ_2	Minimum principal residual stresses

1 INTRODUCTION AND JUSTIFICATION

Additive manufacturing (AM), commonly referred to as 3D printing or additive layer manufacturing, has become increasingly prominent relative to conventional manufacturing processes. In 2016, according to the Wohlers report, the industry market share of AM surpassed $5 billion USD, growing 25.9% over 2015 figures. Over the past 27 years, the corporate annual growth rate for additive manufacturing has been a sizeable 26.2%, demonstrating the growth potential of this industry compared with that of traditional processes [1]. The rapid growth of AM stems from its versatility, the large number of materials that can be used, and the fast deployment of components after their design has been completed [2].

The term “additive manufacturing” arose in direct contrast to conventional manufacturing processes that have been in use since the 19th century, as the latter are mostly referred to as subtractive manufacturing. While subtractive processes, like milling, involve the removal (subtracting) of material from a working piece until the desired design is complete, additive processes join raw material in a layer-by-layer fashion until the final height is reached. Additive manufacturing, like subtractive manufacturing, refers to several different processes that are mostly classified according to the type of raw material used or by the consolidation phenomena involved [3]. The focus of this research is powder bed fusion (PBF) additive manufacturing — which includes selective laser melting (SLM), direct metal laser sintering (DMLS), and electron beam melting (EBM) — all of which use metallic alloy materials and full melting consolidation phenomena.

1.1 Technological Gap and Justification of the Study

Although AM technologies have grown rapidly, the lack of standardization makes it difficult for most industries to rely on the technology. This is due to the large amount of technologies that are still under patent and the complexity behind them. Technologies such as PBF and fused deposition modeling (FDM) are usually limited to a few applications, owing to the impact of the process parameters on the properties of the final part, which has still not been fully investigated [3]. The overarching objective of this thesis was to implement a low-cost thermal finite element model (FEM) of PBF technology showing (1) the effects of the process parameters on the final temperature distribution of the powder bed during scanning and (2) the impact of the process parameters on the porosity, relative density, and residual stress in the built part. Temperature distribution and cooling rates are key parameters affecting the amount of residual stress in the final part. To achieve this objective, two PBF technologies were analyzed: SLM and DMLS. The model was initially developed for SLM using SS-304L, a low-cost stainless steel alloy that is not yet available for use in PBF processes. Consequently, samples of stainless steel 316 L (SS-316L) manufactured using DMLS were analyzed to characterize the built samples.

1.2 Research Objectives

To achieve the primary objective of this work — a low-cost FEM — the following activities were carried out.

i. Effective thermal conductivity and emissivity of the powders

The thermal conductivity of the powder placed in the bed is different from that of the same material in solid form. In order to account that difference, effective thermal conductivity was

determined; the impact of the packing density and powder diameter was studied as well. Beyond that, surface emissivity, an important parameter to consider when radiation is involved, was also determined for the powder.

ii. Thermal modeling and sensitivity analysis

Numerical analysis using FEM was conducted to characterize thermal distribution in the powder bed. The main focus was to analyze the behavior of the moving heat source in a single track and the impact of its parameters on the temperature gradient in the powder bed. The material utilized was SS-304L, which has not yet been validated for use in the PBF process. The model was constructed using the main parameters of SLM. The sensitivity in the final temperature distribution in the powder bed to power input, powder packing density, powder diameter, and substrate temperature were analyzed.

iii. Experimental setup, residual stress analysis, verification, and validation

The model was validated by performing residual stress analysis, taking a micrograph of the surface, and measuring relative density and analyzing the porosity of samples of SS-316L manufactured by DMLS. Residual stresses in the built part result from a high temperature distribution or cooling rate imposed during the manufacturing process. Validation through temperature readings is not feasible given the high speed of the laser and the high temperature induced in the powder bed, leaving the measurement of residual stress as the more reliable parameter for the model. Further validation was conducted by comparing the simulated melt pool shape with values determined in the experiments.

1.3 Methodology

A comprehensive literature review indicated that the building of a low-cost FEM could be achieved using a parametric thermal model with low computational cost that was able to predict temperature distributions when scanning a single layer and track of a powder bed. Some aspects of the discrete element method (DEM) were implemented, especially those related to thermal conductivity of the powder. We began with the laser power model, using a double-ellipsoidal Gaussian profile as the heat flux input into the FEM. Next, the material was defined, considering the state (solid, liquid, powder) and temperature dependency. Effective thermal conductivity was compiled for the powder under different initial conditions to determine the impact of varying the powder's properties (packing density and powder diameter) on its sensitivity. Different laser power inputs and substrate temperatures were accounted for, and their impact on temperature distributions in the powder bed were analyzed. Particular attention was also paid to the phase change and emissivity of the powder as well. The final model was assembled using SS-304L as the material and simulated for all conditions, leading to the results and analysis sections.

The experimental part of this thesis verifies how well the model can predict the behavior of the temperature distributions. The temperature distributions were not measured using an in situ thermal couple or camera because such a method is inefficient at capturing high-resolution changes in temperature within a small time frame. Instead, samples built using SS-316L were divided into four groups that varied based on three different input parameters (laser speed, power, and hatch distance). Layer thickness, substrate temperature, and scanning strategy were kept constant. The top (scanning direction) and side (build direction) of the samples were analyzed according to their microstructural composition, density, and porosity. Further analysis involved the measurement of

the residual stresses induced in the samples, and these were correlated with the thermal model results previously obtained.

1.4 Layout of the Thesis

The thesis consists of six chapters. The present chapter, **chapter 1**, is a brief introduction. **Chapter 2** provides an in-depth literature review on relevant models and processes, the manufacturing capabilities of PBF, and the technological gaps. In **chapter 3**, we define the material properties of the powder based on Sih and Barlow as well as the analytical approach of Wakao and Kagei, and then compare these values with published research. Next, in **chapter 4** we address the thermal FEM and obtain the temperature distributions for different case scenarios using SLM parameters. **Chapter 5** presents the experimental approach involved in printing samples using the DMLS process and characterizing the samples according to density, final porosity, microstructure, and residual stresses. Finally, in **chapter 6** we conclude the work and propose future research.

2 BACKGROUND AND LITERATURE REVIEW

2.1 Additive Manufacturing of Metallic Alloys — An Overview

AM, or 3D printing, is defined as the process of using raw material in the form of a wire, powder, or liquid to build parts of full or partial density in a layer-by-layer fashion. In the past 38 years, different materials have been employed in this technology. In the early years, polymers such as acrylonitrile butadiene styrene and polycarbonate were used. More recently, the process switched to using powdered or wire metals. Metal AM is being investigated by several researchers and academic institutions, lending significant new insights into how process parameters and physics can affect the final built part. The first developments in this area came with direct metal deposition, laser engineering net shaping, and laser cladding, all of which are highly analogous to thermal spray coating. These are known to be the first AM processes that used metal alloys as a raw material. In this metal AM technique, a powder nozzle provides a successive supply of a metal powder onto a substrate or over a part according to the desired geometry [4]. A high-power laser is responsible for melting the powder that is injected, and the process repeats layer-by-layer until the final height is reached.

After these initial technologies began to be used in the industry, the second wave of technology arrived with the introduction of a new concept — the powder bed process. The first revolutionary approach, selective laser sintering (SLS), came into use in the mid-1980s. SLS was patented by C. Deckard from Texas in 1990 and was the first to be classified as PBF [5]. This process consolidates the metal powder through full or partial melting phenomena. Meanwhile, in Europe, after watching the introduction of the first PBF process in the U.S. market, a partnership between Finland's Electrolux Rapid Development (which supplied the powder metallurgy technology) and EOS

GmbH in Germany (which provided the plastic laser sintering technology) proved to be very successful in competing for this new manufacturing segment [6]. Launched in 1994 and known as DMLS, this technology has been continuously improving to become one of today's state of-the-art processes in metal AM. The name "laser sintering," which applies to both SLS and DMLS, remains controversial, since the process is a full or partial melting, not sintering as the name suggests. According to a terminology standard discussion in "ASTM F2792a Standard Terminology for Additive Manufacturing Technologies" issued in 2012, laser sintering was considered a misnomer [7]. However, the standard was later on withdrawn from the official ASTM listing, and no replacement for it has been provided. Below are the schematics of the process (Figure 2.1) described by C. Deckard.

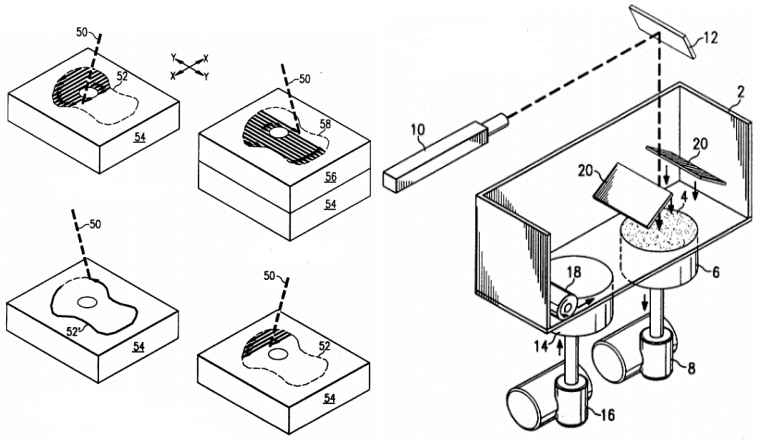

Figure 2.1. Selective laser sintering method patented in 1990 by C. Deckard [8].

Yet another path was pursued by others, given the increased demand for advanced AM processes. This led to the development of SLM in the mid-1990s by F&S Stereolithographietechnik GmbH and Fraunhofer ILT in Germany and the distribution of the process by SLM Solutions [9]. SLM was built on the same basic concepts as SLS, including the use of a bed filled with powder and selective scanning by a high-power laser to solidify each layer

to create a full-density part; however, the solidification step follows the full melting phenomena [10]. Figure 2.2 illustrate the process. Finally, EBM, another process that can use either a powder bed or a metal wire combined with an electric beam, was developed by Arcam in Sweden in the 1990s and launched around 2003. When EBM came onto the scene, it became one more option in the fast-growing AM market [11].

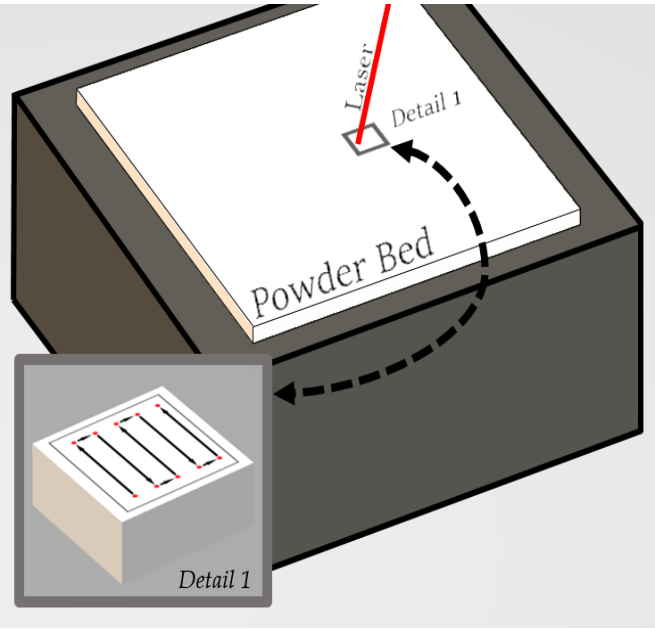

Figure 2.2. Schematic of selective laser melting.

Increasing demand for improvements in AM technology in the 1990s stemmed from the advantages AM has over conventional manufacturing processes. AM processes, such as PBF, can build extremely complex components without the need for tooling. AM technologies were highly applicable to the aerospace, medical, and dental fields; however, the automotive and other engineering sectors benefited as well. Cost savings, shorter time to market, and high degree of freedom are the notable advantages of PBF, but these apply only to a specific high-end market, such as the aerospace and defense sectors [12], [13]. For general applications, however, the low

productivity of PBF leads to a high per-unit manufacturing cost, the definitive factor for choosing a manufacturing process in most scenarios [2]. Though the PBF process uses a very high scanning speed (up to 10 m/s; Table 2.2), its low productivity remains problematic and is commonly attributed to the small spot diameter (40–115 μm) of the laser or electric beam (Tables 2.2 and 2.3). Some of the applications of PBF in the industry and R&D are shown in Figure 2.3.

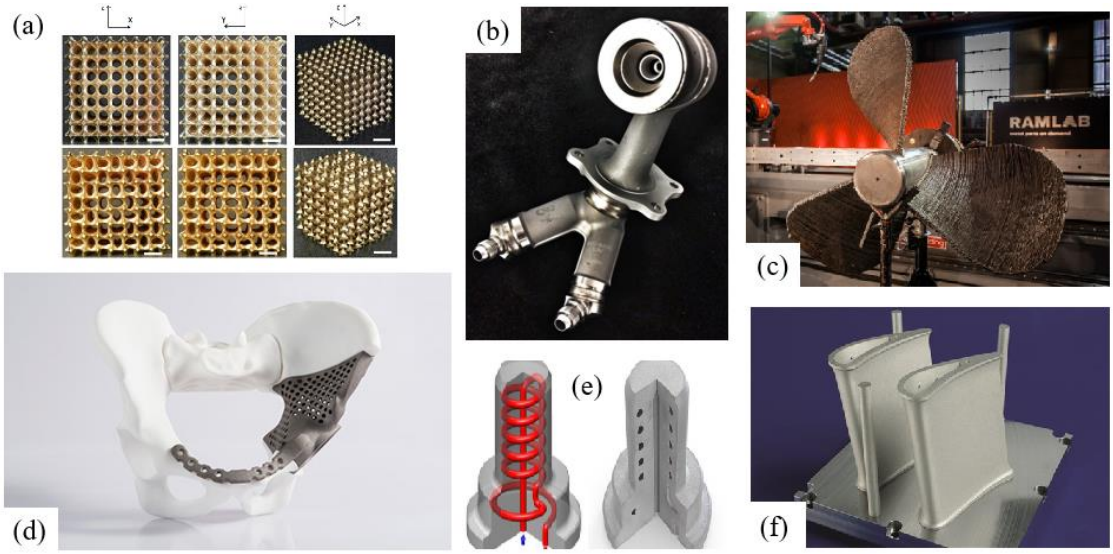

Figure 2.3. Applications of the powder bed fusion process. (a) Research using metal printed metamaterials. Reused with permission of IOP Publishing: *Society of Photo-optical Instrumentation Engineers* [14], Copyright © 2015; (b) GE fuel nozzle [15]; (c) RAMLAB ship propeller [16]; (d) EOS pelvis replacement [17]; (e) tool and die maker with conformal cooling [18]; (f) Siemens turbine blade [19].

With these various developments available in the manufacturing industry, it is now common to classify SLS, DMLS, SLM, and EBM as PBF processes, the reason being that they share certain features, such as the use of a powder bed with a roller and a high-power electron beam or laser as heat source [12].

2.2 Selective Laser Melting and Direct Metal Laser Sintering

This thesis focuses on two PBF processes, SLM and DMLS. Currently, this technology is commercially distributed by only a few manufacturers around the world, with a selection of alloys available [10], [20], [21]. The parameters used by SLM Solutions and EOS GmbH were chosen for this work. These two technologies have been improved drastically, allowing them to be implemented in high-end components for diverse engineering applications. Full-density parts can be built that offer similar or even slightly improved material properties over those of parts produced using conventional manufacturing processes [9]. Recent research shows that parts produced by SLM are stronger than the ones produced by casting; however, the SLM-produced parts tend to be less malleable owing to the rapid solidification that occurs during the process [9]. Table 2.1 shows some of the properties that can be found in SLM-produced parts.

Table 2.1. Tensile strength of selected metal alloys produced by SLM [9].

Material	UTS (MPa)	Yield strength (MPa)	Elongation (%)	Reference	Conventional material UTS (MPa)
Fe	411.50	305.30	—	[22]	225.00
Fe–Ni	600.00	—	—	[23]	—
Fe–Ni–Cr	1100.00	—	—	[23]	—
Fe–Ni–Cu–P	505.00	425.00	—	[24]	—
15-5 PH steel	1450.00	1297.00	12.53	[25]	1317.00
15-5 PH steel	1470.00	1100.00	15.00	[26]	1317.00
304 stainless steel	717.00	570.00	42.80	[27]	579.00
316L stainless steel	760.00	650.00	30.00	[28]	558.00
Maraging steel	1290.00	1214.00	13.30	[29]	1930.00

SLM equipment found on the market today offers different capabilities. Beam diameter is usually between 70 and 115 µm, laser thickness ranges from 20 to 75 µm, and maximum scanning speed is up to 10 m/s [10]. SLM Solutions offers three different machines: SLM 125, SLM 280

2.0, and SLM 500. The build rate and build envelope are the main differences among the machines, with SLM 280 2.0 and SLM 500 having the ability to use twin and quad lasers of 400, 700, or 1000 W depending on the optics configuration, as shown in Table 2.2. The same holds true for DMLS specifications (equipment manufactured by EOS GmbH), but with different ranges of parameters (Table 2.3).

Table 2.2. Configuration of three single laser melting machines (SLM Solutions) [10].

	SLM 125	**SLM 280 2.0**	**SLM 500**
Build envelope (length × width × height)	125 mm × 125 mm × 125 mm	280 mm × 280 mm × 365 mm	500 mm × 280 mm × 365 mm
3D optics configuration	Single (400 W)	Single (400 or 700 W); twin (400 or 700 W); dual (700 and 1000 W);	Twin (400 or 700 W); quad (400 or 700 W);
Laser and gas filling	IPG fiber laser with inert gas filling		
Build rate	Up to 25 cm^3/h	Up to 55 cm^3/h	Up to 105 cm^3/h
Layer thickness	20—75 µm		
Beam diameter	70—100 µm	80—115 µm	
Max. scan speed	10 m/s		

Table 2.3. Configuration of four direct metal laser sintering machines (EOS GmbH) [17].

	EOS M100	**EOSINT M280**	**EOS M290**	**EOS M400**
Build envelope (length × width × height)	Ø 100 mm × 95 mm	250 mm × 250 mm × 325 mm	250 mm × 250 mm × 325 mm	400 mm × 400 × 400 mm
3D optics configuration	Single (200 W)	Single (200 or 400 W)	Single (200 W)	Single (400 W) or quad (400 W)
Laser and gas filling	Yb fiber laser with inert gas filling (nitrogen)			
Build rate	Not provided			
Layer thickness	20–50 µm			
Beam diameter	40 µm	100–500 µm	100 µm	90 µm (single); 100 µm (quad)
Max. scan speed	Up to 7 m/s			

2.3 Limitations of and Technological Gaps in Powder Bed Fusion Processes

Process and environmental parameters are known to play an important role in determining the final mechanical properties of the parts produced by PBF, as several researchers have demonstrated [30]. Experimental studies consist of investigating mechanical properties, microstructures, the effect of varying the parameters (sensitivity), and several other aspects of the material. These studies have been performed since the commercialization of this technology first began, and many valuable research findings have helped to improve the process overall. However, experimental studies are incredibly costly, since numerous process parameters are involved in this technology. A relatively large investment was made by the vanguard in this sector to validate the commercialized alloys that they provided along with their machines. Although several investigators have uncovered excellent mechanical properties when using optimal process parameters with particular alloys, a variety of new alloys that could be used in this technology have not yet been validated.

The materials used thus far by SLM and DMLS are Ti6AL4V, SS-316L, AlSi10Mg, Hastelloy X, IN718, IN625, IN939, Invar36, CuSn10, 17-4PH, maraging steel, and some proprietary alloys such as GP1, MS1 by EOS GmbH, and Medi-Dent by SLM Solutions. These materials have their optimal parameters already defined by each of the manufacturers, and the manufacturer nearly always recommends the use of their metal powder only, making the process prohibitively expensive and inflexible in most situations. Manufacturers also prohibit new alloys from being used on this commercial equipment, and violations can void the equipment warranty in most cases.

Without the use of optimal parameters, a large number of issues can arise that affect the integrity of the built part. Residual stresses, layer delamination, cracking, warping, and undesired porosity are among the main problems when printing metal using PBF. These problems are mostly

due to the high temperature gradients induced by the laser. Figure 2.4a illustrates this problem, where a high heat flux from the laser to the powder bed is inputted in a short time frame. As a result, the powder (loose material) melts, causing the previous layers to lose strength owing to the high temperature of the top layer. At the same time, the expansion of the top layer is restricted by the deep layers, and elastic compressive strains are introduced. The top layer is finally plastically compressed at the yield strength of the material. When cooling (Figure 2.4b) the plastically compressed upper layers begin contracting and bending occurs. Figure 2.4c shows the delamination and cracking problem that results.

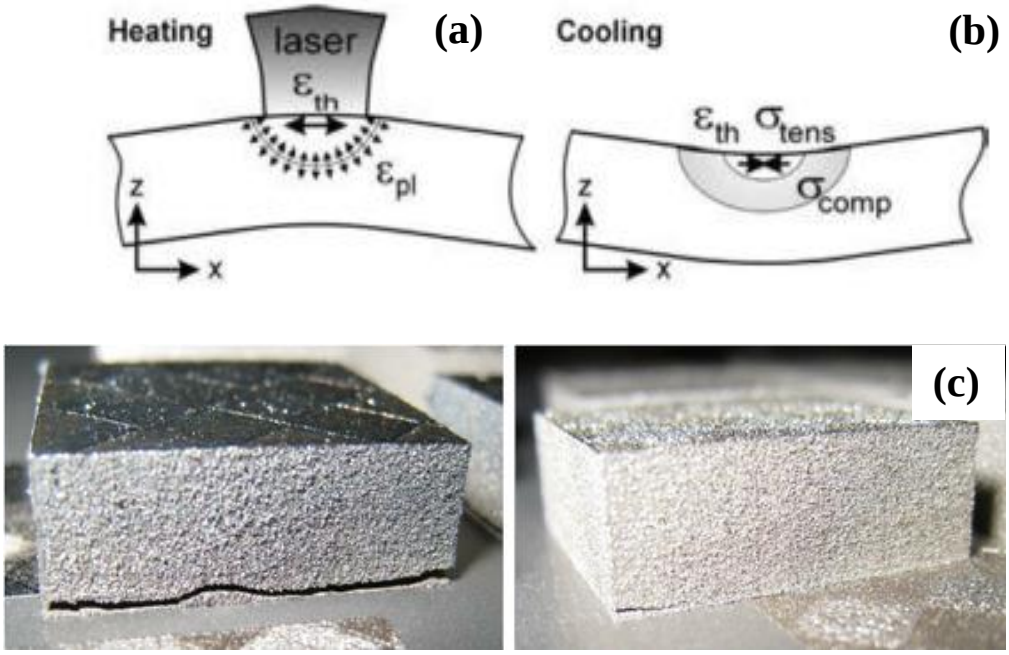

Figure 2.4. The laser heats the powder bed (a) and subsequent cooling occurs (b). Reused by permission from Emerald Publishing Limited: *Rapid Prototyping Journal* [31]. Copyright © 2006. Delamination and cracking observed on printed samples (c). Reused by permission from AIP Publishing: *Applied Physics Review* [9]. Copyright © 2015.

Another issue that arises when the correct parameters are not used during the printing of samples related to the porosity and poor mechanical properties of the final built part. Porosity and poor mechanical properties are associated with each other in general, since high porosity will reduce the yield strength of the material [32]. Porosity is mostly caused by low-level laser energy density; however, high-level laser energy density can bring some degree of porosity to the final part as well, mostly due to the presence of gas bubbles [33]. Laser energy density is a relationship between the main parameters of the process, such as power input, scanning speed, hatch distance, and layer thickness [34]. Equation 2.1 in the following section describes the laser energy density relationship.

2.4 The Finite Element Model of Powder Bed Fusion and Experimental Approaches

In the last 10 years, owing to advances in computational capability and the development of dedicated FEM software in the field, numerical analysis studies have become immensely popular [35]. There is considerable research involving multi-coupled aspects of the PBF process; yet, the majority of studies maintain single-mode analysis to reduce computational cost and model complexity. Multi-coupled models tend to show high nonlinearity and undesired deformation, leading to increased time to perform simulations and consequently high computational cost. The models used most often are thermal, kinetic, fluid dynamics (molten pool), and DEM, as well as the coupling of one or more types of analysis [36].

Recent progress has been achieved in the development of new alloys for PBF processes. Biomedical and aerospace applications are the most widely explored fields, as they demand parts with specific microstructural and material properties that match the requirements of their intended use [37], [38]. Most of this work is performed by studying the impacts of laser energy density on

the final material properties and analyzing the discontinuities, such as cracks, delamination, balling effect, heat-affected zone (HAZ), and residual stresses. The laser energy density E (J/mm^3) is defined as the relationship between the laser power input P (W), the scan speed v (mm/s), the layer thickness h (mm), and the hatch distance s (mm), as shown in eq. 2.1:

$$E_v = \frac{P}{v \cdot h \cdot s} \tag{2.1}$$

An experimental study using pure titanium has showed that applying a fixed laser energy density (120 J/mm^3) is enough to produce 99.5% of the relative density; however, the high density is greatly affected by laser power and hatching distance combinations [37]. In the same study, when comparing cast to SLM-built titanium alloys, the SLM-built sample displayed considerably better performance for wear resistance, yield strength, and Vickers micro-hardness. The porous titanium alloys produced by SLM have proved to be effective in biomedical applications, and their properties can be tailored to resemble human bones for better osseointegration [37]. EBM-built parts are also well explored in biomedical applications, especially those that produce lattice materials from topology optimization analysis. Different EBM-built samples with up to 70% porosity displayed acceptable mechanical properties for specific applications [38].

Microstructural studies have also been undertaken to correlate a material's mechanical properties with grain size and material phase. Liu et al. [39], [40] analyzed the microstructure and mechanical properties of β-type Ti–24Nb–4Zr–8Sn produced by EBM and SLM processes and the gradient in microstructure in AlSi10Mg samples produced by SLM. Titanium samples from SLM exhibited a single β-phase, while EBM-built samples consisted of α and β phases, meaning that faster cooling rates from the SLM process induced the formation of β dendrites and led to a low Young's modulus when compared with the properties of EBM-built parts. Another notable result

was how the HAZ was influenced by the laser and electron beam spot, with EBM displaying a high HAZ (~200 μm) owing to the larger electron beam spot (~40 μm with SLM) [39]. AlSi10Mg samples produced by SLM using 30 μm layer thickness and 1500 mm/s scanning speed experienced cooling rates of 1.44×10^6 K/s on the top of the powder bed and around 1×10^3 K/s on the bottom [40]. The high cooling rates present in the melt pool were responsible for the gradient microstructure in the sample, meaning that the grains in the surface of the sample are finer than those in the core, resulting in greater wear resistance and hardness [40].

The numerical simulation of PBF processes has improved our understanding of the effects of parameters in several ways. Denlinger et al. [41] conducted a thermal modeling experiment of Inconel 718 with an in situ temperature setup to acquire temperature distributions. The model predicted the temperature distribution with an error of 11% during the acquisition period and showed that conductivity in powdered media should be accounted for in PBF analyses. Huang et al. [42] also performed a similar study using TiAl6V4, with their results indicating that laser power plays a more fundamental role in the powder bed thermal behavior compared with other parameters such as scan speed and hatch distance. However, shorter hatch distances and tracks can decrease the temperature gradient while at the same time increasing the maximum temperature achieved. Shaw and Dai [43] developed coupled thermomechanical models for multi-material behavior and analyzed residual stresses. Cheng et al. [44] investigated residual stresses and the deformation of a multi-layer model using different scanning strategies. And finally, Vastola et al. [45] conducted a parameter analysis on the final residual stresses when performing a single laser track using TiAl6V4.

Liu et al. [46] conducted a study of SLM-built lattice materials under compressive testing and cyclic loading–unloading conditions with different strains. An FEM built in Comsol was then employed to visualize the local stress concentration for each lattice configuration. Results obtained in this study showed that the energy absorption for all cases can be directly attributed to the difference between stress distributions and local stress concentrations [46]. Loh et al. [47] conducted a parametric study, building an FEM able to predict melt-pool geometry of an SLM process using aluminum 6061. Among the findings, they found that high laser power and low scanning speed were responsible for increased melt penetration and width; similarly, when using low laser power and high scanning speed, the same phenomena were observed, although the latter process was more energy efficient [47].

Residual stress analysis has also been well explored experimentally using two different approaches: the crack compliance method and the X-ray diffraction method [31]. The crack compliance method is the simplest in that it uses strain gauges positioned around a predetermined surface. This surface is later wire cut in small steps using electric discharge machining, and the strain values are measured for each position. Later, a fitting curve profile based on either a Legendre or Fourier series is used to account for the strain measurements, and the subsequent residual stress profile is obtained. The X-ray diffraction method is most often used in research on AM processes, as it can measure surface residual stresses, in contrast to the crack compliance method, which is only able to measure residual stresses through the thickness of the material.

X-ray diffraction is responsible for identifying the material phase in the samples produced and for describing the diffracted angle (2θ) that characterizes the measured lattice plane ($hk\ell$). The lattice deformation from the samples is obtained using a radiation source and compared with the

unstressed lattice measured from the same material. This method has the advantage of obtaining stresses in two axes through the surface (plane). Mostafa et al. [48] have performed several measurements in a large group of 3D-printed airfoils to account for residual stresses. They concluded that thermal stresses and phase transformation were the main causes of the residual stresses and were mostly in the compressive state, be it in the scanning or the build direction. These residual stresses are justifiable, since the material is cooling very fast and shrinkage is expected to occur. Mercelis and Kruth [31] performed a theorical and experimental study using both the X-ray diffraction and crack compliance methods. Their work yielded very similar findings to those of Mostafa et al.; however, the authors observed a different residual stress state in the parts before and after removal of the printed parts with a low aspect ratio. This means that when the part is built, the bottom of the part is fused to the substrate and generates additional residual stress. When the part is finally removed from the substrate, the residual stresses are relieved to some extent, which can induce part deformation [31].

3 POWDER THERMAL PROPERTIES

This chapter was partially adopted from the journal publication of "de Moraes, D.A., Czekanski, A. Parametric thermal FE analysis on the laser power input and powder effective thermal conductivity during selective laser melting of SS304L. *J. Manuf. Mater. Process*. 2018, 2, 47". According to the copyright agreement, "The authors retain all copyrights and will not be forced to sign any copyright transfer agreements."

3.1 Powder Packing Density

The contact between powder particles is an important factor when analyzing the effective thermal conductivity of the powder bed [49]. The size of the powder particles, their distribution, and their shape affect the contact area between the particles, which influences effective thermal conductivity [50]. Kovalev and Gusarov [50], [51] studied the effects of monodispersed and polydispersed powder beds and different packing densities on the thermal conductivity of particles using FEM packed spheres (DEM modeling). They obtained satisfactory results when comparing their DEM model findings with the analytical solution based on Hertz contact theory [52].

The packing density (relative density) of the powder bed directly affects powder porosity, one of the main parameters influencing effective thermal conductivity. The following are important prior observations about powder that form the general principal assumptions considered in this study:

- The relative density was calculated assuming a perfect monodispersed spherical powder;
- The powder bed was modeled as a whole, meaning that our model represents the total volume occupied by the powder bed, not the individual powder particles;

- Contact between particles was considered to be in the elastic zone, with no plastic deformation; and
- External loads were neglected, and only gravitational forces were accounted for.

3.1.1 Packing structures

Three different packing structures were analyzed. The simple cubic (SC), generally known as a cubic structure, is a packing structure with a relative density of 0.523 and represents the least dense packing structure in this study. The body-centered cubic (BCC) packing structure has an intermediate relative density of 0.68. The face-centered cubic (FCC) packing structure, generally referred to as a close-packed structure, has a relative density of 0.74.

Although there are several other packing structures described in the literature, such as diamond-like (relative density of 0.34) and hexagonal close-packed (relative density of 0.74048), it was not the objective of this study to include those structures, since the results of the included packing structures can be extrapolated. In this case, relative density is described by the atomic packing factor (AFP), which is calculated using the following equation:

$$\mathrm{AFP} = \frac{n_{\mathrm{particle}} \cdot V_{\mathrm{particle}}}{V_{\mathrm{unit\ cell}}} \tag{3.1}$$

where n_{particle} is the number of particles per unit cell (cube in this case), V_{particle} is the volume of each corresponding particle, and $V_{\mathrm{unit\ cell}}$ is the volume of the unit cell. For instance, the SC structure in Figure 3.1a has eight 1/8 of a particle at each corner, giving a total of one particle per unit cell. Each particle, assumed to be a sphere, has a volume of $4\pi r^3/3$, and the volume of the unit cell (cube) is represented by $(2r)^3$. These parameters yield the following relative density:

$$\mathrm{AFP} = \frac{(1)\frac{4}{3}\pi r^3}{(2r)^3} \approx 0.523 \tag{3.2}$$

Figure 3.1 shows the packing structures of SC, BCC, and FCC, respectively.

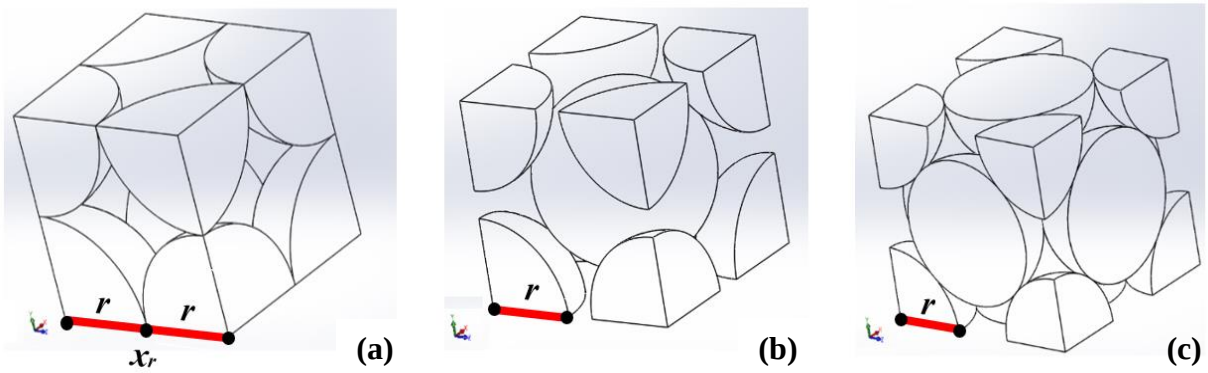

Figure 3.1. Simple cube (SC) packing structure (a), body-centered cubic (BCC) packing structure (b), and face-centered cubic (FCC) packing structure (c).

3.2 Contact Area and Porosity of the Powder Bed

The contact of two adjacent spherical particles is essential when calculating thermal conductivity, since heat exchange occurs primarily through conduction [53]. The respective radius of contact is based in the Hertz theory to contact interaction of solid bodies [52]. This contact area is very small (Figure 3.2), especially in the present study, since plasticity is not considered and gravity is the only force acting among particles. The main influence of the contact radius is associated with the thermal conductivity due contact between particles, where majority of the heat losses occur during the process. In the following section 3.5 the contact thermal conductivity is addressed.

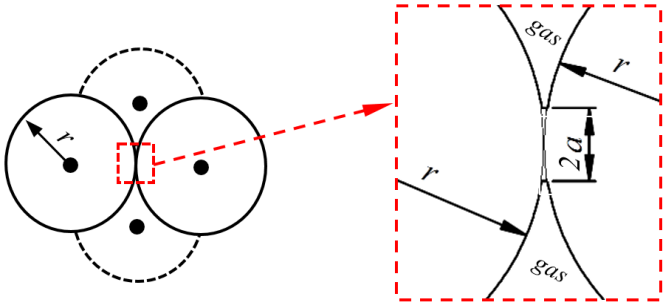

Figure 3.2. Particles in the contact region (left) and in the contact radius in detail (right).

An equation derived from Dul'nev and Zarichnyak's model is applied to define porosity, as Abyzov et al., Kovalev, and Gusarov later successfully applied this equation in their models to calculate effective thermal conductivity [50], [52], [54], [55]. Porosity, φ, is expressed as a function of the coordination number, N, as follows:

$$\varphi = \frac{3N - 4}{N(N-1)} \tag{3.1}$$

$$N = \frac{1}{M}\sum_{j=1}^{M} k_j \tag{3.2}$$

where the mean coordination number of a given particle, N, is defined as the number of its neighbor's particles that have their respective centres at a distance that corresponds exactly to the diameter of the original particle when studying monodispersed spheres. The correlation in eq. 3.4 is the mathematical representation of N, while M is the total number of particles in the domain and k_j is the number of contacts of a given particle j. The mean coordination numbers for FCC, BCC, and SC packing structures are 12, 8, and 6, respectively, resulting in porosities of 0.2424, 0.3571, and 0.467, respectively. In previous work, the effects of powder packing in the bed were not analyzed, and thus a general porosity value of 0.400 was adopted [36]. The equation for loading applied by a roller or scraper (F_N) and the material properties constant (E^*) is defined by Hertz elastic contact theory [52]:

$$F_N = \frac{1}{3}\frac{a^3 E^*}{x_r} \tag{3.3}$$

$$E^* = \frac{E}{(1-\nu^2)} \tag{3.4}$$

where a is the contact radius, E is Young's modulus, and ν is Poisson's ratio. Combining load eq. 3.5 with eq. 3.6 and isolating for contact radius, we obtain the following:

$$a = \sqrt[3]{\frac{3}{4}\frac{x_r F_N (1-\nu^2)}{E}} \tag{3.5}$$

In this study, besides the three packing densities, three different powder diameters were analyzed: 20, 60, and 100 μm. The normal contact load between the particles in the SLM process is difficult to account for analytically, and a proper model for compaction by roller or scraper should be implemented. It was not the objective of this work to develop such a formulation, and hence only gravitational loads were the forces considered to be acting in the powder bed [50].

The roller or scraper, when distributing a new layer of powder, can increase the load between the particles in the powder bed. However, no specific data or studies were found that associated the effect of the roller or scraper with packing structure or contact loading. We assumed that as soon as the roller or scraper finished distributing a new layer, the additional load due to powder compaction ceased to exist. For this reason, in this study we assumed that the roller or scraper impact on the powder is related only to the particle packing structure, not to the actual compaction of powder through the powder bed.

3.3 Material Properties

The material used to develop the model was SS-304L. This alloy is considerably less expensive and yet is still not available for commercial use. The alloy's temperature-dependent

properties were derived from a report by Kim [56] and are shown in Figure 3.3, including specific heat, density, and thermal conductivity, all of which are essential parameters to know when simulating a high-temperature change in thermal distribution over small increments of time. To accommodate phase transformation, we also included latent heat, as it modifies heat capacity during the melting of the powder [36].

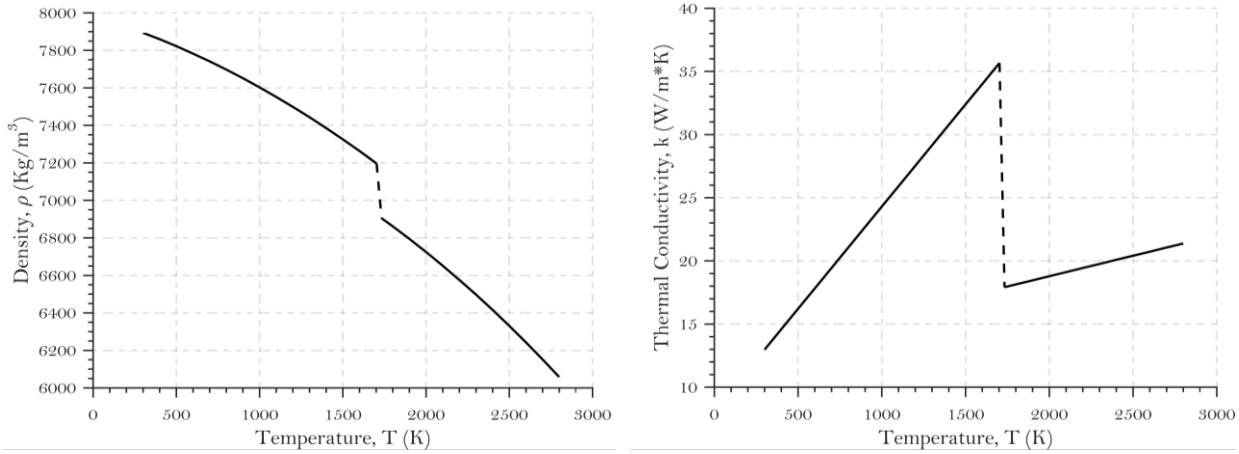

(a)

(b)

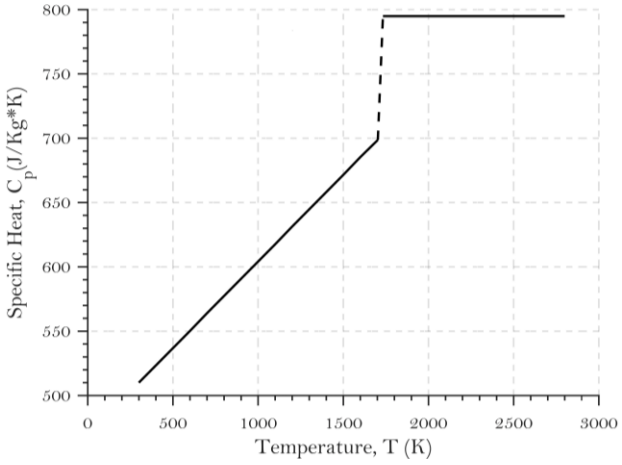

(c)

Figure 3.3. Temperature-dependent density (a), thermal conductivity (b), and specific heat (c) of stainless steel 304L.

3.4 Powder Emissivity

Powder emissivity was included as a model parameter, as it affects overall radiation thermal losses and the thermal conductivity of the powder bed. Since we have three different packing-density scenarios — SC, BCC, and FCC — along with their respective powder bed porosity values, there are three different emissivity values to determine. The following formulations were used to achieve the final value of emissivity, where ε_{p} is defined as effective powder emissivity, ε_{s} is solid emissivity of the material, ε_H is gap emissivity, A_{H} is area fraction of the powder surface, and φ is powder porosity [53]:

$$\varepsilon_{\mathrm{H}} = \frac{\varepsilon_{\mathrm{s}}\left[2 + 3.082\left(\frac{1-\varphi}{\varphi}\right)^2\right]}{\varepsilon_{\mathrm{s}}\left[1 + 3.082\left(\frac{1-\varphi}{\varphi}\right)^2\right] + 1} \tag{3.6}$$

$$A_{\mathrm{H}} = \frac{0.908\varphi^2}{1.908\varphi^2 - 2\varphi + 1} \tag{3.7}$$

$$\varepsilon_{\mathrm{p}} = A_{\mathrm{H}}\varepsilon_{\mathrm{H}} + (1 - A_{\mathrm{H}})\varepsilon_{\mathrm{s}} \tag{3.8}$$

In Figure 3.4, the emissivity values calculated for the three different packing densities considered in this work are plotted along the curve representing all possible emissivity values. A 0% porosity is interpreted as being representative of a full-density material, which is considered to have an emissivity of 0.44 for SS-304L [53], [57].

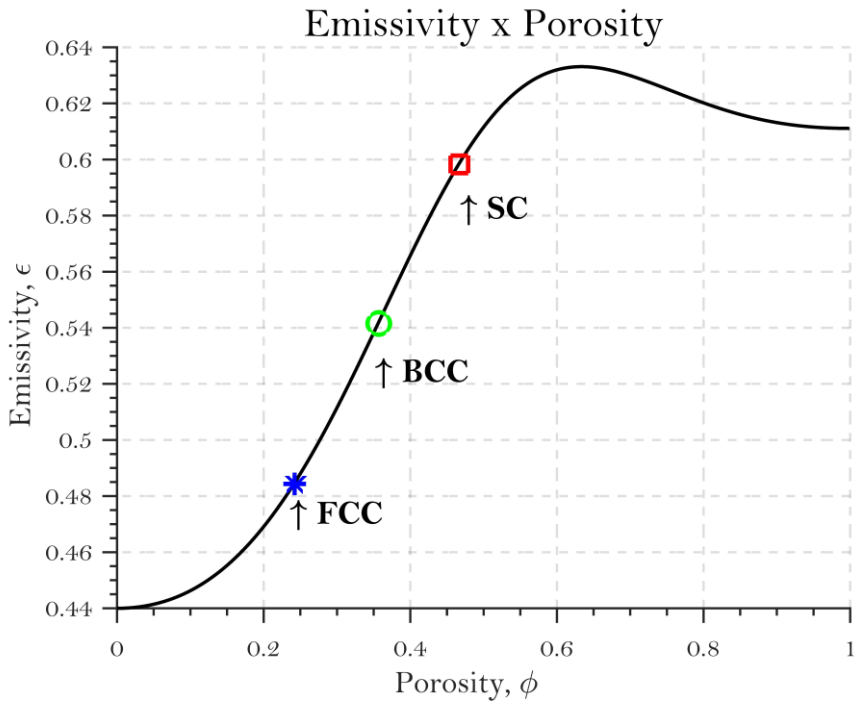

Figure 3.4. Porosity-dependent emissivity of simple cubic (SC) packing structure, body-centered cubic (BCC) packing structure, and face-centered cubic (FCC) packing structure.

3.5 Effective Thermal Conductivity of Powders

The definition of effective thermal conductivity (k_{eff}) of powders addresses four of the main thermal transport phenomena that occur in the powder bed: contact thermal conductivity between particles, $k_{contact}$; thermal conductivity due to radiation, k_R; gas thermal conductivity, k_g; and solid thermal conductivity of SS-304L, k_s [53], [58]. Wakao and Kagei [58] developed this definition for powder-packed beds. It was applied in several studies, including the work of Sih and Barlow [53], as previously mentioned. Below is the full equation, with all four main terms already expanded, followed by Figure 3.5 showing the compiled results for SS-304L at temperatures of 300 K to $T_{Solidus}$.

$$k_{\text{eff}} = k_{\text{g}} \left\{ (1-\sqrt{1-\varphi}) \left(1+\frac{\varphi k_{\text{R}}}{k_{\text{g}}} \right) + \sqrt{1-\varphi} \left[(1-\Lambda). \left(\frac{2}{\left(1-\frac{Bk_{\text{g}}}{k_{\text{s}}} \right)} \cdot \left(\frac{B}{\left(1-\frac{Bk_{\text{g}}}{k_{\text{s}}} \right)^2} \cdot \right. \right. \right. \right.$$

$$\left. \left. \left. \left. \cdot \left(1-\frac{k_{\text{g}}}{k_{\text{s}}} \right) \ln \left(\frac{k_{\text{s}}}{Bk_{\text{g}}} \right) - \frac{B+1}{2} - \frac{B-1}{\left(1-\frac{Bk_{\text{g}}}{k_{\text{s}}} \right)} \right) + \frac{k_{\text{R}}}{k_{\text{g}}} \right) + \Lambda \frac{k_{\text{contact}}}{k_{\text{g}}} \right] \right\} \tag{3.9}$$

$$B \cong 1.25 \left(\frac{1-\varphi}{\varphi} \right)^{\frac{10}{9}} \tag{3.10}$$

$$k_{\text{R}} = \frac{4\varepsilon_{\text{p}} \sigma T^3 x_{\text{R}}}{1-0.132\varepsilon_{\text{p}}} \tag{3.11}$$

$$k_{\text{contact}} = \begin{cases} 18\Lambda k_{\text{s}}, & \Lambda < 3\times10^{-4} \\ k_{\text{s}}, & \Lambda > 1\times10^{-2} \end{cases} \tag{3.12}$$

$$\Lambda = \frac{A_{\text{contact}}}{A_{\text{cross-section}}} \tag{3.13}$$

The thermal radiation term is highly influenced by powder diameter, temperature, and emissivity of the powder bed. Thermal conductivity, owing to the contact between particles, will vary according to the contact ratio and the initial solid thermal conductivity, since the value of the fractional contact area, Λ, is less than 3×10^{-4}. The term B is a deformation parameter that varies according to porosity. Note that the compilation of the effective thermal conductivity of the powder will generate nine different curves. We have three packing densities (SC, BCC and FCC) that affect, respectively, porosity and emissivity, yielding three k_{eff} curves. There are also three

different powder diameters (20, 60 and 100 μm) that affect the fractional contact area, yielding three curves per packing density scenario.

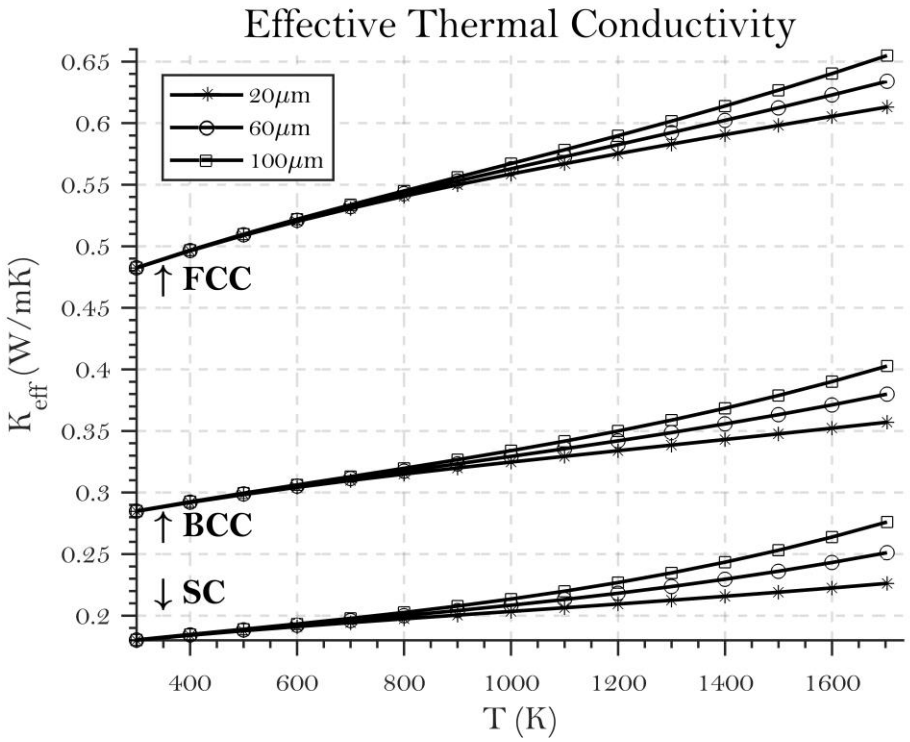

Figure 3.5. Effective thermal conductivity of powder in simple cubic (SC) packing structure, body-centered cubic (BCC) packing structure, and face-centered cubic (FCC) packing structure, with powder particles of 20, 60, and 100 μm diameter.

It is evident from Figure 3.5 that powder diameter does not significantly affect the value of k_{eff} for temperatures between 300 and 800 K. However, for higher temperatures, owing to the radiation term, there is a perceptible difference. For example, for FCC there is ~7% k_{eff} increase when using a powder with a diameter of 100 μm instead of 20 μm. The margin increases to 22% when doing the same comparison with SC, owing to the higher emissivity of SC compared with that of FCC. When comparing the different packing densities, the increase in k_{eff} is even greater, more than 2.5 times that between SC and FCC for instance.

3.6 Verification and Conclusions

The results compiled in the last section for effective thermal conductivity of a powder were not verified experimentally owing to the considerations already mentioned. These include the geometric shape of the particles (spherical) and because attempting to represent the packing structures with a commercially available powder is impractical. The reason is that the powder particles have a size distribution that ranges from a minimum value to a maximum value and generally follows a Gaussian profile. In addition, the powder particles are not all necessarily spherical; they can take any geometric configuration possible (oblong, oval, etc.) [59].

Nevertheless, recent studies in the field, both numerical and experimental, are in good accordance with the results presented here, although some use different materials and methodologies [50], [60]. Kovalev and Gusarov [50] modeled a DEM powder bed with several powder packing densities and conditions. The steel used for the model was not specified, but the authors used the following properties: E = 210 GPa, ρ = 6900 kg/m³, C_p = 477 J/kg·K, ν = 0.28, and k_s = 30.5 W/mK. Also worth noting, the authors did not consider temperature-dependent properties, while these properties are considered in the model described in this thesis.

Alkahari et al. [60] performed an experiment whereby they measured the effective thermal conductivity of SS-316L. A point source of heat was applied to the powder receptacle, to which thermocouples were attached, to measure the moment in time when maximum voltage is reached [60]. The setup was executed only at ambient temperature (300 K) for four different powder diameters and bulk densities. Table 3.1 compares the thermal conductivity determined in the literature cited above with the value determined in the current work.

Table 3.1. Comparison of effective thermal conductivity from Kovalev and Gusarov [50], Alkahari et al. [60], and the current work.

Packing structure	**DEM model from Kovalev and Gusarov:** T **= 300 K,** x_r **= 62.5 µm, unspecified steel**	**Experimental data from Alkahari et al.:** T **= 300 K,** x_r **= 50 µm, SS-316L**	**Analytical model in current work:** T **= 300 K,** x_r **= 60 µm, SS-304L**
Cubic	0.014 W/mK	0.206 W/mK	0.180 W/mK
Body-centered cubic	0.026 W/mK	—	0.285 W/mK
Face-centered cubic	0.039 W/mK	—	0.482 W/mK
Random	0.015 W/mK	—	—
Polydispersed	0.009 W/mK	—	—

Note: Where no data are provided (—), that type of powder was not included in the study.

Comparing the effective thermal conductivity between the work of Gusarov–Kovalev and that of the current model shows that they do not match, with the latter being around 10 times larger. Since the materials employed are different, we cannot draw a definitive conclusion about the exact values, but there is a tendency observed in both data sets: the higher the packing density, from SC to FCC, the higher k_{eff}. The increased percentage is similar as well, with 54% from SC to BCC and 67% from BCC to FCC for the Gusarov–Kovalev data, and 63% from SC to BCC and 59% from BCC to FCC for the current data. This confirms that packing density influences thermal conductivity, with the lower packing density having the lower k_{eff}.

When comparing the findings of Alkahari et al. with those of the current model, there is very close agreement between the k_{eff}, with a difference of only 13%, as shown in Table 3.1. Alkahari et al. conducted a study using different bulk densities, which is in fact a packing density analysis; however, we cannot infer which value of bulk density corresponds to the packing structure in the current model. From the results, the authors found that increased bulk density and powder diameter raise the k_{eff} as well, an observation similar to that for the current model.

4 FINITE ELEMENT THERMAL MODELING OF SELECTIVE LASER MELTING

This chapter was partially adopted from the journal publication of "de Moraes, D.A., Czekanski, A. Parametric thermal FE analysis on the laser power input and powder effective thermal conductivity during selective laser melting of SS304L. *J. Manuf. Mater. Process.* 2018, 2, 47". According to the copyright agreement, "The authors retain all copyrights and will not be forced to sign any copyright transfer agreements."

4.1 Governing Equations

The temperature distribution of the PBF process, described as $T(x,y,z,t)$, is found by solving the three-dimensional heat conduction equation (eq. 3.1) with suitable boundary conditions as follows:

$$\rho(T)C_{\mathrm{p}}(T)\frac{dT}{dt} = -\nabla \cdot \bar{q}(\bar{r},t) + Q(\bar{r},t) \tag{4.1}$$

$$\bar{q}(\bar{r},t) = -k\nabla T \tag{4.2}$$

$$\bar{r} = x, y, z \tag{4.3}$$

where the $\rho(T)$ and $C_{\mathrm{p}}(T)$ are the density and specific heat with temperature T dependent values, respectively; $q(r,t)$ is the rate of flow of heat energy per unit area; $Q(r,t)$ is the volumetric heat flux; and r represents the three-dimensional Cartesian coordinates in this study [61]. By substituting eq. 3.2 into eq. 3.1 and decomposing the Laplace operator, we arrive at:

$$\rho C_{\mathrm{p}}\frac{\partial T}{\partial t} = \frac{\partial}{\partial x}\left(k\frac{\partial T}{\partial x}\right) + \frac{\partial}{\partial y}\left(k\frac{\partial T}{\partial y}\right) + \frac{\partial}{\partial z}\left(k\frac{\partial T}{\partial z}\right) + Q \tag{4.4}$$

The boundary conditions for the thermal analysis depend on the environment inside the chamber. In this case, besides the conduction that is happening in the powder bed, thermal conduction and radiation are accounted for by considering the powder emissivity, the type of inert gas, and the initial temperature inside the chamber [41], [49]. The following equations are described in the literature for convection and radiation:

$$q_{\text{conv}} = h_{\text{c}}(T - T_0) \tag{4.5}$$

$$q_{\text{rad}} = \varepsilon_{\text{p}}\sigma(T^4 - T_0^{\,4}) \tag{4.6}$$

where h_{c} is the convective heat transfer coefficient, ε_{p} is the emissivity of the powder surface, σ is the Stefan–Boltzmann constant, and T and T_0 are the surface and ambient temperatures, respectively [41]. To reduce computational cost, the convective and radiant heat transfers were modeled as a combined boundary condition. The main reason for doing so is that radiation is a highly nonlinear heat-transfer condition, a property that increases computational costs and time [62]. In an experimental study by Vinokurov, the following equation combining radiation and convection was demonstrated to have less than a 5% loss in accuracy [63]:

$$h = h_{\text{c}} + \varepsilon\sigma(T^2 + T_0^2)(T + T_0) \cong 2.41\times10^{-3}\varepsilon_{\text{p}}T^{1.61} \tag{4.7}$$

The appropriate value of powder emissivity, ε_{p}, was determined in chapter 3. A user-defined subroutine, FILM, was used to combine the coefficients of radiation and convection.

4.2 Thermal Model Domain and Finite Element Model

The thermal model was defined to handle materials in different phases (liquid, solid, and powder states) as well as to account for their variation at different temperatures. A three-dimensional model was established using a 25 μm DC3D8 hexahedron element with a total domain

of 1500 μm × 1500 μm × 75 μm (1.5 mm × 1.5 mm × 0.075 mm), as shown in Figure 4.1. A small domain was justifiable given the small laser spot diameter of 50 μm used in the model and the very low thermal conductivity present on the bed.

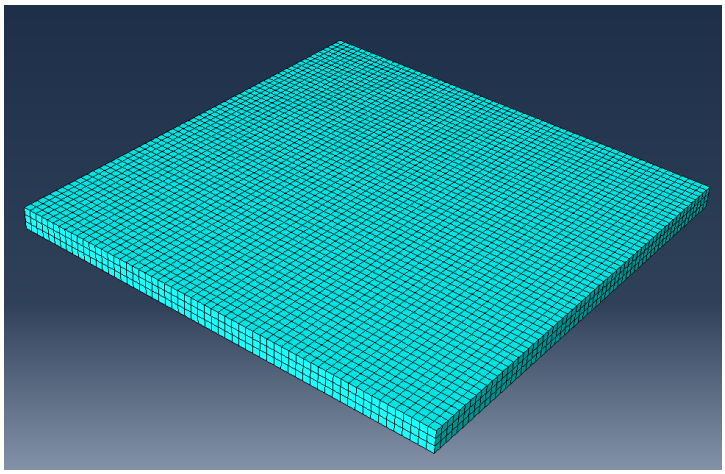

Figure 4.1. Three-dimensional domain of the model.

The software used for this work was Abaqus. The choice was made considering the volume and quality of previous available findings in which Abaqus was the most frequently used option [45], [64]–[67]. The software is also flexible enough to permit user-defined subroutines, allowing proper implementation of the moving heat source and boundary conditions [68]. The material was modeled as temperature and state dependent, as defined in chapter 3, ensuring more accurate representation of temperature distributions. Some additional considerations that maintained low computational time and cost inferred the following principal assumptions of the FEM model:

- Thermo-fluid effects were not considered, so the Marangoni effect and fluid flow in the melt pool were not accounted for;

- Material vaporization is not accounted for, although the phenomenon can occur at high temperatures. The impact of vaporization, however, would not affect the temperature distributions in this study [69];
- A single track of the laser was observed and the influence of the hatch distance was neglected to focus on the effect of packing structure and particle diameter on the temperature distributions; and
- Only mean powder (particle) diameter was considered when calculating the effective thermal conductivity of the powdered state.

Abaqus, as already mentioned, allows the user to write subroutines. For this model, the DFLUX and FILM subroutines were implemented to account for Gaussian heat flux and convection–radiation, respectively. The solution given is the temperature distribution of the process, described as $T(x,y,z,t)$, obtained from each selected node associated with the cross-section being analyzed.

4.3 Modeling of Selective Laser Melting Heat Source

The laser used in the SLM process follows a Gaussian heat flux profile. The laser used in this study was an ytterbium fiber laser with a TEM_{00} profile. TEM, or transverse electromagnetic mode, refers to the classification used for laser beams that follow a Gaussian profile. Figure 4.2 shows these different TEM profiles for several lasers [70], [71]. Although the laser profile is described as Gaussian, the process is not stationary, meaning that the laser is not heating only one specific point at a time. The movement of the heat source through the powder bed is no longer described as a purely Gaussian profile, but a combination of the three different profiles within the three-

dimensional space, resulting in a double ellipsoid shape that is usually called a “comet tail” shape [66].

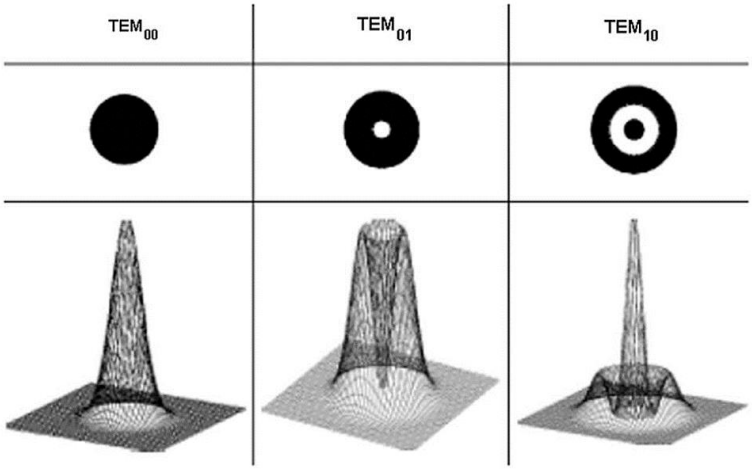

Figure 4.2. Different transverse electromagnetic modes for lasers. Reused by permission from Elsevier: *International Journal of Machine Tools and Manufacturing* [71], Copyright © 2009.

$$\dot{Q}_{f(x,y,z)} = \frac{6\sqrt{3} f_f \eta_{abs} P}{a_f bc\pi\sqrt{\pi}} e^{-\left(\frac{3x^2}{a_f{}^2} + \frac{3y^2}{b^2} + \frac{3z^2}{c^2}\right)} \tag{4.8}$$

$$\dot{Q}_{r(x,y,z)} = \frac{6\sqrt{3} f_r \eta_{abs} P}{a_r bc\pi\sqrt{\pi}} e^{-\left(\frac{3x^2}{a_r{}^2} + \frac{3y^2}{b^2} + \frac{3z^2}{c^2}\right)} \tag{4.9}$$

The “comet tail” shape (Figure 4.3) is the result of a high-power laser, usually a fiber laser of 100 to 1000 W, that consolidates the powder in SLM systems, as shown in Table 2.2 [10]. There are several formulations in the literature for the moving heat source [44], [45], [62], [64], [65]. The first developments in numerical simulation to account for the phenomena came from Goldak et al. [72] in 1984. His model for welding processes has been widely used since then, with some

modifications depending on the process being studied. Recently, several authors have been applying the formulation in the PBF numerical simulation, with good results being obtained, in accordance with the melt pool profile induced in the powder bed [73], [74] [41], [67]. For this reason, the Goldak implementation was used in this thesis, as described in eqs. 4.8 and 4.9, and modeled into the DFLUX subroutine using Fortran language [72].

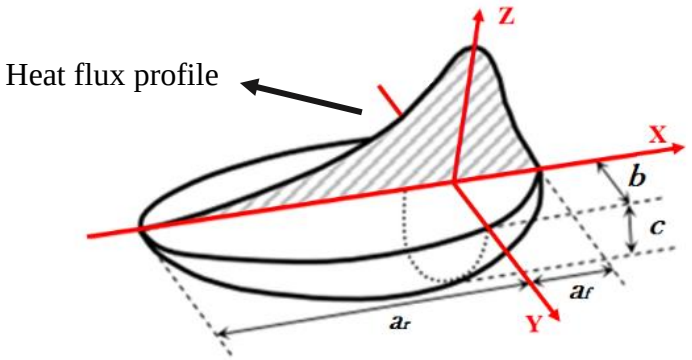

Figure 4.3. Double-ellipsoidal heat source model. Adapted by permission from Springer Nature: *Metallurgical and Materials Transactions* B [72], Copyright © 1984.

The heat flux, $\dot{Q}_{(x,y,z)}$, is represented as two functions, one for the front part of the flux and another for the rear part. These terms yield the correct representation of the comet shape formed by the laser moving through the powder bed. In Figure 4.3, the heat source moves in the *X*-axis, scanning the bed with steady speed. The longitudinal ellipsoid has two coefficients, a_{f} (front) and a_{r} (rear); the cross-section is determined by *b* and the depth by *c*. The parameter f_f corresponds to the front heat fraction (0.6), and the rear heat fraction is represented by f_r (1.4) [72]. η_{abs} is the powder absorption coefficient. Finally, *x*, *y*, and *z* are the coordinates of the model. Figure 4.4 below shows the heat flux distribution at a stationary point.

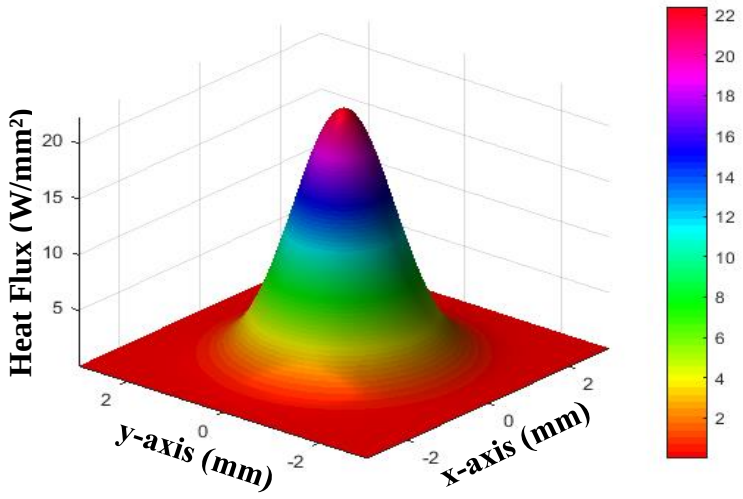

Figure 4.4. Static heat flux distribution modeled as a Gaussian profile using the Goldak formulation.

4.4 Phase Transformation

Phase transformation must be considered to analyze the proper temperature profile induced by the phase change in the powder bed. The formulation that investigators have used extensively is based on the modification of specific heat according to the latent heat and the solidus and liquidus temperatures:

$$C_{\mathrm{eq}}(T)=\begin{cases} C_{\mathrm{p}}(T), & T \le T_{\mathrm{S}} \\ C_{\mathrm{p}}(T)+\dfrac{L_{\mathrm{f}}}{T_{\mathrm{L}}-T_{\mathrm{S}}}, & T_S < T < T_{\mathrm{L}} \\ C_{\mathrm{L}}, & T \ge T_{\mathrm{L}} \end{cases} \tag{4.10}$$

where C_{p} is the specific heat, L_{f} is the latent heat of fusion, C_{L} is the specific heat of the liquid, and T_{L} and T_{S} are the liquidus and solidus temperatures, respectively.

4.5 Parameters of the Simulation

For the three-dimensional model using transient thermal analysis, the distributor of Abaqus recommends that the following equation be used to determine the minimum time increments required:

$$\Delta t > \frac{\rho C_p}{6k} \Delta l^2 \tag{4.11}$$

where $C_p, \rho, k,$ and Δl are, respectively, the specific heat, density, thermal conductivity, and element size of the meshing. This calculation prevents false oscillations that may appear in the boundary vicinities as well inaccurate solutions for very small time increments [68]. To execute and debug subroutines that are written in Fortran, the software is linked with Intel Parallel Compiler 17.0 and Visual Studio 2012 [75].

Following this recommendation and for convenience, a time increment of 1.5×10^{-6} s was used with 1000 increments, yielding a total time of 1.5 ms. The total time was calculated based on the speed of the laser, which was defined as 1 m/s. The other model parameters are listed in Table 4.1.

Table 4.1. Parameters of the selective laser melting simulation.

Parameters	**Values**	**Reference(s)**
Latent heat of fusion, $\boldsymbol{L_f}$ (J/kg)	273790	[62]
Solidus temperature, $\boldsymbol{T_S}$ (K)	1703	[56]
Liquidus temperature, $\boldsymbol{T_L}$ (K)	1733	[56]
Solid emissivity, $\boldsymbol{\varepsilon_s}$	0.44	[57]
Preheat temperature, $\boldsymbol{T_0}$ (K)	298, 373, 643	[10], [20], [21]
Absorption coefficient, $\boldsymbol{\eta_{abs}}$ (W)	0.40	[76]
Laser spot diameter $\boldsymbol{d_0}$ (μm)	50	[10], [20], [21]
Layer thickness, $\boldsymbol{h}$ (μm)	75	[10], [20], [21]
Laser power input, $\boldsymbol{P}$ (W)	100, 200, 400	[10], [20], [21]
Scanning speed, $\boldsymbol{v}$ (m/s)	1.0	[10], [20], [21]
Average powder diameter, $\boldsymbol{x_R}$ (μm)	20, 60, 100	[77]

Gas thermal conductivity, k_g (W/m·K)	0.016	[41]
Coefficient a_r (μm)	220	[72]
Coefficient a_f (μm)	60	[72]
Coefficient b (μm)	120	[72]
Coefficient c (μm)	150	[72]
Time step, t (ms)	1.5	-

4.6 Results

4.6.1 Longitudinal and cross-sectional temperature distributions

The numerical analysis was conducted for three laser inputs combined with three packing densities and three different powder diameters, resulting in 27 compiled models. A single processor was used for each simulation and two tokens were available for Abaqus, allowing two parallel simulations to be run at the same time. We used an Intel Core i7-6700 3.4GHz processor that was able to run all the compilations for one substrate temperature in 14 h (42 h total), averaging ~30 min for each simulation.

The temperature was measured at nodal points from the mesh, with acquisition points for the time-dependent temperature measurements (total time = 1.5 ms), shown in yellow, taken through the thickness of the layer. Acquisition points for the cross-section measurements, shown in black, were collected for half of the cross-section only; since the Gaussian model uses a symmetric formulation, temperatures on both sides are mirrored. Figure 4.5 displays the nodal points.

The contact powder and substrate were omitted; however, the preheating temperature from the substrate was entered as a boundary condition, with the present data set having a predefined temperature of 643 K. In the next chapter, the substrate temperature is analyzed as standalone parameter [10], [20], [21]. Previously produced layers were not modeled in this study; nevertheless, excluding them did not affect the effective thermal conductivity value of the powder

itself. The only perceivable impact occurred on the temperature at the bottom of the new layer, which could achieve higher temperatures than the initial substrate temperature [71]. We have found that different powder diameters at the same packing density have no impact on the final temperature distributions of the model. However, between the three different packing densities the temperature differs.

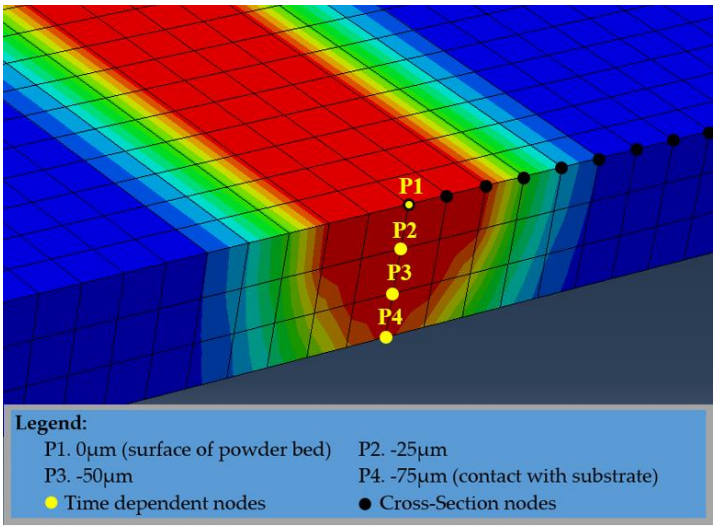

Figure 4.5. Nodal acquisition scheme.

When using a power input of 100 W (P = 100 W; Figure 4.6) with the current configurations of the parameters mentioned, the maximum temperature achieved was ~1575 K at the surface, not enough to reach the melting point of the alloy used. However, it was essential to consider that powder can still melt to a certain degree owing to necking between the small particles. The only concern here is at the bottom (−75 μm), where temperatures only reached 1090 K.

In the same temperature distribution plot, the temperature increases at the same rate for all packing densities. However, as soon as the temperature reaches the maximum value and the laser scan moves forward, the temperature loss differs among each of the configurations. On the second plot in the same graph, SC loses less heat than BCC and FCC. Since SC has the smallest effective

thermal conductivity among all the packing densities, less heat is exchanged. The biggest difference is 45 K (or 3%), between SC and FCC, which occurs at the surface of the powder bed.

Another notable finding from the temperature distributions of P = 100 W is that the cooling rate was very small after the temperature reached its maximum, even though the temperature rises when the number of laser scans is very high. This occurred because the domain was still in the powder state and thus had low thermal conductivity overall. The cooling rate for the top surface (Figure 4.6) is around 60 K/ms for FCC packing density, 37.1 K/ms for BCC, and 25.7 K/ms for SC within the domain modeled.

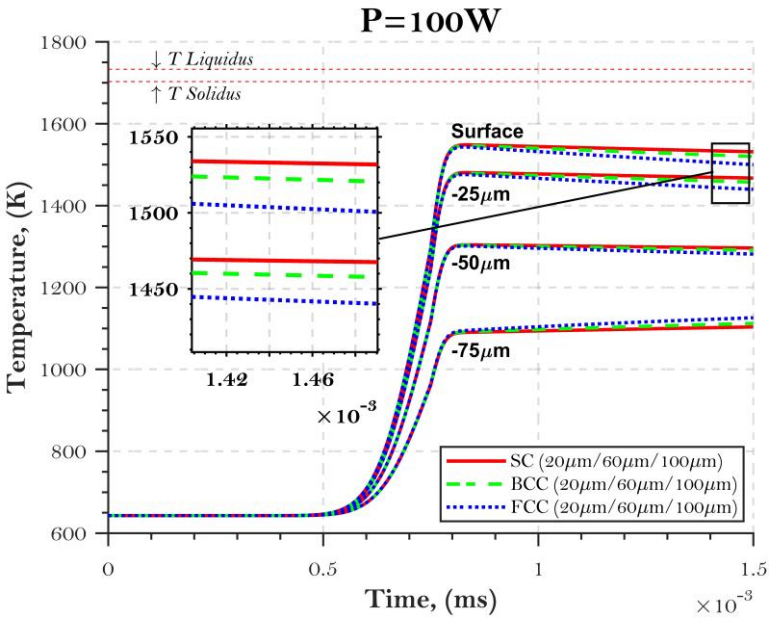

Figure 4.6. Temperature distribution at a power input (P) of 100 W during one scan in the scanning direction.

The cross-section plot in Figure 4.7 shows how the temperature spreads through the powder bed when t = 0.75 ms (maximum temperature achieved), with a HAZ of ~160 μm from the centre of the powder bed. This behavior was observed for all plots (P = 200 and 400 W). The secondary plot shows in detail that the different packing densities had no significant impact on the

temperature profile. Another distinguishable feature from the cross-section plot is the effect of mesh size, which is evident from the sudden temperature rate change at exactly 25 µm, meaning that the mesh was not ideally capturing all the temperature changes. However, a change in mesh size in this model can increase the simulation time up to 4 times.

The cross-sectional temperature distribution for P = 100 W also shows how the temperature gradient between the layers behaves. The top (0 µm) and bottom (-75 µm) surfaces of the powder bed have a $\nabla T_{0\ \mu m \rightarrow -75\ \mu m}$ (temperature gradient) of 460 K in the middle of the powder bed; from the top surface to –25 µm it is 80 K; from –25 µm to –50 µm it is 170 K; and finally, from –50 µm to the bottom surface at –75 µm it was measured to be 210 K. The temperature gradient along the thickness captured for P = 100 W, however, is not considered high among the full-melting consolidation processes.

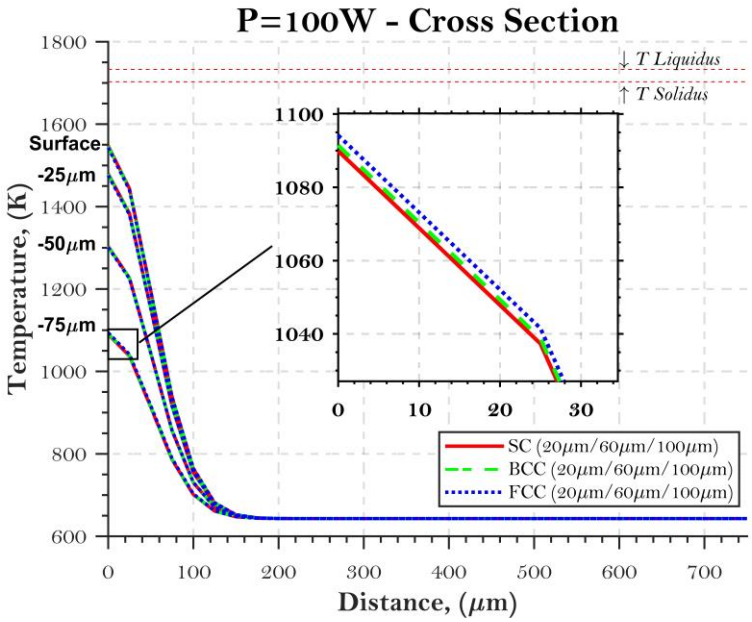

Figure 4.7. Temperature distribution at a power input (P) of 100 W at the cross-section perpendicular to the laser scanning direction.

For P = 200 W in Figure 4.8, the melting point was reached for the surface of the powder bed at –25 and –50 µm. However, the bottom of the powder bed did not reach the melting point, with the temperature remaining at 1525 K, whereas the surface reached 1900 K. This led to a high exchange of heat after the laser had scanned through, and it is evident how the bottom point (–75 µm) still increased from 1525 to 1675 K in less than 0.7 ms. The packing densities here do not display an apparent temperature difference, since there is only a 4 K difference between SC and FCC on the bottom node, as shown in the second plot. As confirmation of the role of powder diameter in the temperature distribution, Table 4.2 list the five last increments corresponding to the three powder diameters under SC packing density. There are only fluctuations of temperature, with no significant changes, which explains the overlap of all the temperature distributions at different powder diameters. In fact, researchers studying the effects of individual powder particle interactions using DEM models found significant effects of powder diameter on temperature distributions [50], but this parameter was not within the scope of the present study.

Table 4.2. Temperature in the last five time increments at –75 µm and *P* = 200 W for simple cubic (SC) packing density.

Time increment (*t*)	**Temperature (K)**		
	20 µm SC	60 µm SC	100 µm SC
1.4940 ms	1683.71	1683.34	1683.52
1.4955 ms	1683.83	1683.46	1683.65
1.4970 ms	1683.96	1683.59	1683.77
1.4985 ms	1684.08	1683.71	1683.89
1.5000 ms	1684.20	1683.83	1684.01

At –50 µm, after the laser scans through, the temperature remains within the solidus and liquidus temperatures, owing to the effect of the latent heat of fusion. Interestingly, the top surface (0 µm), –25 µm, and bottom surface (–75 µm) are all converging around the mushy zone, which

is defined as the zone between the solidus and liquidus temperatures. This means that high energy is concentrated on those regions and heat is exchanged accordingly until a steady state is achieved.

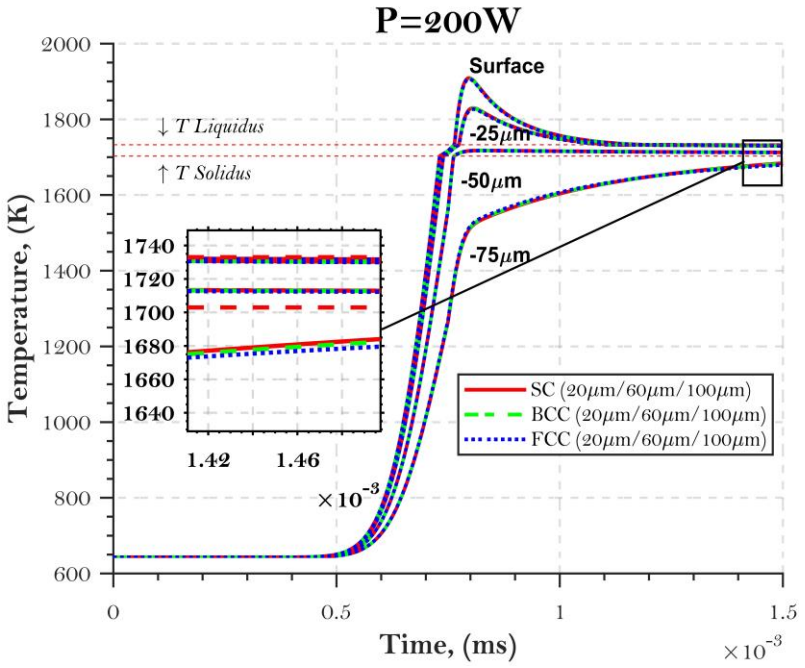

Figure 4.8. Temperature distribution at a power input (*P*) of 200 W during one scan in the scanning direction.

The impact of the packing density is no longer visible for the top surface, –25 µm, and –50 µm. The impact is only observable for the bottom surface; however, there is a very small temperature difference between the packing densities. It is evident that the impact of packing density on temperature distribution diminishes when the temperature crosses the melting point.

From the cross-sectional temperature distribution for *P* = 200 W (Figure 4.9), we observed the following temperature gradients: from the top (0 µm) and bottom (–75 µm) surfaces of the powder bed $\nabla T_{0\ \mu m \rightarrow -75\ \mu m}$ = 380 K; from the top surface to –25 µm it is 70 K; from –25 µm to –50 µm it is 100 K; and finally, from –50 µm to the bottom surface at –75 µm it is 210 K. When

comparing these results with those obtained for P = 100 W, these gradients are actually 80 K lower, representing a relatively better condition for solidification, since a higher temperature gradient can induce residual stresses and consequently warpage and deformations in the built part.

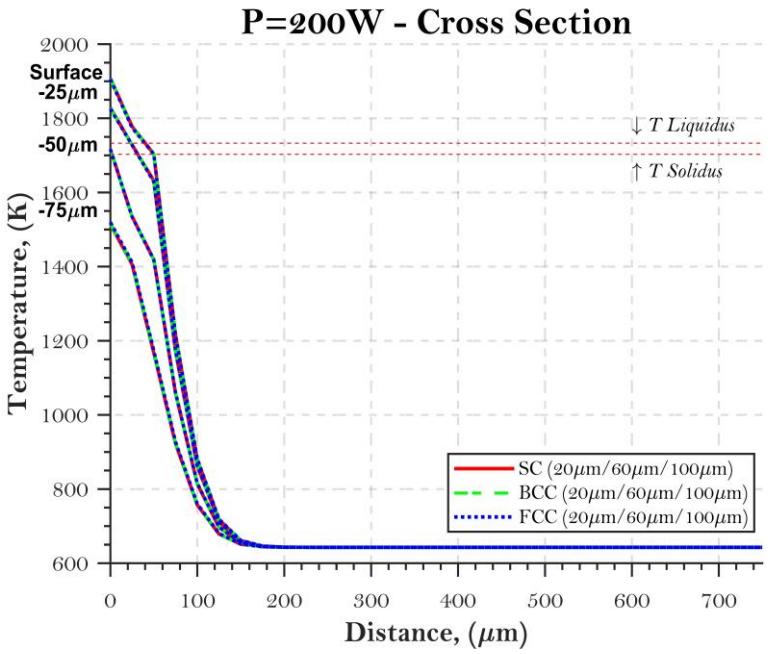

Figure 4.9. Temperature distribution at a power input (P) of 200 W at the cross-section perpendicular to the laser scanning direction.

The last power input (P = 400 W) is the only one in which the entire depth of the powder bed layer reached the melting point. However, the maximum temperature achieved at the surface was ~3250 K, which is an undesirable condition that can lead to the evaporation of the metal [69]. The bottom reached ~2100 K, which would most likely induce the melting of the substrate or increase the HAZ of the same. It is noteworthy that a gradient of ~1100 K between the top and bottom layers was induced, whereas at P = 100 W the gradient was 450 K and at P = 200 W the gradient was 400 K. This fact alone is extremely important when analyzing residual stresses during SLM, as explained previously.

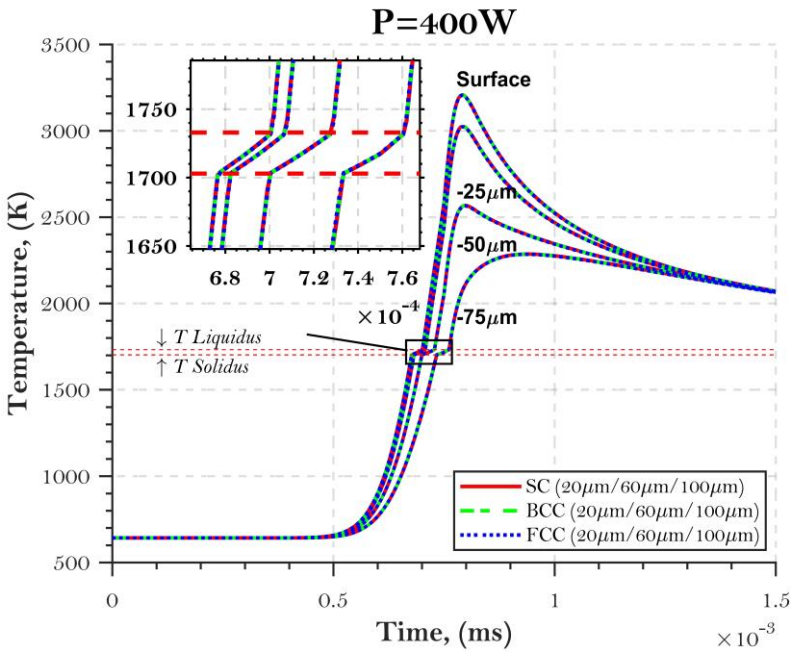

Figure 4.10. Temperature distribution at a power input (*P*) of 400 W during one scan in the scanning direction.

In the secondary plot shown in Figure 4.10, the melting point area between solidus and liquidus temperature (broken red line) is highlighted. The rate of temperature change in this interval proves that the model is capable of interpreting the different property states and the phase change caused by the latent heat of fusion even when using a small time increment.

The cross-sectional temperature gradients for P = 400 W (Figure 4.11) were the highest achieved in this study. The following temperature gradients were observed: from the top (0 µm) and bottom (–75 µm) surfaces of the powder bed $\nabla T_{0\ \mu m \rightarrow -75\ \mu m}$ = 1100 K; from the top surface to –25 µm it is 200 K; from –25 µm to –50 µm it is 450 K; and finally, from –50 µm to the bottom surface at –75 µm it was measured to be 450 K.

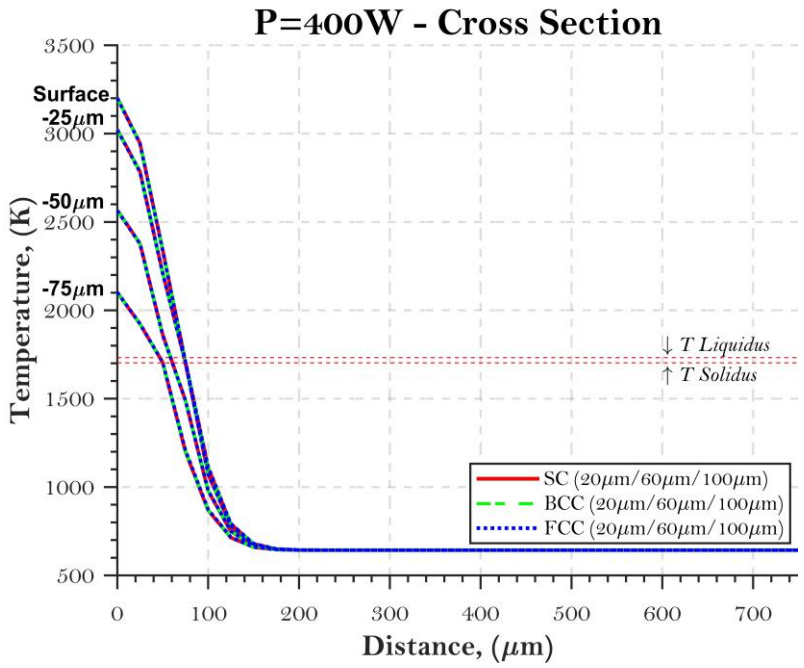

Figure 4.11. Temperature distribution at a power input (*P*) of 400 W at the cross-section perpendicular to the laser scanning direction.

4.6.2 Melt pool behavior for T_0 = 643 K

Identifying the melt pool region in SLM processes is important for determining the HAZ of each scanned track. Usually the melt pool exceeds the diameter of the laser beam depending on parameters such as scanning speed and power input. The following results are for a substrate temperature of 643 K, SC packing density, and 20 µm powder diameter.

When using *P* = 100 W, the powder does not effectively melt. Temperature distributions are kept below the melting point through the entire thickness of the layer, as shown previously. Figure 4.12 shows the cross-section along two planes. For *P* = 200 W (Figure 4.13a), the maximum temperature value was fixed at 1733 K, thus the grey region in the temperature field corresponds to the melt pool region. It is evident that the comet shape formed in the melt pool region, a feature

that was expected, since the Goldak heat flux input used in the current model resembles this shape [72]. Note that all temperatures are expressed in degrees kelvin (K).

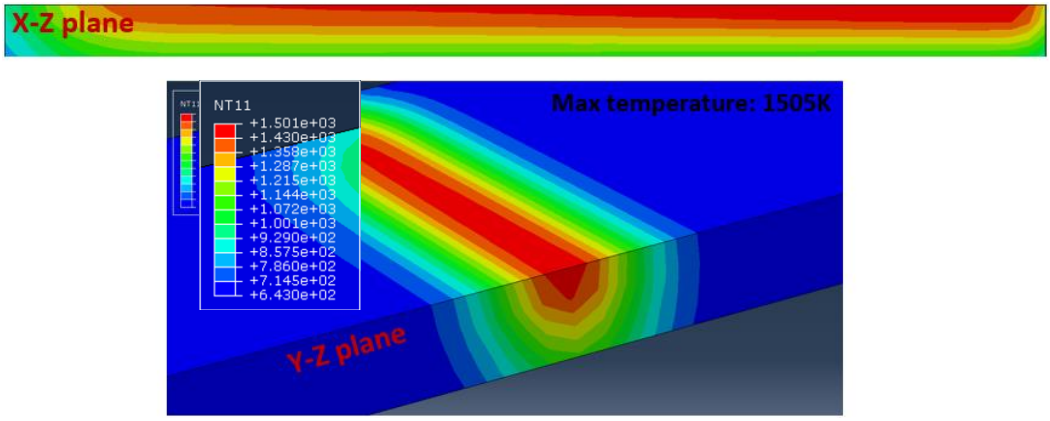

Figure 4.12. *X*–*Z* cross-section (top) and *Y*–*Z* cross-section (bottom).

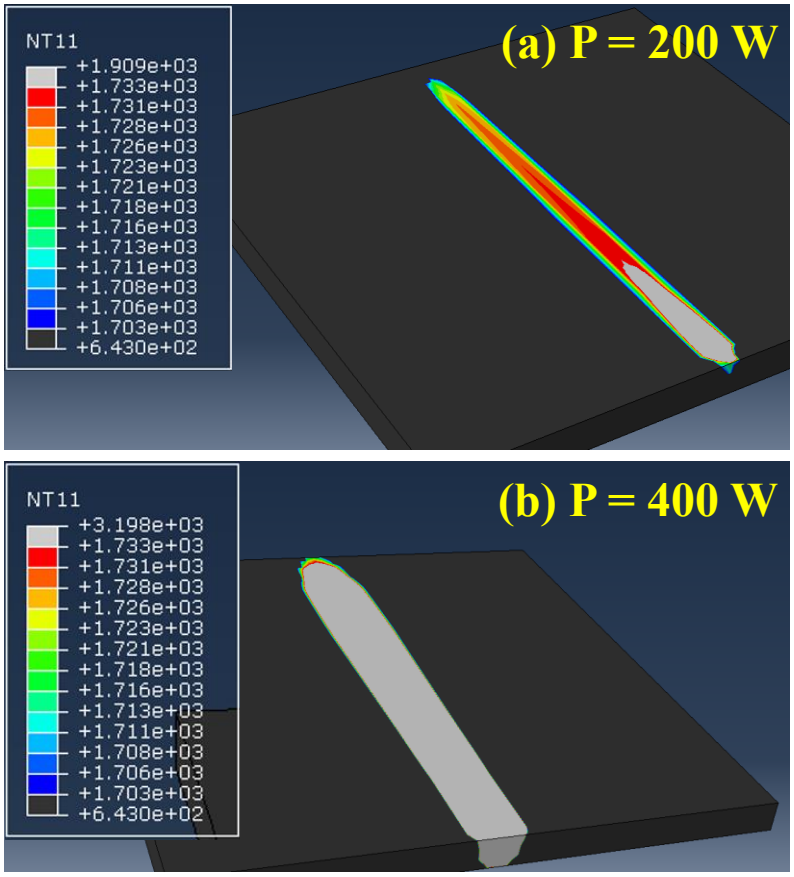

Figure 4.13. Melt pool area at 1.5 ms for P = 200 W (a) and P = 400 W (b).

The molten material at P = 400 W (Figure 4.13b) occurs along the entire distance of the bed scanned by the laser and through all the powder bed thickness as well. It is apparent, in the beginning of the track, that the melt pool area increases in width over time. This change indicates that the melt pool has high energy and is exchanging heat with the nearby powder, thereby melting it and increasing the HAZ.

Regarding the melt pool dimensions for P = 200 and 400 W, the feasibility of using a power input of 200 W is evident, given the small HAZ present. Figures 4.14 and 4.15 show the melt pool size for P = 200 and 400 W along different cross-sections.

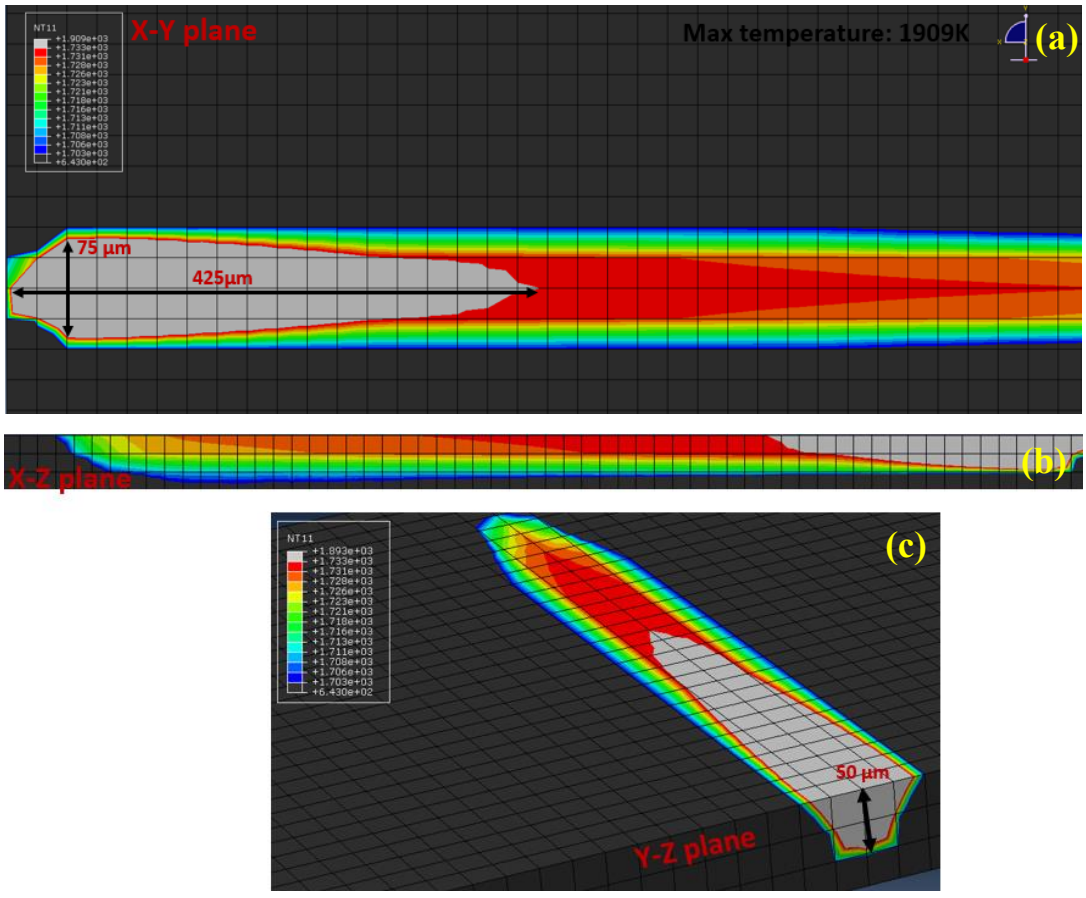

Figure 4.14. Melt pool dimensions in the last time increment for P = 200 W. X–Y plane (a), X–Z plane (b), and Y–Z plane (c).

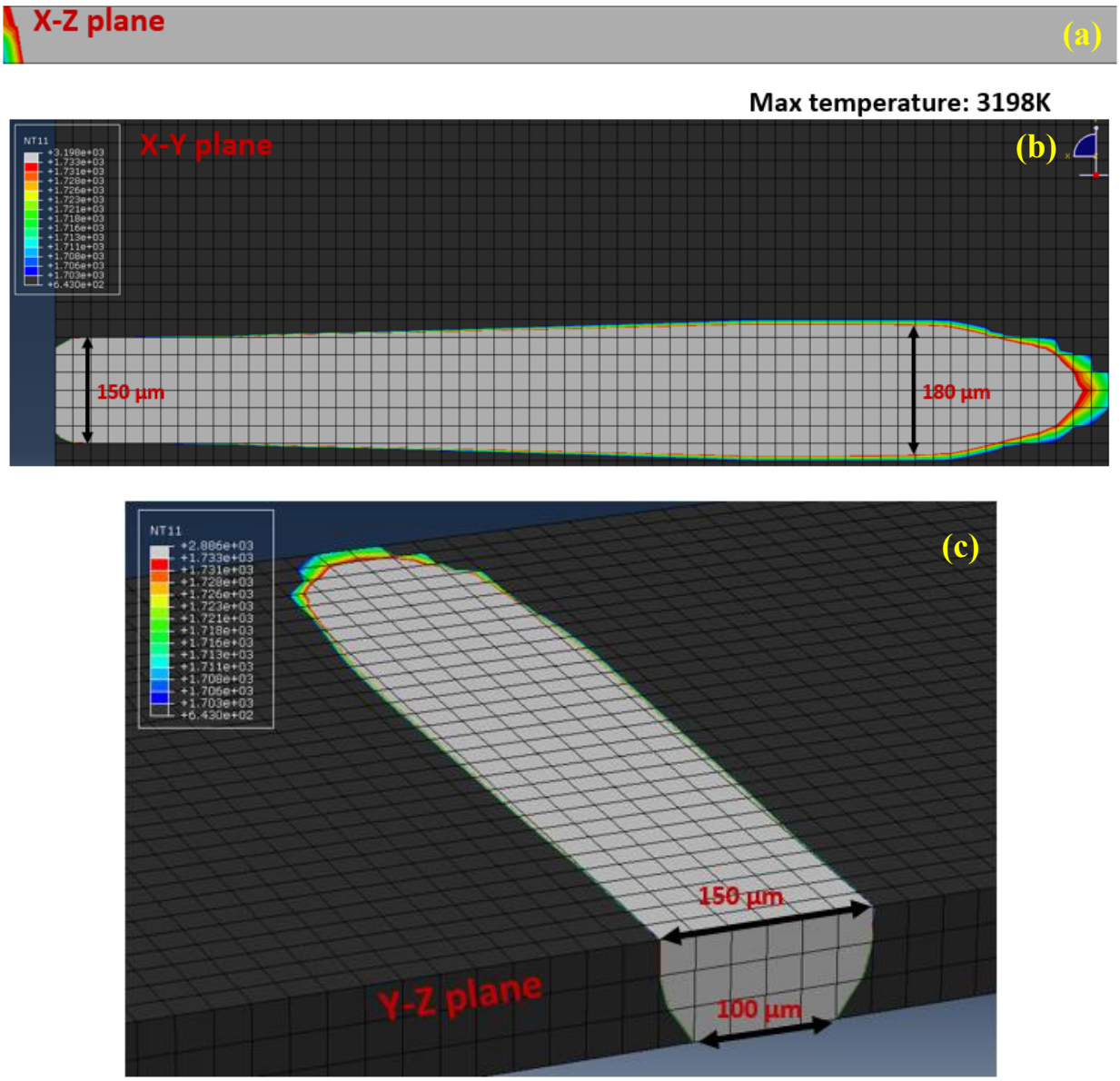

Figure 4.15. Melt pool dimensions in the last time increment for P = 400 W. X–Z plane (a), X–Y plane (b), and Y–Z plane (c).

The material becomes fully molten at P = 200 W up to –50 µm; the light grey in Fig. 4.14 and 4.15 represents the region where temperatures exceed 1733 K (T_{liquidus}). The remaining colours are in the range of 1703–1733 K, representing the mushy zone, a mixture of solid and liquid material. Finally, the dark grey represents temperatures below 1703 K (T_{solidus}). The dimension of the melt

pool at P = 200 W is 75 µm × 425 µm, a width that it is 1.5 times larger than the laser beam diameter used in the model.

On the other hand, at P = 400 W, the whole thickness of the layer is above the melting point, with 100 µm of the width in the bottom surface and 150 µm on the top of the powder bed 3 times larger than the laser beam diameter. The entire track is molten as well (750 µm of length), and at the end of the laser scanning period, at 1.5 ms, the melt pool width at the beginning scan point is ~180 µm.

The remaining packing density and powder diameter data sets have not been compiled here, since the previous sensitivity analysis showed that they have a very small impact on temperature distributions overall. The next section covers the topic of substrate temperature in detail.

4.6.3 Sensitivity analysis of substrate temperature

The substrate temperature, T_0, was previously set at 643 K (370 °C), which is a common value used for stainless steel [78]. To investigate the impact of the substrate temperature, two more data sets were simulated, one with T_0 = 298 K (25 °C) and the other with T_0 = 373 K (100 °C). The SLM process has substrate temperature range of 20 to 550 °C according to SLM Solutions, while DMLS has a substrate temperature range of 20 to 100 °C according to EOS GmbH [10], [17]. A study performed by Li et al. [79] demonstrated how substrate temperature influences the built part, since it plays an important role in defining the interface bonding between the substrate and the part as well as the microstructures of the final part. The authors concluded that higher substrate temperature increased the quality of the bond and can be attributed to the high cooling rate and larger melt-pool volume. A lower substrate temperature initially has a higher cooling rate; however, the small melt pool induced is responsible for forming a strong boundary and gap in

between the part and the substrate, preventing an effective heat transfer from the part to the substrate and resulting in a reduction of the actual cooling rate [79].

In the model, the substrate temperature was entered as a boundary condition for all data sets, but mechanical contact between the interfaces was ignored, since the focus here was thermal behavior. Figure 4.16 presents the results for T_0 = 298 K for all power inputs, packing densities, and powder diameters, and Figure 4.17 shows the results for T_0 = 373 K. Since the previous sections covered temperature distribution behavior in depth, here the plots were placed side by side to show the longitudinal temperature distribution and its cross-sectional counterpart.

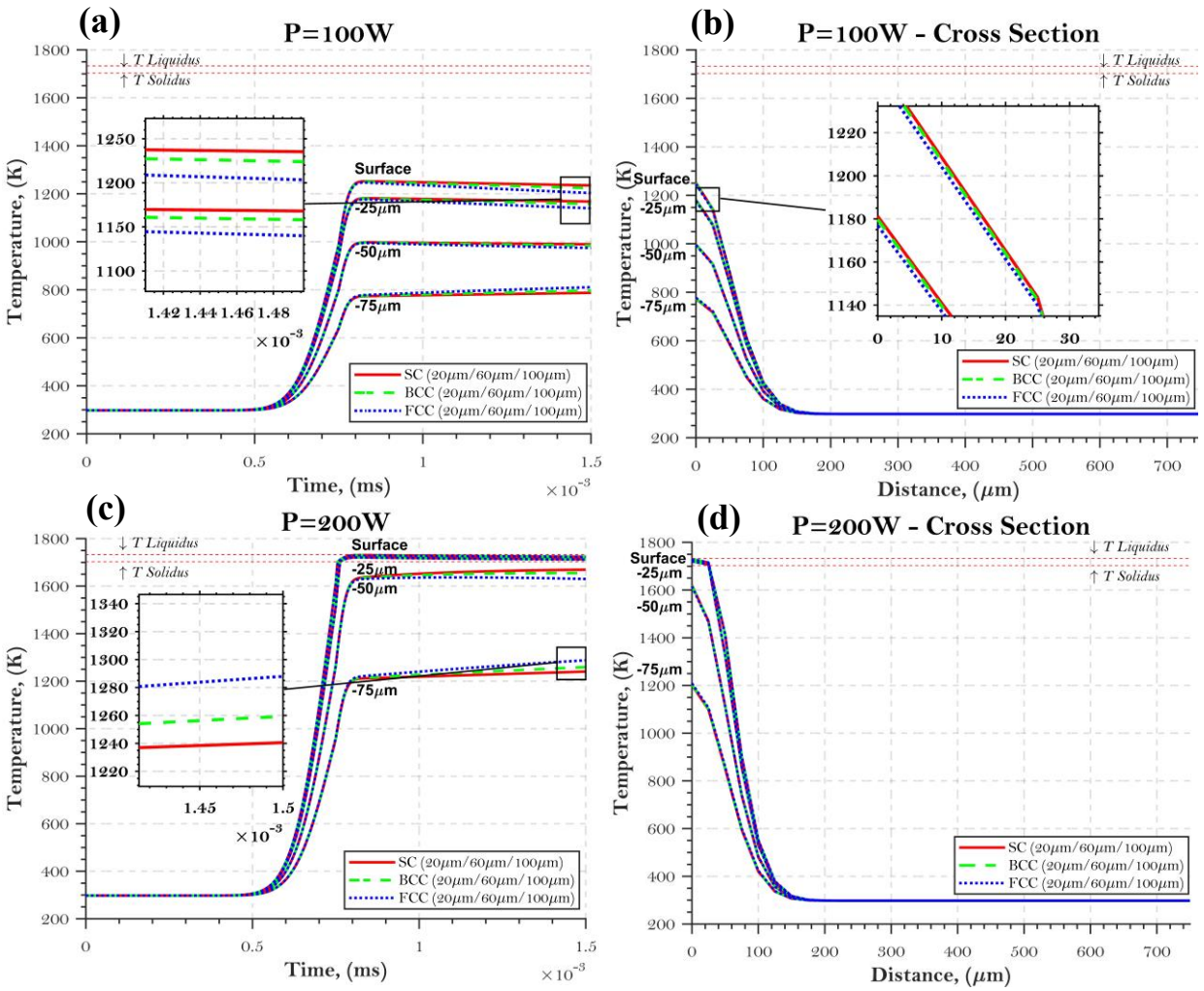

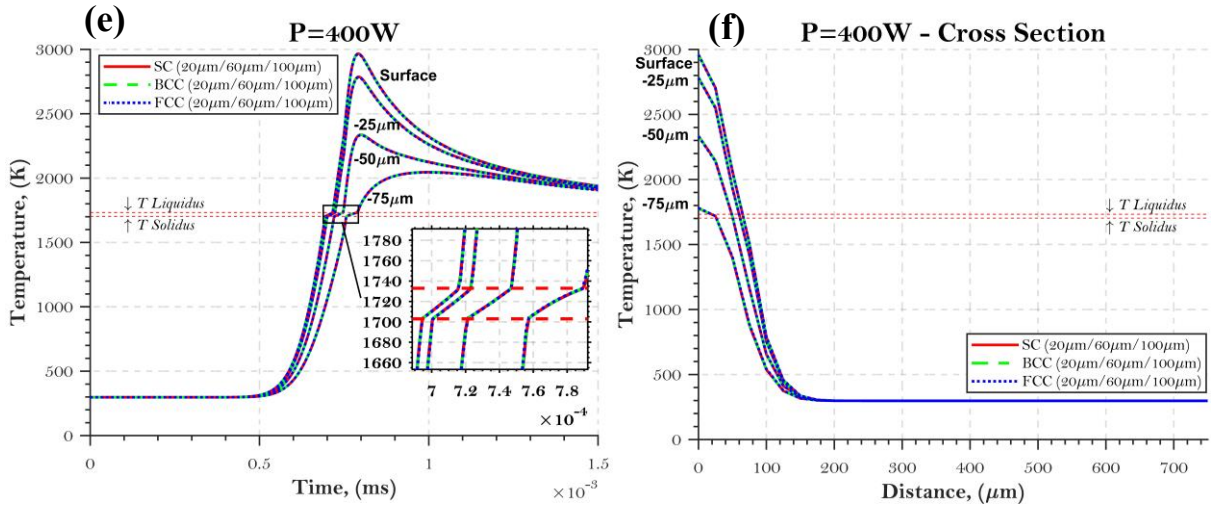

Figure 4.16. Temperature distribution for T_0 = 298 K at P = 100 W (a), P = 200 W (c), and P =400 W (e) and their corresponding cross-sections in (b), (d), and (f).

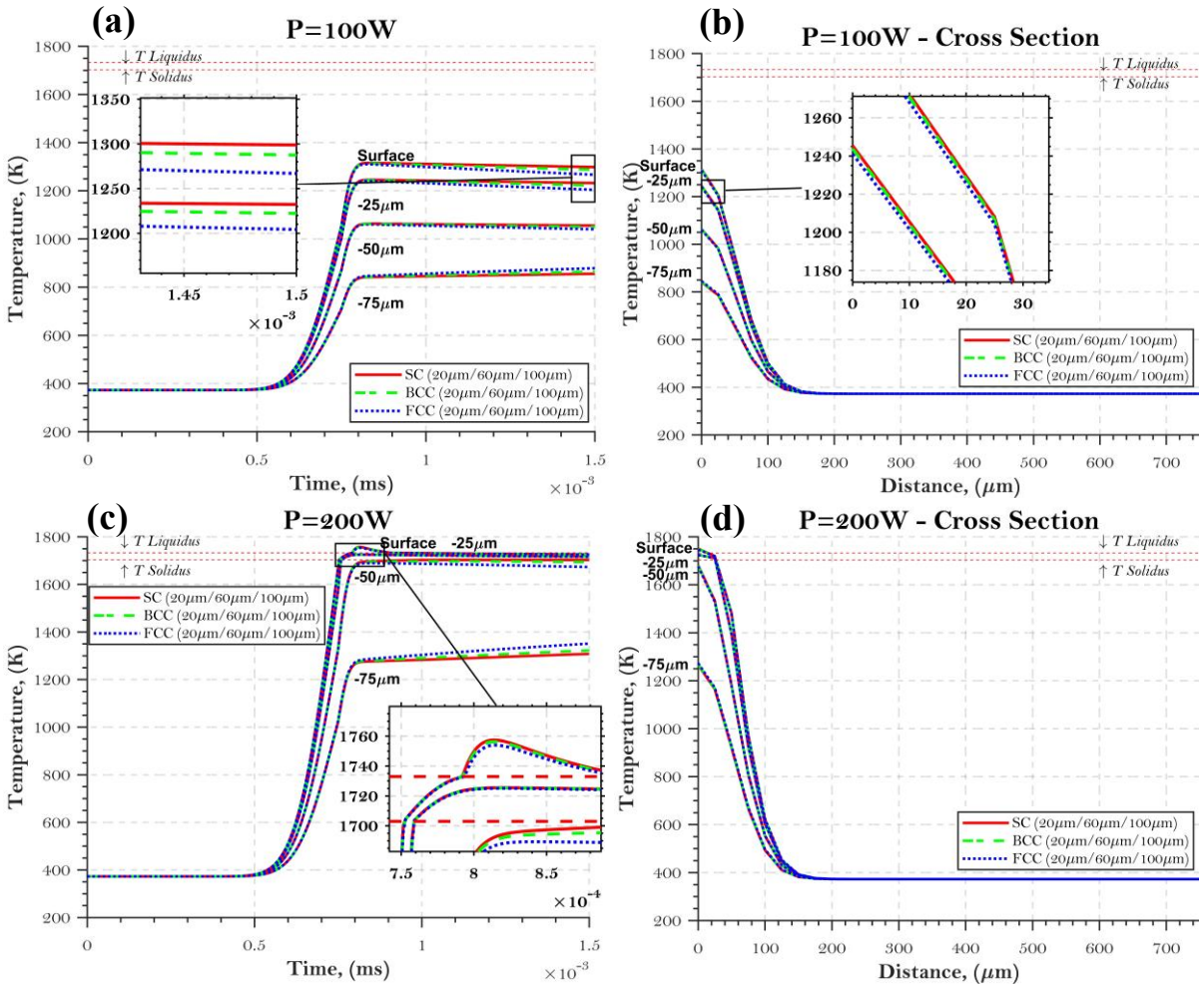

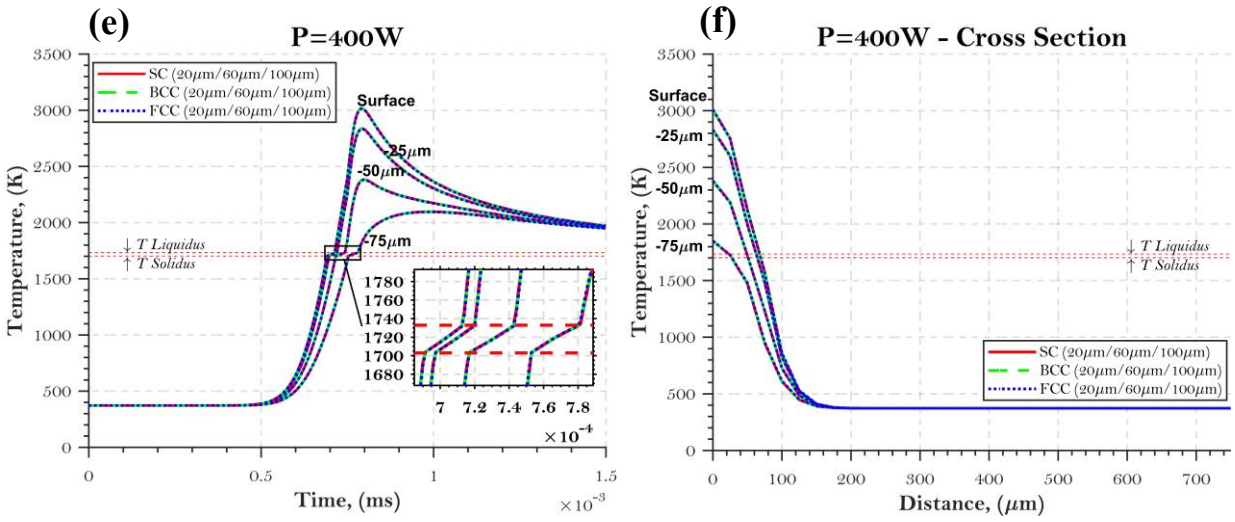

Figure 4.17. Temperature distribution for T_0 = 373 K at P = 100 W (a), P = 200 W (c), and P =400 W (e) and their corresponding cross-sections in (b), (d), and (f).

It is clear that by increasing the substrate temperature, the maximum temperature achieved increases as well. However, the temperature gradients measured through the thickness of the layer decreases, as shown in Table 4.3. The main implication of the results is that an increase in the substrate temperature causes the powder bed to use less energy from the heat flux, consequently decreasing the temperature gradient through the layer thickness. However, this increase is not linear, meaning that a rise of 100 K in the temperature does not bring about a 100 K change in the temperature distribution obtained. Thus, the complexity of the simulation is evident.

The best scenario among all simulations is P = 200 W and T_0 = 643 K, with a lower gradient of 380 K between the bottom and top surfaces. Although P = 100 W has a lower heat flux, it inputted a higher temperature gradient when compared with P = 200 W, mainly because the former condition did not cause the substrate to reach the melting point and the latter resulted in one or more points through the layer thickness being above the melting point or in the mushy zone. When

the material is in the mushy zone, it requires a great deal of energy to change the state (solid to liquid), and thus the gradient was reduced in the case of P = 200 W.

Table 4.3. Temperature gradients (∇T) and maximum temperature (T_{Max}; in kelvin) for all simulated substrate and power conditions.

		T_0 = 298 K	T_0 = 373 K	T_0 = 643 K
P = 100 W	T_{Max}	1250	1300	1550
	$\nabla T_{0\ \mu m \rightarrow -25\ \mu m}$	70	50	80
	$\nabla T_{-25\ \mu m \rightarrow -50\ \mu m}$	180	220	170
	$\nabla T_{-50 \mu m \rightarrow -75\ \mu m}$	225	200	210
	$\nabla T_{0\ \mu m \rightarrow -75\ \mu m}$	475	470	460
P = 200 W	T_{Max}	1733	1760	1900
	$\nabla T_{0\ \mu m \rightarrow -25\ \mu m}$	3	40	70
	$\nabla T_{-25\ \mu m \rightarrow -50\ \mu m}$	110	30	100
	$\nabla T_{-50\ \mu m \rightarrow -75\ \mu m}$	420	400	210
	$\nabla T_{0\ \mu m \rightarrow -75\ \mu m}$	533	470	380
P = 400 W	T_{Max}	2950	3000	3200
	$\nabla T_{0\ \mu m \rightarrow -25\ \mu m}$	150	170	200
	$\nabla T_{-25\ \mu m \rightarrow -50\ \mu m}$	450	430	450
	$\nabla T_{-50\ \mu m \rightarrow -75\ \mu m}$	560	550	450
	$\nabla T_{0\ \mu m \rightarrow -75\ \mu m}$	1160	1150	1100

4.7 Verification and Conclusions

The parametric low-cost FEM thermal model proposed in this chapter is capable of measuring temperature distributions through a powder bed, and consequently the temperature gradient, of a single layer and track of laser scanning using the SLM process. Parameters such as power input, powder diameter, powder packing density, and substrate temperature were analyzed. Packing density and powder diameter influenced the effective thermal conductivity of the power, as seen in chapter 3, and these parameters were implemented in the simulation.

The only considerable effects of both powder diameter and powder packing density that are visible in the temperature distribution were found for lower power input (P = 100 W) and only for different packing densities. The powder diameter did not have a major impact on the outcome, which can be attributed to the minor change in effective thermal conductivity that occurred, regardless of packing density, and because the model was based on the total volume occupied by the particles as a whole, and thus the individual particle interactions are not accounted for. The packing density effects are perceived for temperatures below the melting point, since the model of effective thermal conductivity is calculated from 300 to 1703 K. The SC packing density has the lowest k_{eff} and thus lower cooling rates when comparing to BCC or FCC, as seen in the temperature distributions for power input of 100 W. The maximum difference of temperature (ΔT) achieved between SC and FCC was 45 K at the top surface of the powder bed at 100 W; for 200 W, the difference was minor, only perceivable at –75 μm with ΔT = 5 K; and finally, for 400 W, the packing density did not influence the temperature distributions at all, since all the layers were above the melting point.

Power input and substrate temperature played a major role in the analysis, with all the scenarios having specific implications:

- P = 100 W was the lowest power input at which temperatures did not reach the melting point. According to Gibson, powder can sinter at half melting point temperatures, and in the current investigation the T_{Max} achieved was around 1500 K for T_0 = 643 K. The T_{Solidus} of the material was 1703 K, more than enough for necking to occur among the particles. However, we cannot draw further conclusions on the degree to which the material would effectively consolidate, since the temperature mentioned is only at the

surface of the powder bed; on the bottom surface, the temperature was 1100 K, sufficient to start the sintering between the particles as well, but at a smaller scale. T_0 = 643 K is strongly recommended to be used with P = 100 W, given the statements mentioned before, but when using T_0 = 298 K and T_0 = 373 K, the T_{Max} achieved was around 1250 and 1300 K, respectively, and the T_{Min} around 775 and 850 K, on the threshold for the sintering condition mentioned by Gibson and thus not enough to fully consolidate the material;

- P = 200 W is the ideal situation among all the power inputs analyzed, given the melt pool behavior and the temperature gradients. For T_0 = 643 K, we achieved the optimal temperature gradient of 380 K, the lowest of all the conditions simulated, and thus this temperature is strongly recommended for use with this power input. The main reason is that the temperature distribution was just enough to reach the $T_{Solidus}$ for h = 0 µm, –25 µm, and –50 µm, with a T_{Max} = 1900 K. In this case, when the temperatures are between the $T_{Solidus}$ and $T_{Liquidus}$, the latent heat of fusion plays an important role, consuming most of the heat to change the phase either from the solid state to liquid and vice versa. For this reason, the temperature gradient is fairly small when compared with other power inputs, and even for the other substrate temperatures;
- P = 400 W is strongly not recommended as a power input to be used for SS-304L, the reason being that temperatures reached 3200 K when using T_0 = 643 K, with temperature gradient of 1100 K between the top and bottom of the powder bed. In addition, the entire thickness of the powder bed exceeded the melting point, and the melt pool observed and consequently the HAZ were very large, indicating that re-melting from previously layers or substrate could occur.

Overall, the observed temperature distributions very closely followed the behavior of SS-304L in other experimental studies found in the literature. Abd-Elghany and Bourel printed SS-304L to investigate its mechanical properties using different setups. The authors produced manufactured specimens using a machine with power input of 100 W and 30, 50, and 70 μm layer thicknesses, concluding that higher layer thickness produced specimens with low density and poor mechanical properties [33]. This can be used as a reference to our setup of P = 100 W and layer thickness of 75 μm, in which case the laser input was not enough to bring the temperature to the melting point, and thus consolidation between powder particles was poor.

In the next chapter, results are presented for samples produced by a process analogous to SLM, using SS-316L. The analysis is concentrated on the relative densities of the samples, the porosity, and finally residual stress measurements and microscopic characterization.

5 DIRECT METAL LASER SINTERING EXPERIMENTAL SETUP

The experimental setup is designed to verify the model and demonstrate how parameters play an important role in the final part printed using PBF processes. Specimens were produced using a commercially available machine, EOS GmbH model M280. This industrial 3D printer uses the PBF process known as DMLS. SS-316L was the material selected for the experiments, given the similarity in its thermal properties with SS-304L, the material used in the previous chapter. The part was built in the AM laboratory at McMaster University facilities in Hamilton, Ontario, Canada.

5.1 Stainless Steel 316L Powder

The powder used to manufacture the parts was supplied by EOS, with a powder size distribution of 15–45 μm and a composition described in Table 5.1.

Table 5.1. Chemical composition of EOS stainless steel 316L [17].

Element	Nominal composition (%) of SS-316L powder
Fe	Balance
Cr	17.00/19.00
Ni	13.00/15.00
Mo	2.25/3.00
C	0.030
Mn	2.00
Cu	0.50
P	0.025
S	0.010
Si	0.75
N	0.10

The thermal properties of the material utilized in the experiment, SS-316L, is highly analogous with SS-304L utilized at chapter three and four. The similarity can be perceived at Figure 5.1 below [56].

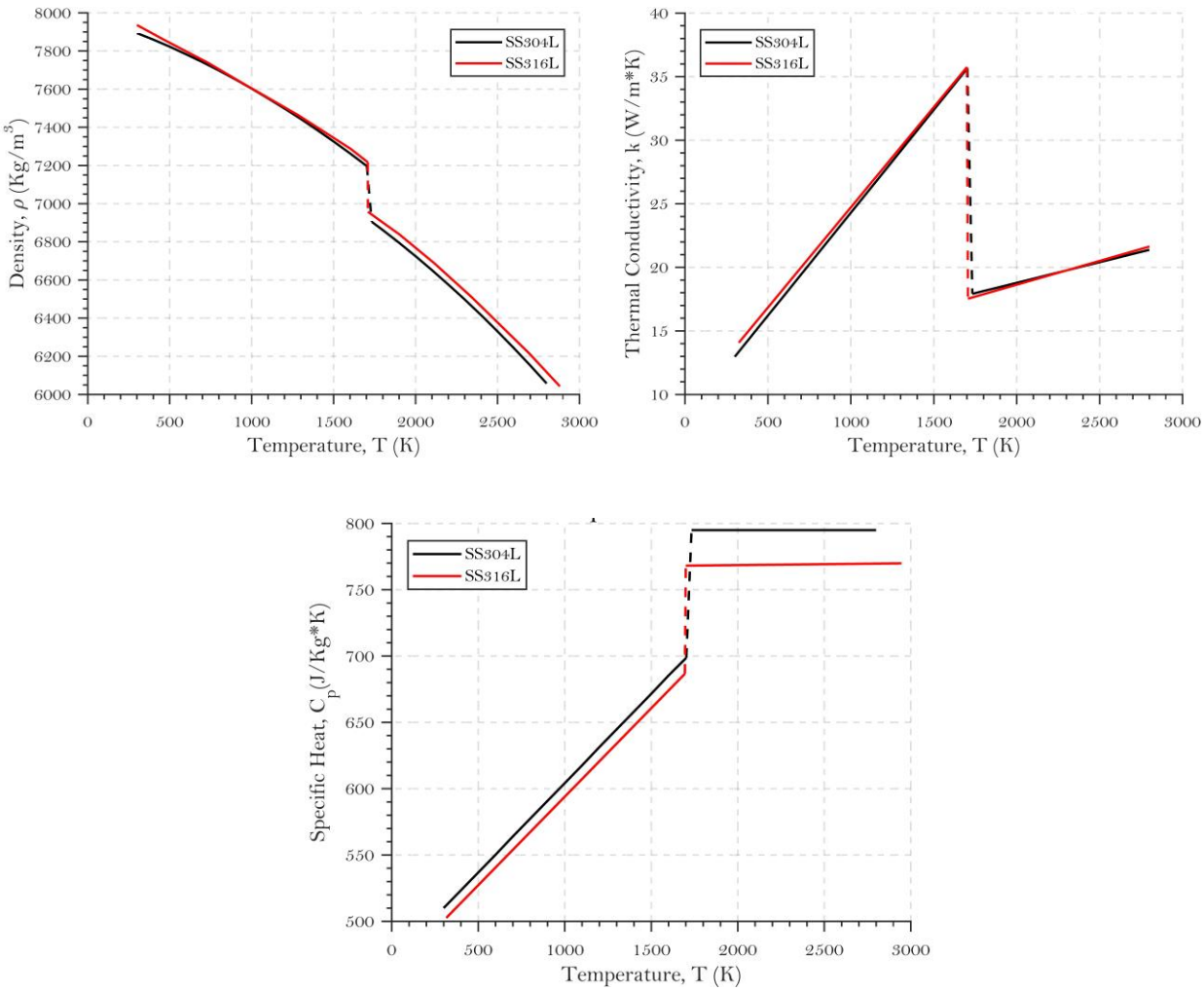

Figure 5.1. Thermal properties of SS-304L and SS-316L [56].

The total volume of the powder bed envelope was calculated before the manufacturing process began, and this value was used to calculate how much material needed to be loaded in the machine. Although there is no proper recommendation from the machine manufacturer as to how much material must be loaded, the laboratory recommends loading 3 times the total weight of the powder

bed volume. With an envelope volume of ~938 cm^3 and a powder density of 8.05 g/cm^3, we calculated a total powder mass of 7547 g, resulting in a total of 22.6 kg being used for the experiment.

The reason for using such a large amount of raw material is that the powder is then equally distributed through the powder bed, which has dimensions of 25 cm × 25 cm, and the sample has a height of 1.5 cm. The roughly three times estimation of material that must be added is a safety measure in order to overcome powder loss through evaporation, contamination, and airborne particles that is spread to other surfaces inside the machine chamber. In total, we used roughly 4.16 kg of material, which ≈1.9 kg was the weight of the batch. The remaining 18.44 kg was recycled; however, the powder had to be sifted to remove oxide powder and agglomerated particles that exceeded the maximum size allowed for reuse. This was one more reason for the large rate of material loss in the process.

5.2 Designing the Experimental Setup

The experiment setup was designed to effectively demonstrate the significance of the parameters on the relative density and residual stresses of the final part. One batch of samples was manufactured; thus, layer thickness and substrate temperature were the fixed parameters of the built part, since they cannot be modified within the same batch. The machine chamber is filled with nitrogen gas, and gas flow is directional along the powder bed. Power input (P), scanning speed (v), and hatch distance (s) were the main parameters analyzed; beam offset, stripe overlap, and stripe width are the remaining build parameters; however, they were set as constant, since it was not our main objective to study their effect in the built samples. Nevertheless, the scanning strategy on the EOS machines cannot be modified, as it uses a 67° scanning angle and stripe raster

strategy with 10 mm width. These settings did not affect the setup in the current study, since the scanning strategies were not analyzed. The samples were designed to have dimensions of 20 mm × 20 mm × 15 mm, following a requirement from the X-ray diffraction equipment of a minimum 10 mm × 10 mm surface and having a minimum of a two-stripe width in the top scanning surface.

The three parameters defined in the sample grouping (*P*, *v*, and *s*) have their own ranges as determined by the machine manufacturer. Table 5.2 shows the range for all parameters of EOS M280.

Table 5.2. Range of parameters for the EOS M280 3D printer [17].

	Min. value	**Max. value**	**Increment**
Layer thickness (µm)	20	50	10
Hatch distance (µm)	10	400	10
Scanning speed (mm/s)	50	7000	1
Power input (W)	1	370	1
Substrate temperature (K)	293	373	1

Following the parameter ranges and based on the literature review conducted, particularly the results of studies by Mower and Long [80] and Ghasri-Khouzani et al. [81] shown in Table 5.3, we determined the experimental range of parameters for this study.

Table 5.3. Common parameters applied for SS-316L using direct metal laser sintering.

	Speed (mm/s)	**Power (W)**	**Temperature (K)**	**Layer thickness (mm)**	**Hatching (mm)**
Mower et al. [80]	750	195	355	40	—
Ghasri-Khouzani et al. [81]	1083	195	353	20	80

The layer thickness was fixed at 30 µm, with a constant substrate temperature of 353 K. The scanning speed was varied from 250 to 1750 mm/s at an increment of 500 mm/s; the laser power

input was varied from 150 to 250 W at an increment of 50 W; and finally, the hatching distance was varied from 80 to 140 µm at an increment of 20 µm. Table 5.4 show how the groups were created with the following nomenclature: G1–G4 were used to define the hatch distance groups; next, A–D were used to define the scanning speed; and finally, 1–3 specified the power input used. The samples were placed according to their laser energy density values, as explained in chapter 2. In total, 48 samples were programed to be printed; however, due to technical problems, 10 samples had to be left out of the study, as they could not be completed. In the next section a full explanation is provided. The samples removed from the experiments are highlighted in red below.

Table 5.4. Designed range of parameters and groups.

		1 (*P*=150W)	**2** (*P*=200W)	**3** (*P*=250W)
G1 (*s*=80µm)	(*v*=250 mm/s) **A**	G1A1	G1A2	G1A3
	(*v*=750 mm/s) **B**	G1B1	G1B2	G1B3
	(*v*=1250 mm/s) **C**	G1C1	G1C2	G1C3
	(*v*=1750 mm/s) **D**	G1D1	G1D2	G1D3
G2 (*s*=100 µm)	(*v*=250 mm/s) **A**	G2A1	G2A2	G2A3
	(*v*=750 mm/s) **B**	G2B1	G2B2	G2B3
	(*v*=1250 mm/s) **C**	G2C1	G2C2	G2C3
	(*v*=1750 mm/s) **D**	G2D1	G2D2	G2D3
G3 (*s*=120µm)	(*v*=250 mm/s) **A**	G3A1	G3A2	G3A3
	(*v*=750 mm/s) **B**	G3B1	G3B2	G3B3
	(*v*=1250 mm/s) **C**	G3C1	G3C2	G3C3
	(*v*=1750 mm/s) **D**	G3D1	G3D2	G3D3
G4 (*s*=140µm)	(*v*=250 mm/s) **A**	G4A1	G4A2	G4A3
	(*v*=750 mm/s) **B**	G4B1	G4B2	G4B3
	(*v*=1250 mm/s) **C**	G4C1	G4C2	G4C3
	(*v*=1750 mm/s) **D**	G4D1	G4D2	G4D3

5.2.1 Samples placement in the substrate plate

Three modes of heat exchange are happening at once when the machine is manufacturing the samples: conduction between powder and substrate; convection between inert gas and chamber-exposed surfaces (including powder and substrate); and radiation due to high temperatures induced

by the fiber laser. There is a gas duct on the side of the powder bed providing directional gas flow through the powder bed surface, thus cooling down the melted material. For this reason, we designed the position of the samples to maximize convection heat exchange: we placed the samples with higher laser energy density closer to the duct where the gas was being emitted and the samples with lower energy density on the opposite side.

The calculated laser energy density E_v (J/mm³) for each sample and their positions are shown in Figure 5.2. The samples that were excluded from the batch owing to a technical manufacturing failure have red values; the successfully printed samples are indicated by blue values.

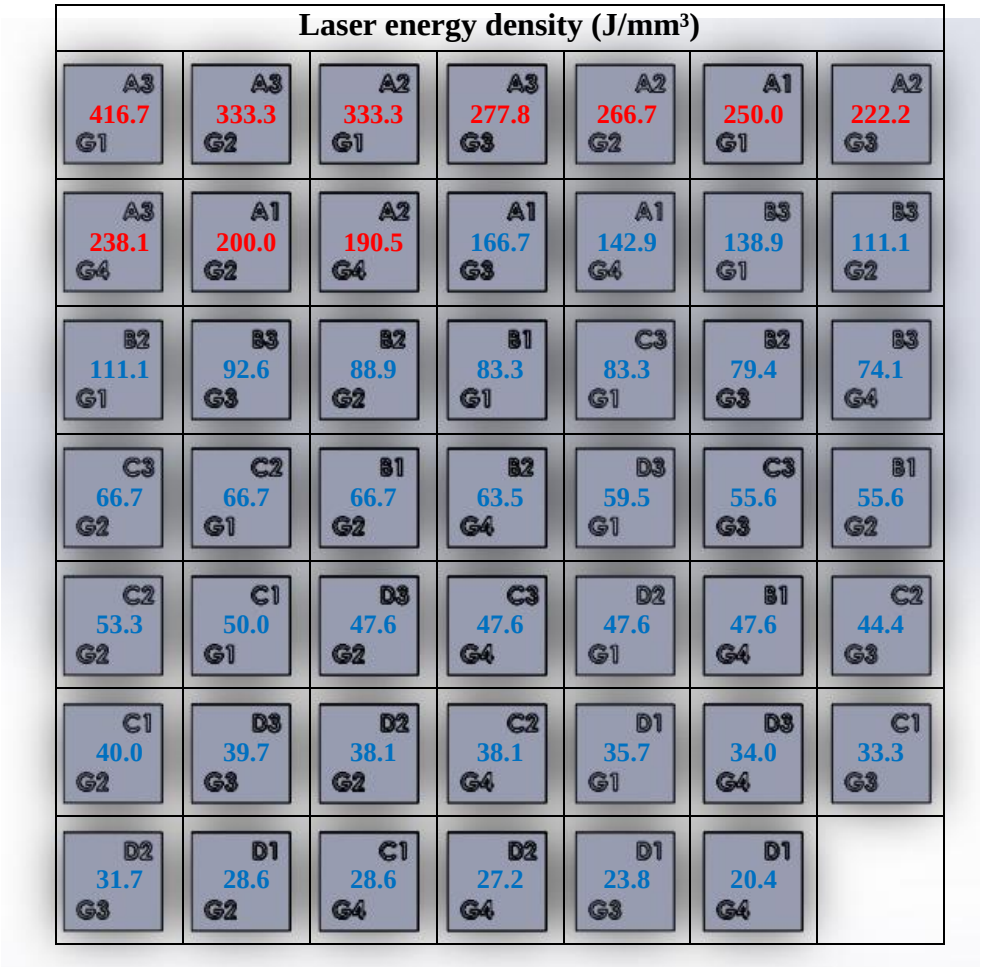

Figure 5.2. Laser energy density of each sample and layout.

5.3 Manufacturing Process

The computer-aided design model presented in the last section contained the assembled 48 samples, with identification marks and minimum distance between samples (6 mm) already defined. The model was then imported into a software called Magics to create the slices necessary for the machine to define each cross-section to be laser scanned. Afterwards, the sliced model was again imported into the EOS machine software, which was then used to define each one of the individual parameters of the samples, as well as the substrate temperature and layer thickness. Finally, the code was generated and sent to the EOS machine to commence the process. At the same time, the machine was loaded with the correct amount of powder and the inert gas was connected to the machine.

The manufacturing process to build the batch of samples took a continuous 48 h to finish; however, as can be observed in Figure 5.3c, 10 samples were not completed. The main reason for the failure was the extreme interference between these 10 samples and the powder roller, resulting in collision between them. The referenced samples were excluded from the batch in the first hour of the printing operation, since this interference could have resulted in imminent damage to the ceramic roller, a very fragile component of the machine. Note the inert gas duct in the top of the chamber (Figure 5.3b), which is responsible for gas flow from the top to the bottom of the powder bed. The high laser energy density samples were placed closer to the gas flow to maximize the cooling rate on them.

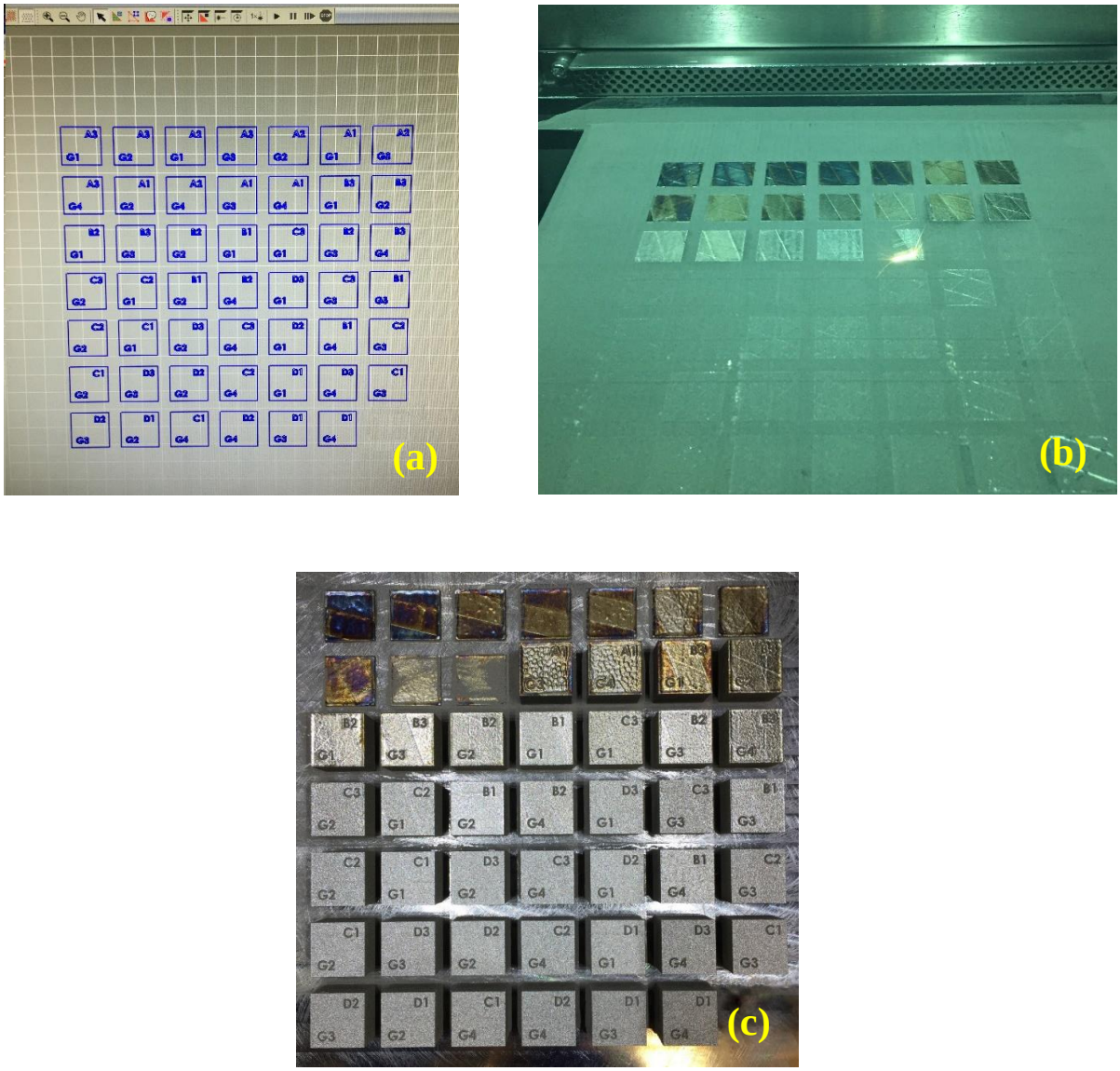

Figure 5.3. Set of samples being programmed using EOS 3D printing system (a), the printing process taking place with the laser scanning at the centre (b), and the finished direct metal laser sintering samples on the substrate.

The root cause of the printing failure of these samples is related to the fact that these samples have high laser energy density, ranging from 416 to 190 J/mm^3. Thus, on each layer the molten material accumulates on the border due to heat and mass transport, resulting in a thick solidified

"bumper" on all four edges of the samples, as indicated in Figure 5.4c. The failed printed samples could not be used for the analysis, given the small height and the impossibility of removing them from the substrate plate. Figure 5.4b shows six of the samples, with some of them presenting a very dark blue colour, while others have a golden surface. As with welding, these colours are the result of an oxide layer that forms on the surface after solidification, affecting the final corrosion resistance of the sample [82].

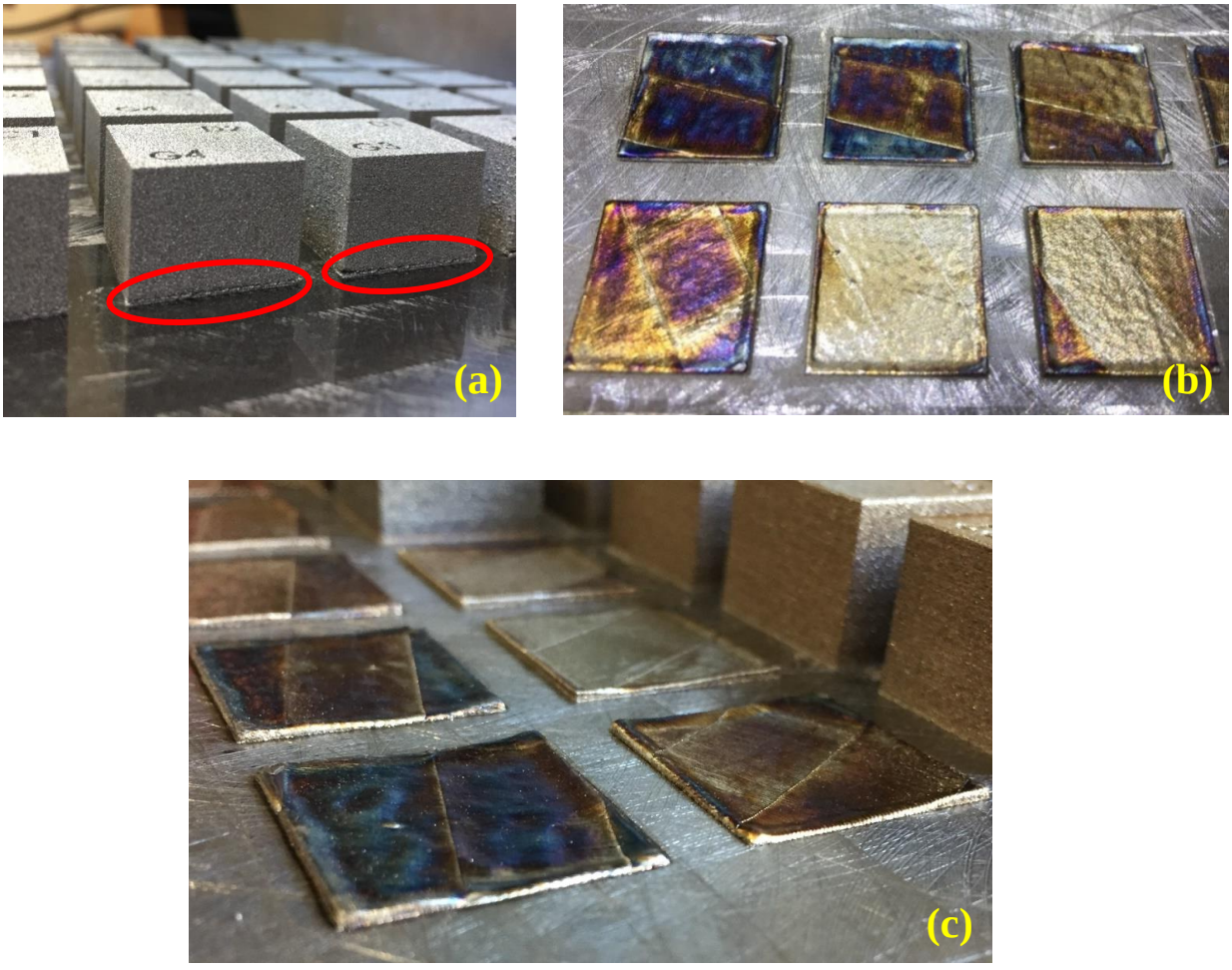

Figure 5.4. Low energy density samples (a), high energy density samples (b), and "bumper" detail on the high energy density samples (c).

On the other hand, for the low energy density samples, we found that a small delamination process occurred in the last sample row, especially on samples G4D2, G3D1, and G4D1. This delamination is an indication that the combination of parameters was not sufficient to properly bond the layers in those samples, although it was still not a severe delamination and we were able to remove and characterize the samples. Figure 5.4a depicts the phenomenon.

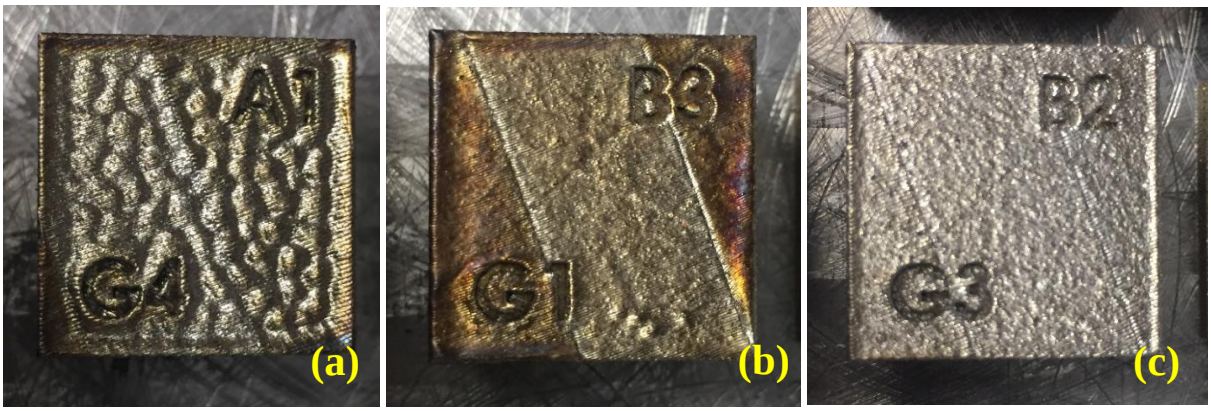

Figure 5.5. High laser energy density sample with surface deformation and oxide layer on samples G4A1 (a) and G1B3 (b); normal surface printed sample G3B2 with lower laser energy density (c).

The highest laser energy density samples (G3B1, G4A1, and G1B3) in the second row of samples still had noticeable surface deformations and an oxide layer. Figure 5.5a shows several surface deformations in the form of small “bumpers” on sample G4B1, and Figure 5.5b shows a sample with a golden oxide layer. The sample in Figure 5.5c, on the other hand, has a metallic appearance to its surface, indicating that mass transport did not influence the sample.

5.4 Density Analysis

The samples were analyzed according to Archimedes’ principle density measurement, which is suitable for metal 3D-printed materials and more accurate than conventional displacement

methods [83]. The method is described by "ASTM B962-17 Standard Test Methods for Density of Compacted or Sintered Powder Metallurgy (PM) Products Using Archimedes' Principle," in which each sample is weighed twice using a Mettler Toledo scale (Figure 5.6) [84]. First, we measured the sample in the air (M_1). Next, we immersed the sample in distilled water and measured the apparent mass (M_2). Next, the density was calculated as follow:

$$\rho_{sample} = \frac{M_1}{M_1 - M_2} \rho_{water} \tag{5.1}$$

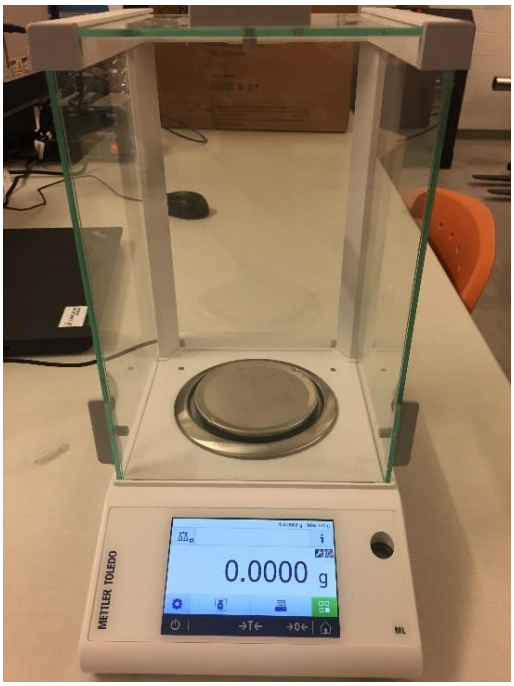

Figure 5.6. Scale used to measure the mass of the samples and consequently their densities.

where ρ_{sample} is the final density of the sample and ρ_{water} is the density of distilled water at 25 °C (0.997 g/cm³). The scale has a resolution of ±0.0001 g. The samples were weighed twice and the results averaged for ρ_{sample}. The bulk density of SS-316L is 8.05 g/cm^3 (ρ_{bulk}), a value used as a reference to calculate the relative density (ρ_r) of the samples as follows:

$$\rho_r = \frac{\rho_{sample}}{\rho_{bulk}}(\%) \tag{5.2}$$

The porosity of the samples was acquired by using an imaging method to calculate the area fraction of the voids. ImageJ software was used for the analysis.

5.4.1 Results of relative density and porosity analysis

The results of the relative density measurements are show in Figure 5.7. The data were compiled according to the laser energy density, *E*v, of each sample. Notice the shape of the fitted curve (R^2 = 0.9702), with samples with low laser energy density having the lowest relative density (ρ_r); however, after achieving a maximum value, ρ_r begins to decrease.

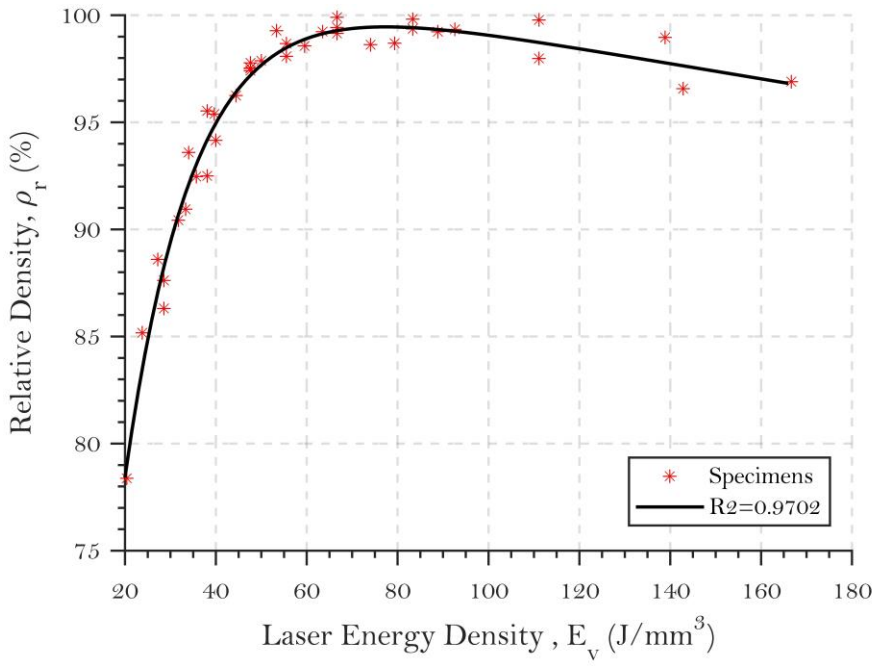

Figure 5.7. Relative density of the samples versus the laser energy density.

By analyzing the effects of each group separately, we compiled three different groups and their corresponding samples, as seen in Figures 5.8, 5.9, and 5.10.

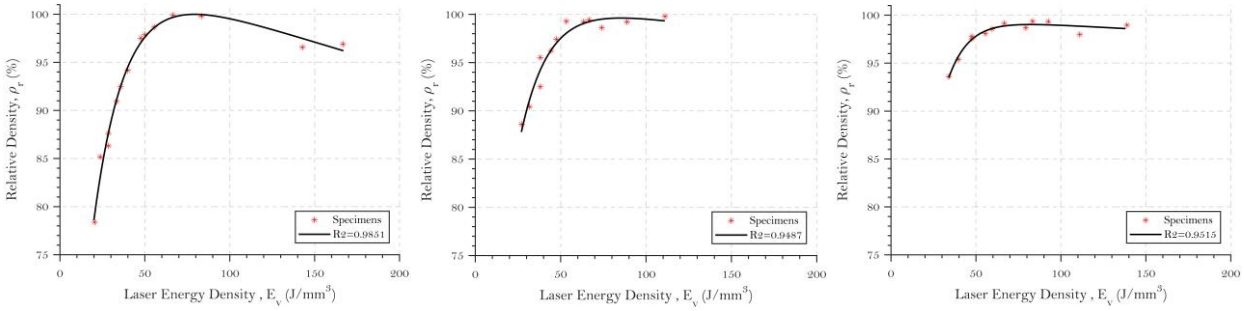

(a) **(b)** **(c)**

Figure 5.8. Relative density of the samples varied according to laser energy density. Samples were grouped according to power input, with groups designated as 1 (P = 150 W) (a), 2 (P = 200 W) (b), and 3 (P = 250 W) (c).

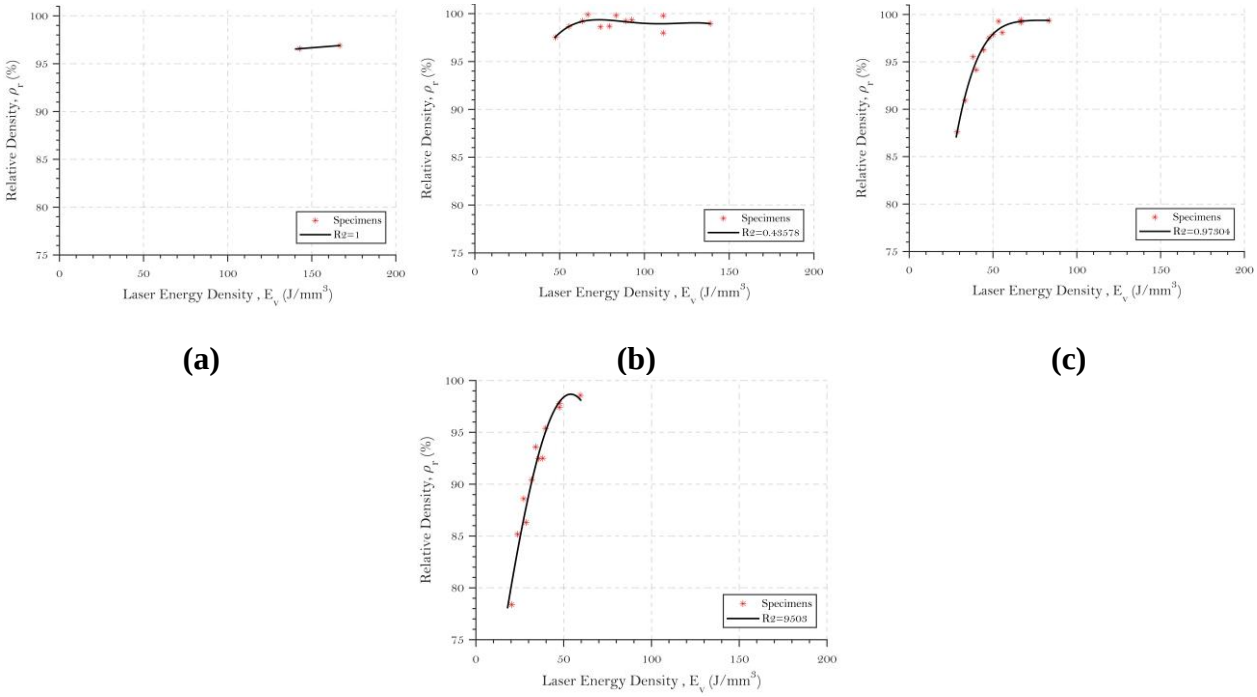

(a) **(b)** **(c)**

(d)

Figure 5.9. Relative density of the samples varied according to laser energy density. Samples were grouped according to scanning speed, with groups designated as A (v = 250 mm/s) (a), B (v = 750 mm/s) (b), C (v = 1250 mm/s) (c), and D (v = 1750 mm/s) (d).

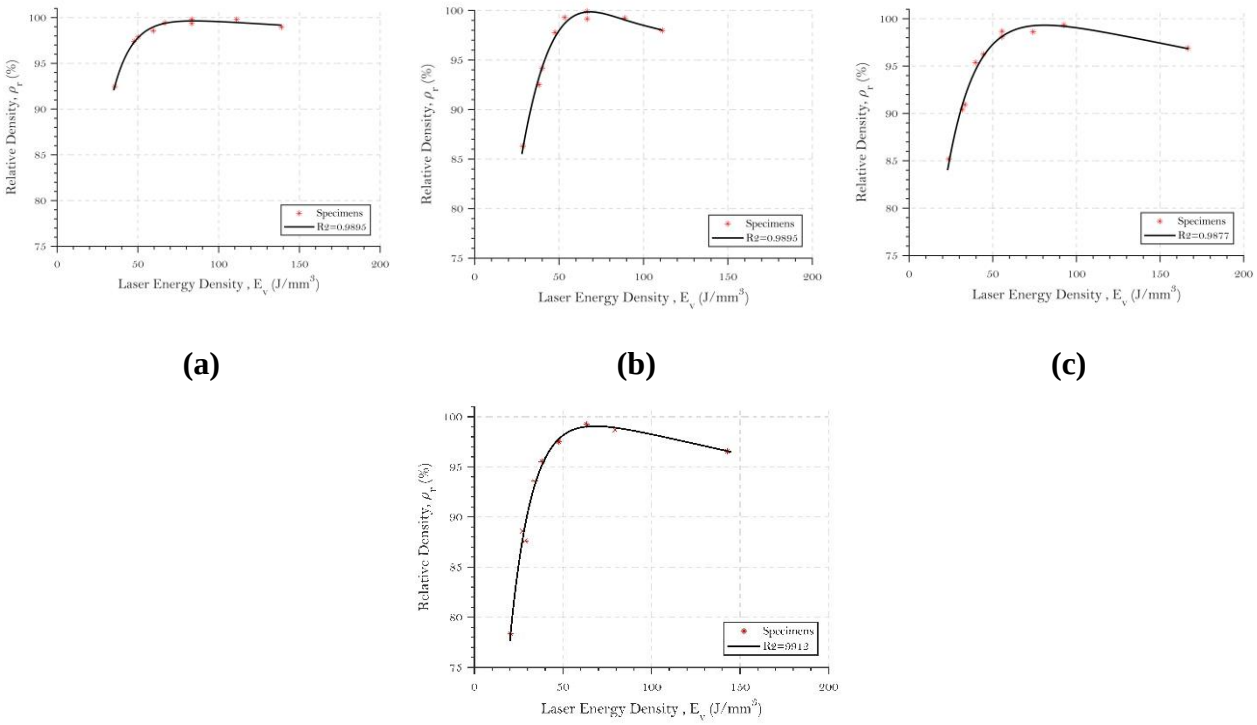

(a) **(b)** **(c)**

(d)

Figure 5.10. Relative density of the samples varied according to laser energy density. Samples were grouped according to hatching distance, with groups designated as G1 (s = 80 µm) (a), G2 (s = 100 µm) (b), G3 (s = 120 µm) (c), and G4 (s = 140 µm) (d).

It is evident that some groups of parameters a have larger ρ_r range of samples varying through the E_v values. We can observe this trend in each one of the parameter groups. In Figure 5.8a, for the P = 150 W group, samples have ρ_r varying from 78.4% to 99.5%; in Figure 5.9d for the v = 1750 mm/s group, samples have ρ_r varying from 78.4% to 98%; and in Figure 5.10d, for the s = 140 µm group, samples have ρ_r varying from 78.4% to 99%. On the other hand, groups with a small relative density range can be seen in Figure 5.8c (P = 250 W), Figure 5.9b (v = 750 mm/s), and Figure 5.10c (s = 80 µm), with 94%–99%, 97%–99.5%, and 93%–99.5% relative density, respectively. A small range in relative density within each group means that the combination of

other parameters did not influence the final density values. Thus, these conditions represent the optimal values to be used in the process. However, relative density alone does not represent all the ideal mechanical properties of a material, and further analysis needed to be carried out.

For the group with v = 250 mm/s (Figure 5.9a), only two samples were printed, and therefore the analysis was not valid for this parameter, given the lack of samples available to analyze the material's tendencies. Figure 5.11 shows the groups individually assessed for better understanding of the trends.

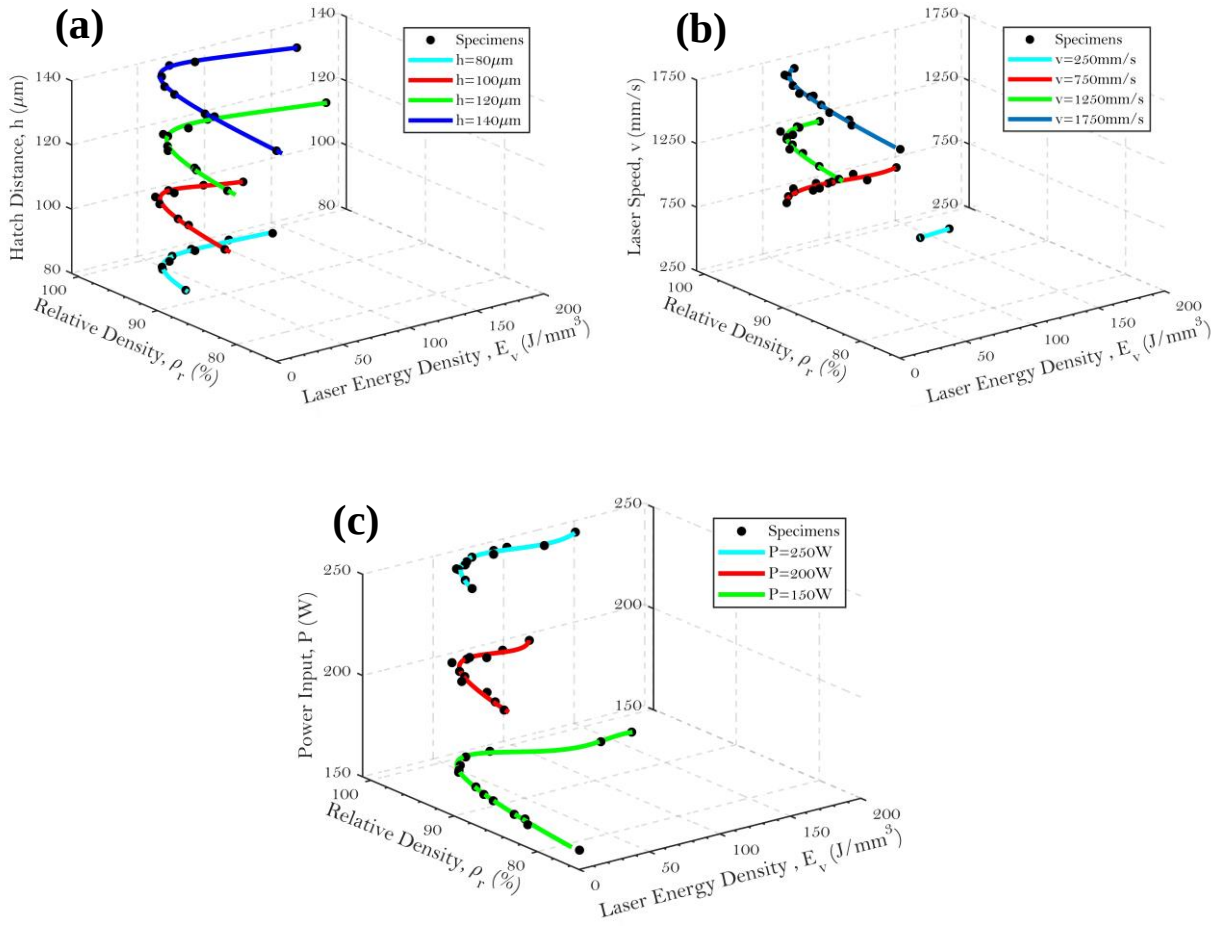

Figure 5.11. Relative density versus laser energy density for hatch distance (a), scanning speed (b), and power input (c).

The maximum relative density value achieved among all samples was 99.57%, for sample G1B1, and the minimum relative density value was 78.389%, for sample G4D1. Figure 5.12 depicts the top surface micrograph (scanning direction) of the samples mentioned. Note the number of voids in the sample with low relative density compared to the one with high relative density.

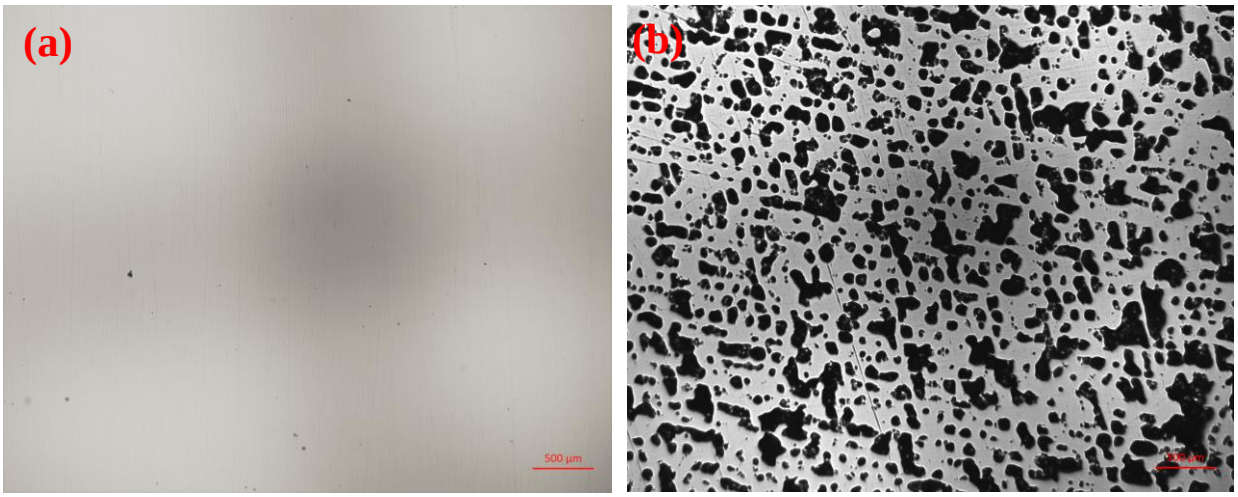

Figure 5.12. Micrographs of the top surface after polishing samples G1B1 (a) and G4D1 (b).

The porosity (φ_{final}) of the samples was measured using ImageJ imaging software. The top surface of the samples was sanded and polished with a 0.05 µm diamond suspension, and later images of the surfaces were acquired by optical microscopy. The micrographs were then processed by ImageJ software, using the area fraction of the voids to calculate the percentage of porosity of the sample. Figure 5.13 shows the results, with a maximum porosity of 41.66% achieved for sample G4D1 and minimum porosity of 0.045% for sample G3B3.

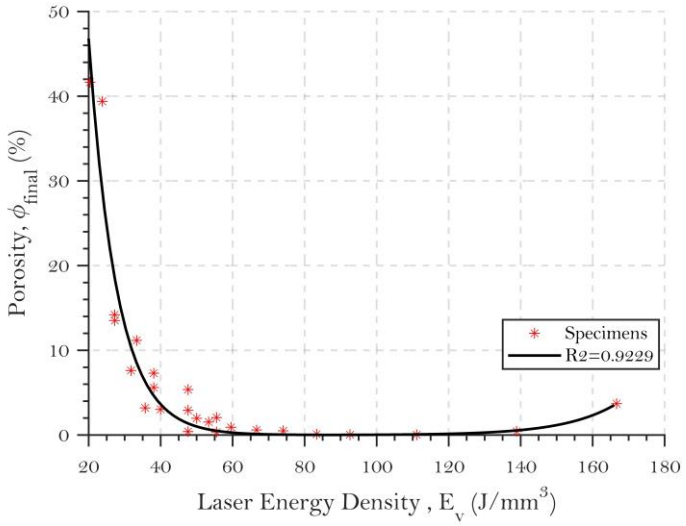

Figure 5.13. Porosity versus laser energy density of the samples.

Note that the curve follows the same trend as the relative density results previously presented. The highest laser energy density sample, G3A1 (166.67 J/mm^3), has 3.71% porosity, considerably more than sample G1B1 (83.33 J/mm^3), which had a porosity of 0.107%.

5.5 Surface Micrographs

The as-built top surface images were also acquired for different groups to show the behavior of the layer and their respective scanned tracks along the surface. The micrographs are shown at a magnification of 2.5× and 10× in the selected area. It is clear that the high porosity observed in sample G4D1 (Figure 5.12b), which gave the part a low relative density, is strongly associated with poor or partially melted powder, as seen in Figure 5.14. On the contrary, the high-density samples have a large number of small particles throughout the surface, as seen in Figure 5.13, the result of particles being ejected due to high laser energy density.

Magnification of 2.5x

Magnification of 10x

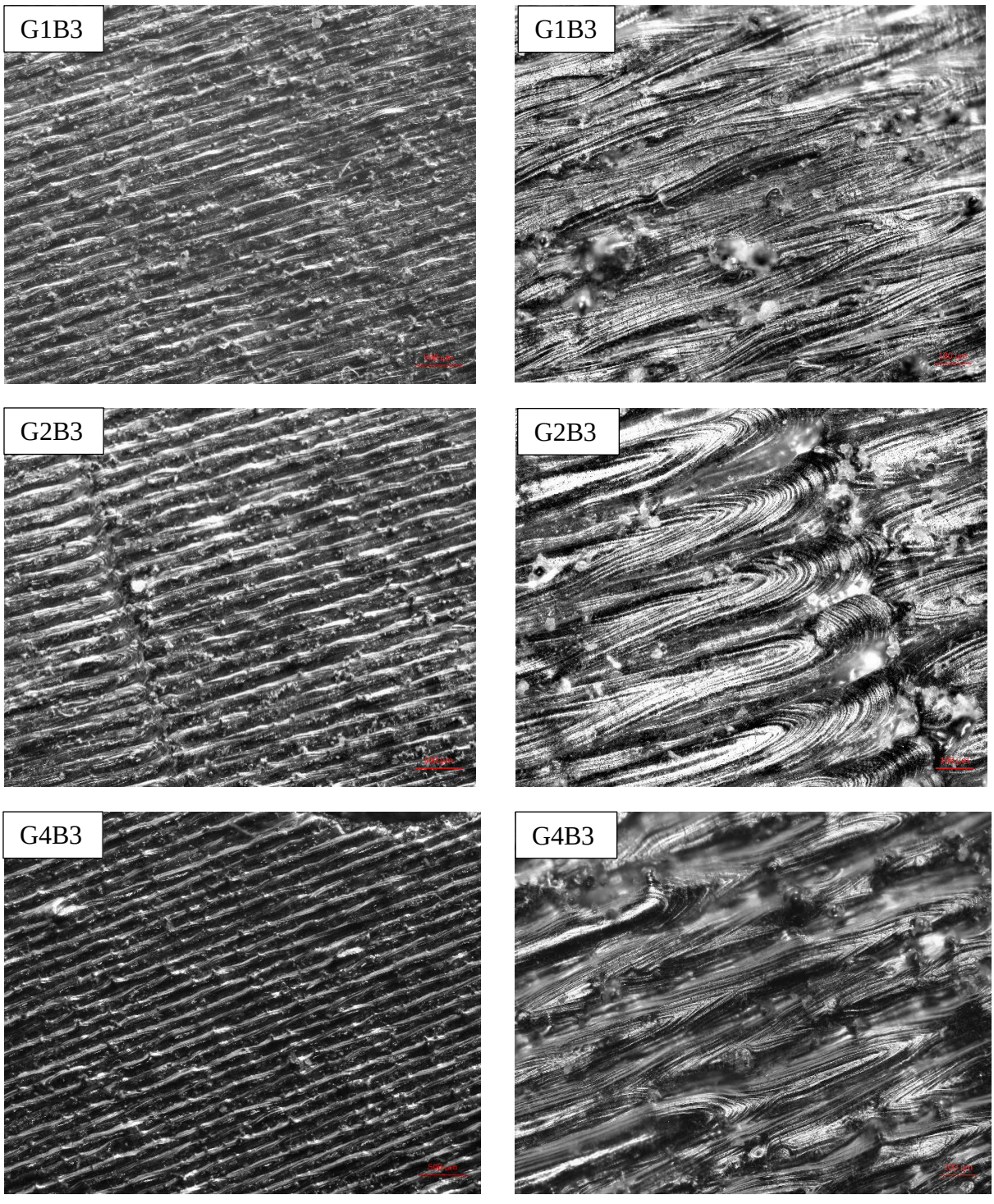

Figure 5.14. As-built micrographs of the top surface with same scanning speed (750 mm/s) and power input (250 W), varying the hatch distance from 80 to 140 µm.

Magnification of 2.5x

Magnification of 10x

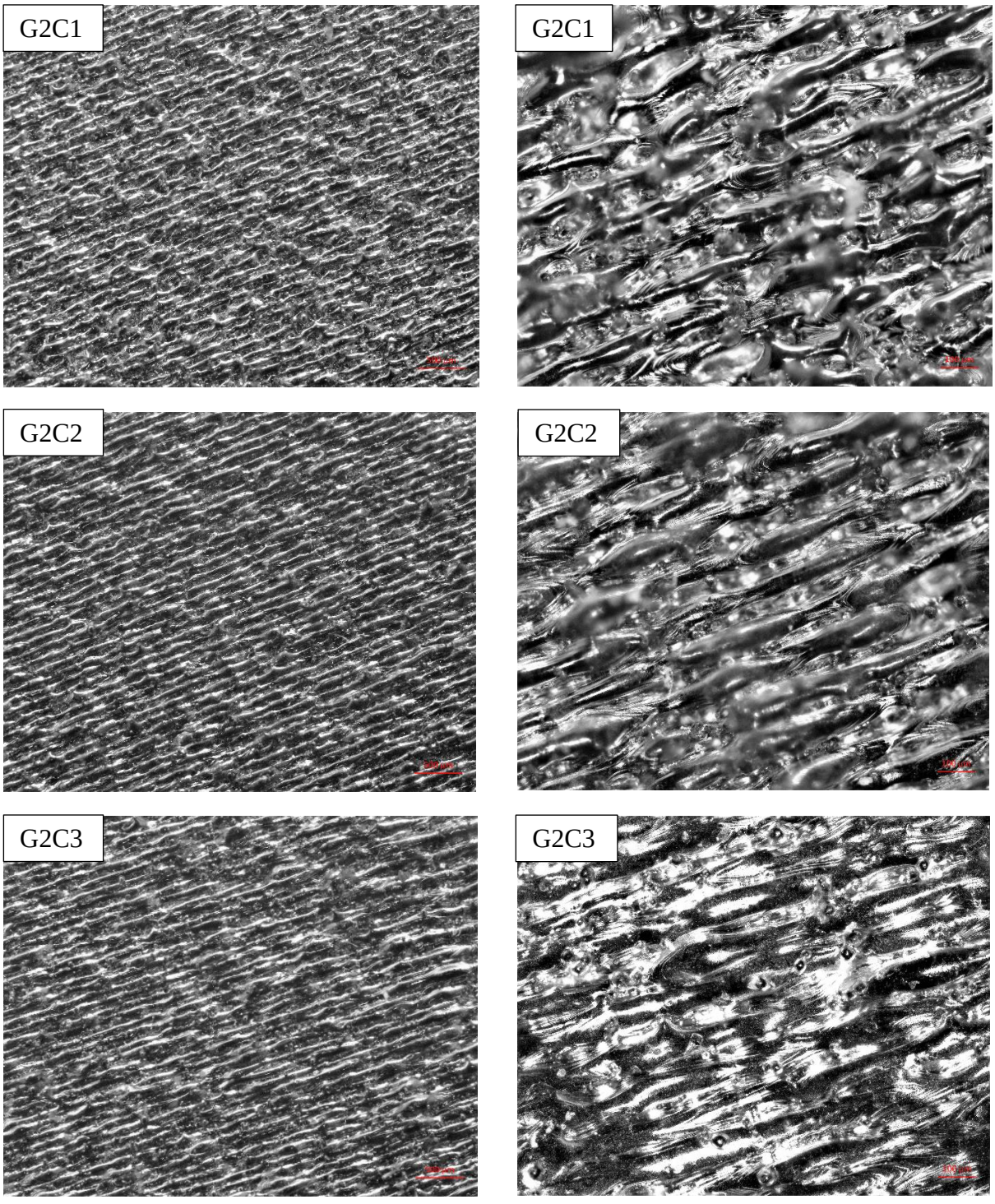

Figure 5.15. As-built micrographs of the top surface with same scanning speed (1250 mm/s) and hatch distance (100 µm), varying the power input from 150 to 250 W.

Magnification of 2.5x

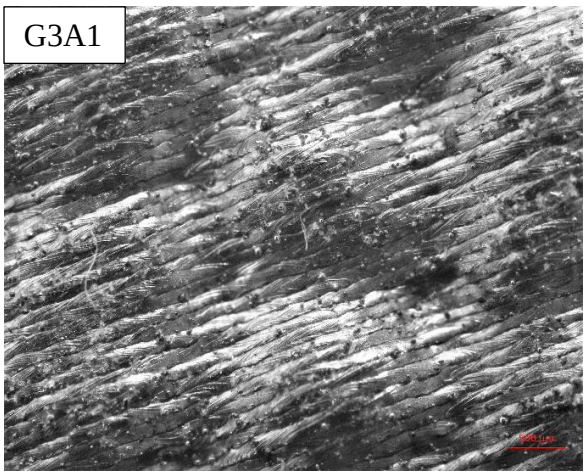

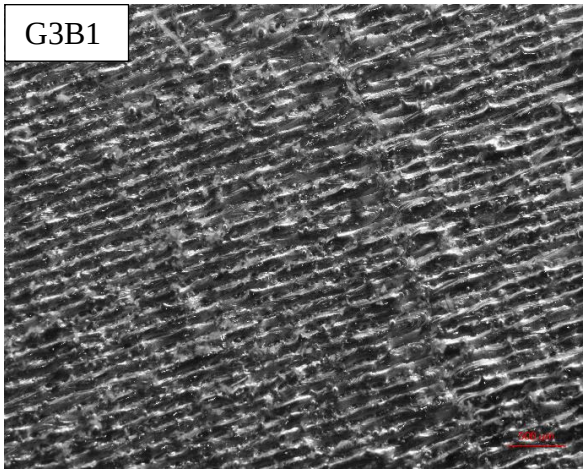

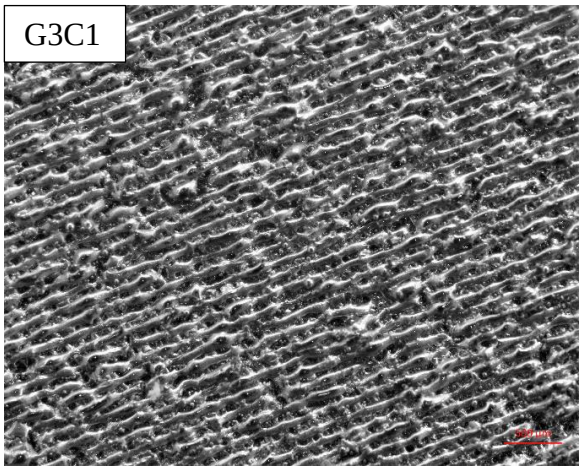

Magnification of 10x

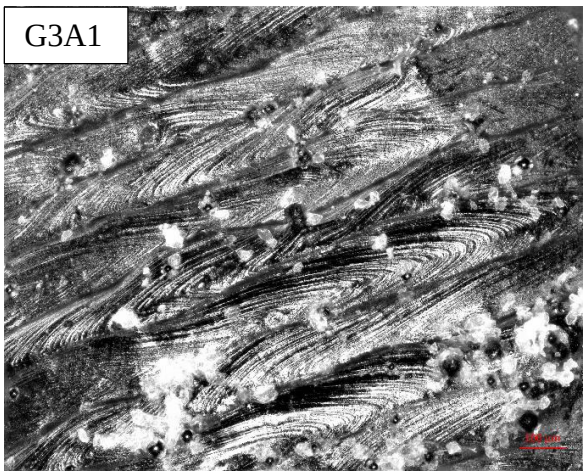

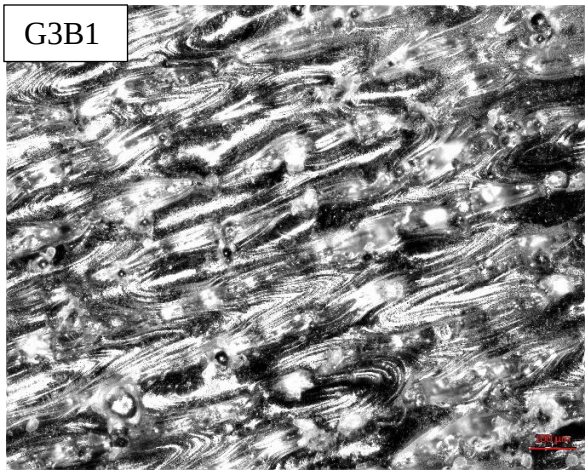

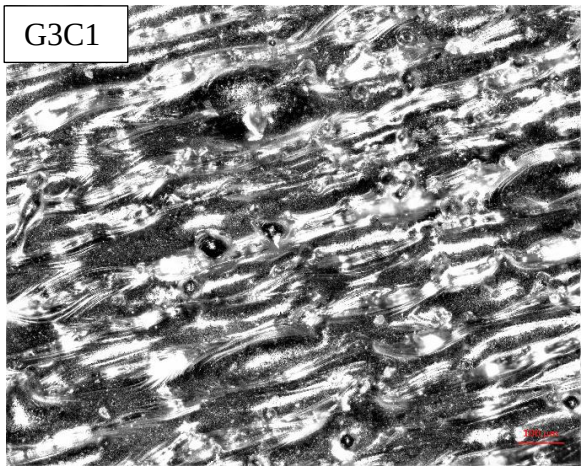

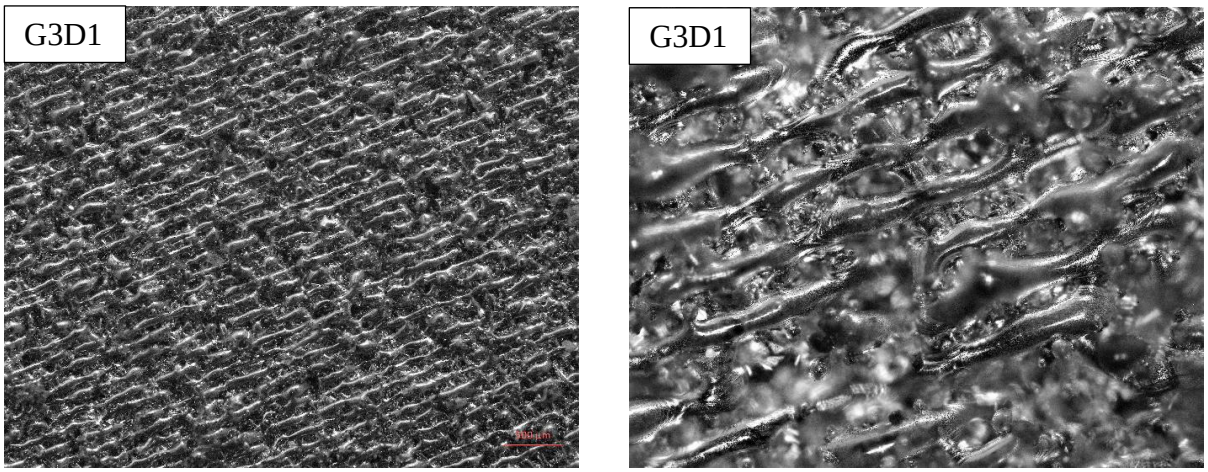

Figure 5.16. As-built micrographs of the top surface with same power input (150 W) and hatch distance (120 µm), varying the scanning speed from 250 to 1750 mm/s.

Magnification of 2.5x Magnification of 10x

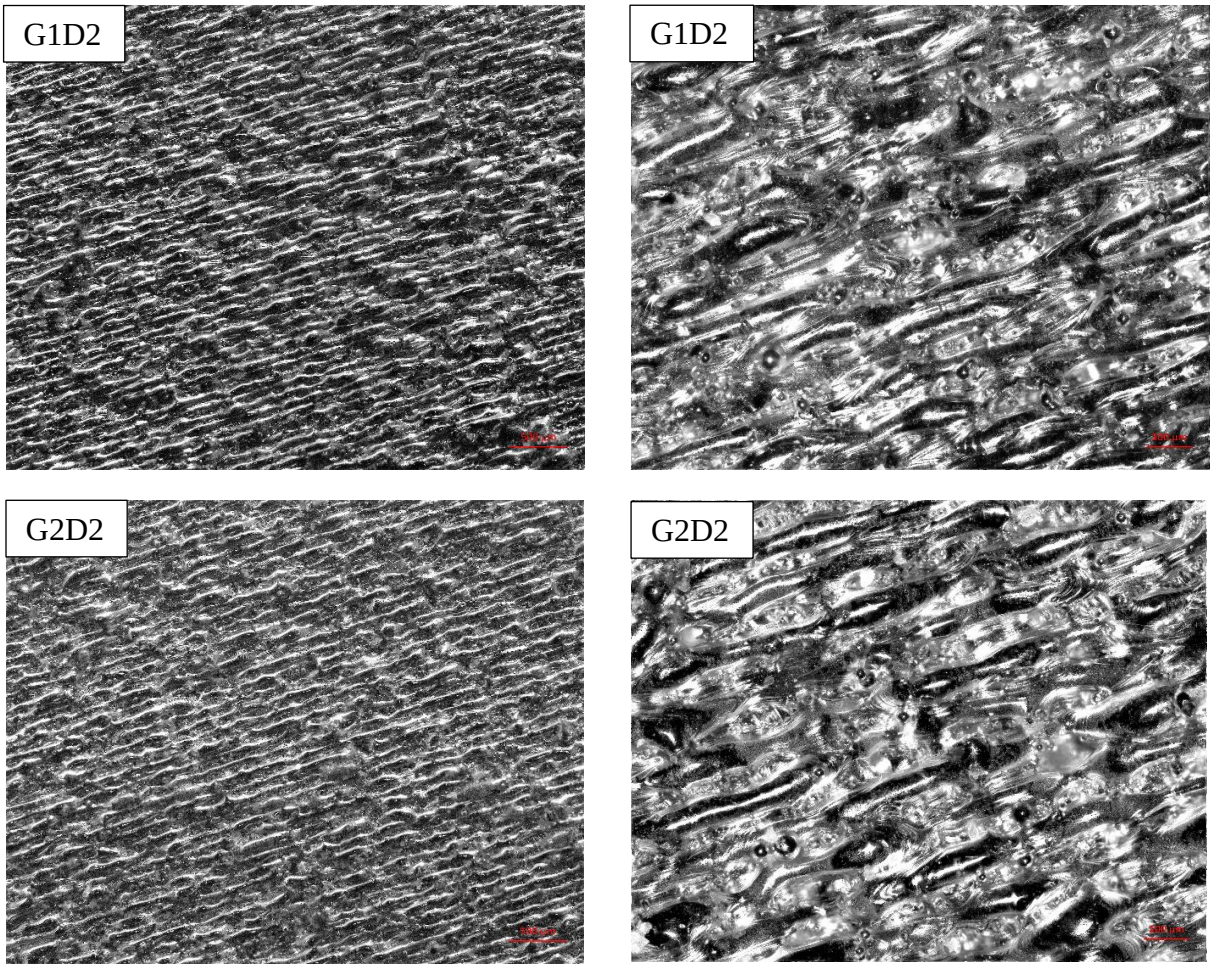

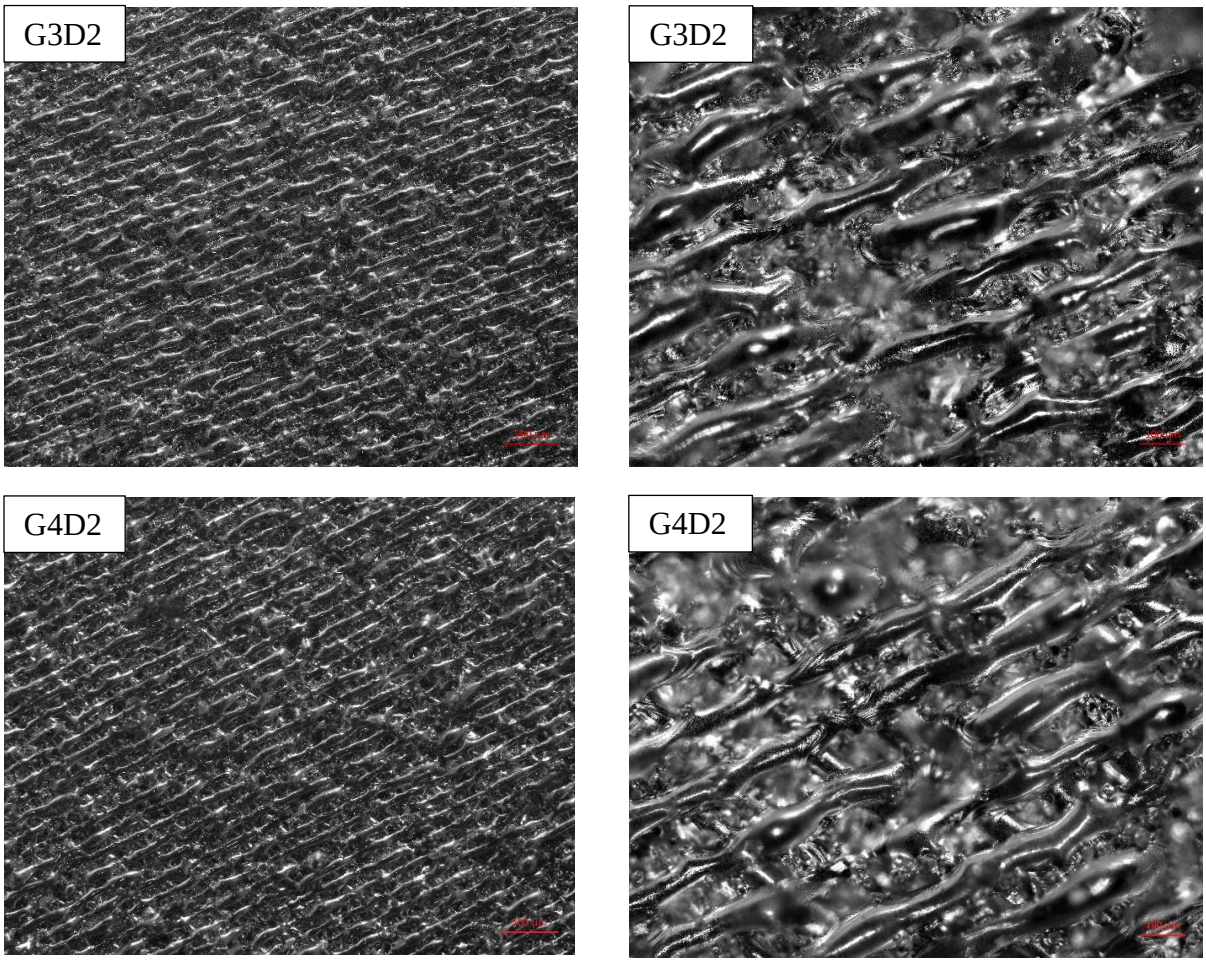

Figure 5.17. As-built micrographs of the top surface with same power input (200 W) and scanning speed (1750 mm/s), varying the hatch distance from 80 to 140 µm.

The poor or partially melted tracks in several micrographs are the main cause of the high porosity and low relative density of the samples. The combination of parameters was responsible for this result — samples G1B1, G3B1, G3D2, and G4D2 had the lowest relative densities, mainly owing to low power input, high scanning speed, and high hatching distance.

Figure 5.14 shows three of the highest density samples: G1B3 (98.964%), G2B3, (97.983%), and G4B3 (98.696%). The relative density values achieved for these samples are very similar to each other, and thus variability in the hatch distance did not influence the results, given that the

samples in this group had P = 250 W and v = 750 mm/s. Figure 5.15 has an interesting scenario, with samples G2C1 (94.161%), G2C2 (99.286%), and G2C3 (99.153%). The power input variance in these samples showed an effect on the relative density, with the sample at P = 150 W (G2C1) having the lowest density, and the samples with a power input of 200 and 250 W having very good densities. This group of samples had a fixed hatch distance of 100 µm and a scanning speed of 1250 mm/s.

Figure 5.16 shows the best case involving low and high density in the same group, for samples G3A1 (96.904%), G3B1 (98.674%), G3C1 (90.943%), and G3D1 (85.177%). In this group, the scanning speed was variable enough to have samples below and above the optimal relative density value. G3A1 has high number of ejected particles in the surface, whereas sample G3B1 has the highest relative density value in the group and displays a fully consolidated surface appearance with only a few partially melted tracks. G3C1 and G3D1 have the highest speeds (1250 and 1750 mm/s, respectively) and presented poor or partially melted tracks, as can be seen in Figure 5.17. Finally, in Figure 5.17, while varying hatch distance and maintaining v = 1750 mm/s and P = 200 W, we conclude with samples G1D2 (97.413%), G2D2 (92.501%), G3D2 (90.434%), and G4D2 (88.598%). The relative density in this group decreased substantially as hatch distance increased.

5.6 Residual Stress Analysis

Residual stresses are measured in samples using the X-ray diffraction method. In this method, the strain in the crystal lattice is obtained and linked with the residual stresses by applying the predetermined constants of the material used. The incident X-rays in the surface are captured by the grains and crystals, thus influencing the final residual stresses found. Some of the X-rays can in fact penetrate the surface, and hence the measurements are an average of strains acting over a

depth of a few microns. The average strains are later converted to residual stresses using the constants of the material [85]. The constants used in this work were extracted from Yakout et al. [48] and applied to all SS-316L samples. Figure 5.18 shows the location of the strain extraction, on the side of the samples (building direction), to avoid the influence of the scanning direction on the measurements.

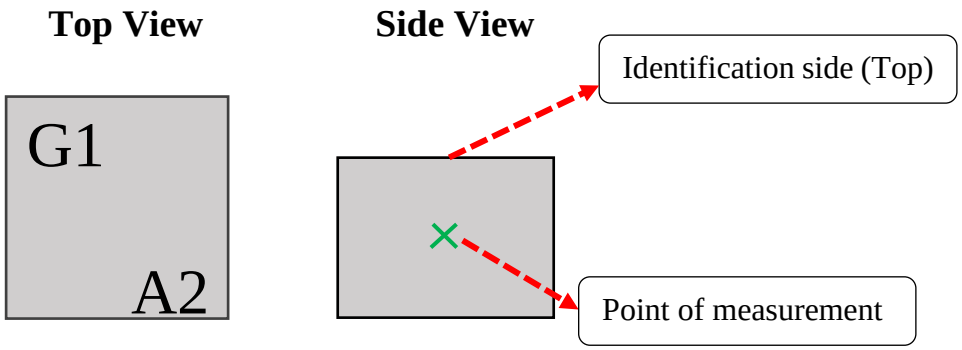

Figure 5.18. Measurement location of residual stresses in a sample.

5.6.1 Results for residual stress analysis

The principal stresses σ_1 and σ_2 were obtained for this analysis, since only one point of X-ray diffraction was obtained in the surface and we were not analyzing the stress directions. Amongst the samples analyzed, there was a large variation of residual stresses, between 40 and 84 J/mm^3, with the maximum principal stresses going from compressive to tension states. From 84 to 140 J/mm^3, we observed a tendency of the residual stresses to rise; however, at 166 J/mm^3 (sample G3A1), the residual stress decrease. Figure 5.19 depicts the behavior of the residual stress versus the laser energy density of the samples.

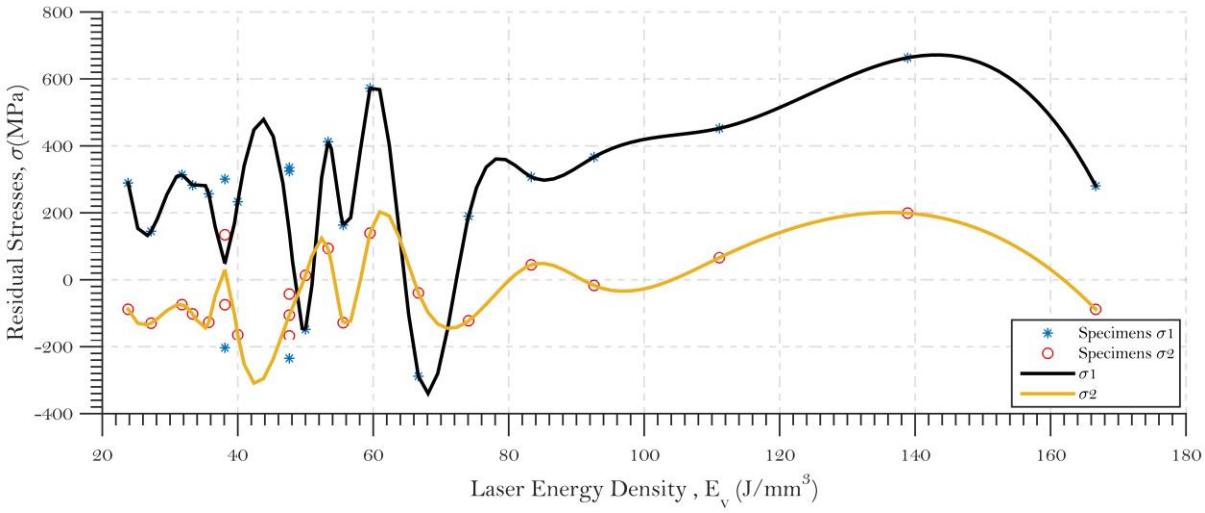

Figure 5.19. Residual stresses measured at the side of the sample's surface versus laser energy density.

Note that residual stresses vary erratically, both for maximum and minimum values in the previously mentioned range. The reason behind this behavior is the intrinsic uncertainty of the X-ray diffraction method associated with the material constants used to convert the phases into strain values, since the 3D-printed part can have slightly different material composition from the material used for the conversion. Figure 5.20 to 5.22 show the results for individual parameter sets.

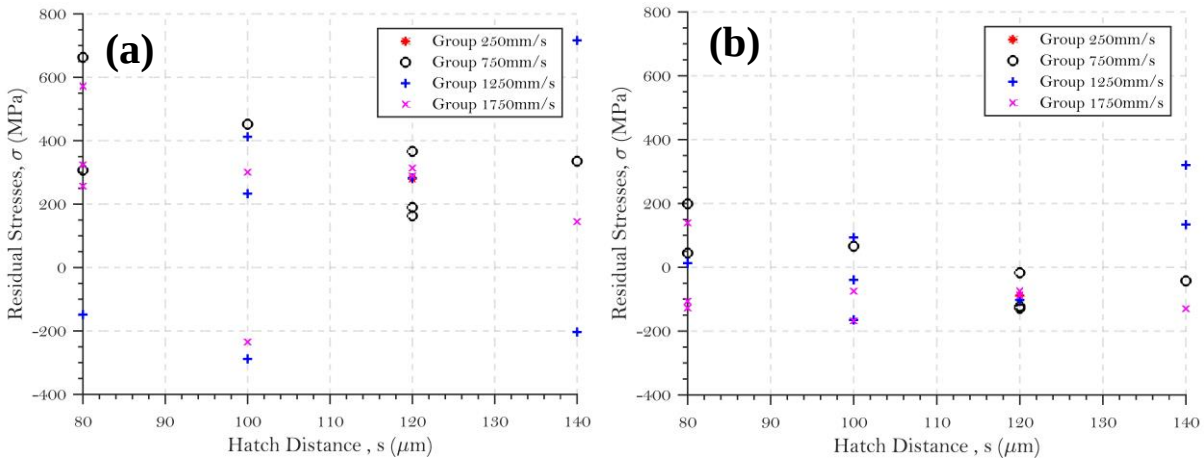

Figure 5.20. Residual stress measurements for scanning speed groups versus hatch distance. Maximum principal stresses (a) and minimum principal stresses (b).

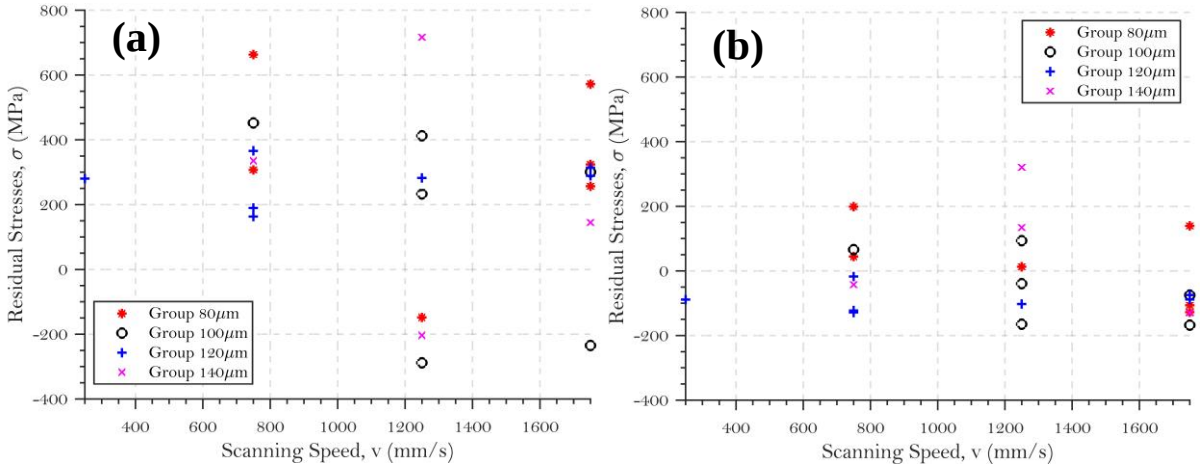

Figure 5.21. Residual stress measurements for hatch distance groups versus scanning speed. Maximum principal stresses (a) and minimum principal stresses (b).

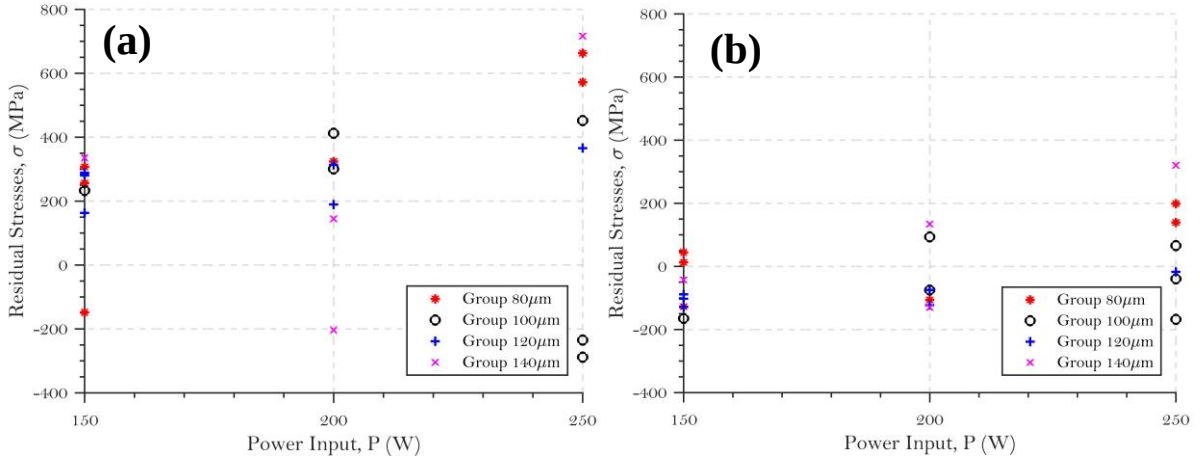

Figure 5.22. Residual stress measurements for hatch distance groups versus power input. Maximum principal stresses (a) and minimum principal stresses (b).

The scanning speed group sorted by its respective hatch distances (from 80 to 140 μm) brought dispersed results for the subsequent residual stress values (Figure 5.20). No trend was found for the maximum principal residual stresses in Figure 5.20a. For the minimum principal residual stresses,

there was a slight trend from 80 to 120 µm, with the σ_2 decreasing, but at 140 µm it dispersed again, as seen in Figure 5.20b.

The same applies to the results presented in Figure 5.21, where samples are sorted according to the scanning speed and hatch distance grouping. In Figure 5.21b, the same behavior occurs, as was observed in the hatch distance group, but the trend is very weak. From 750 to 1750 mm/s, the minimum principal residual stresses decrease.

Power input sorting, however, yielded a trend that is noticeable for both maximum and minimum residual stresses values, as seen in Figure 5.22. It is clear that at 150 W, there is an overall lower stress value than at 200 or 250 W. The trend is more perceptible in Figure 5.22a, with the maximum residual stresses changing from 350 MPa (maximum achieved) at 150 W, 400 MPa for 200 W, and 716 MPa for 250 W. This is a strong indication that power input is the main parameter responsible for high residual stresses in the built samples. Although all parameters play important individual roles, we can infer that the sensitivity of the power input is vital in the final properties of the built part.

5.7 Microstructural Analysis

A microstructural image was obtained to understand the micro-constituents of the printed samples. SS-316L is an austenitic steel (γ-Fe) with an FCC crystal structure in its solid form; however, since the raw material is a powder, it is impossible to define the microstructure of the PBF process without proper characterization [48]. The samples have a high degree of martensitic formation, especially around the melting pool of the solidified material. The reason is the increased temperature gradients around the melt pool, as evident in chapter 4, as well as rapid solidification

rates across each melt pool, a scenario that is ideal for the martensitic transformation. Figures 5.23 and 5.24 show the micrographs. Note the detail highlighted in Figure 5.23, which shows the martensitic transformation happening at the melt pool boundary.

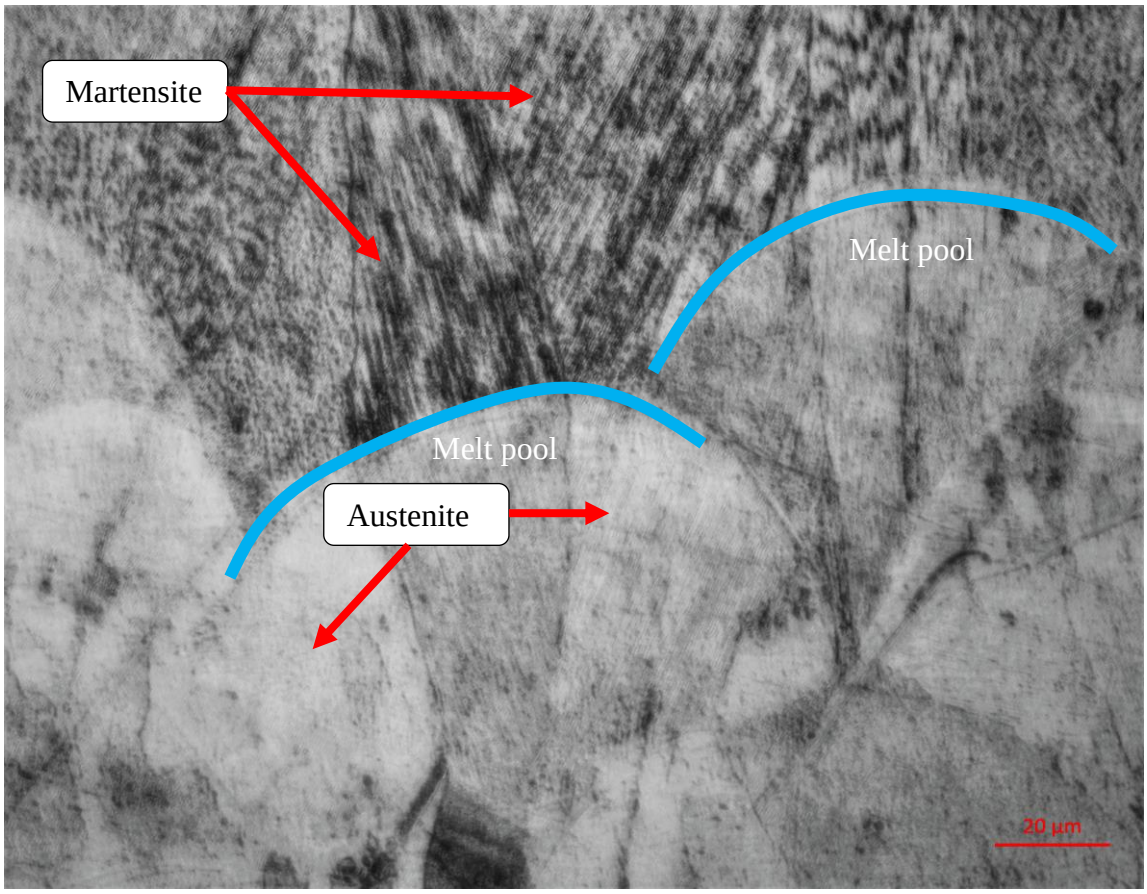

Figure 5.23. Micrograph (magnification 40×) of sample G1B3, with austenite and martensite areas highlighted.

Another important observation is that surface hardening, caused by martensitic transformation, is also responsible for residual stresses. It is not clear what the exact impact of this contribution is; however, volume expansion is taking place when martensite is formed, causing compression at the surface and tensile stresses at the core of the part, as observed by Yakout et al. [48].

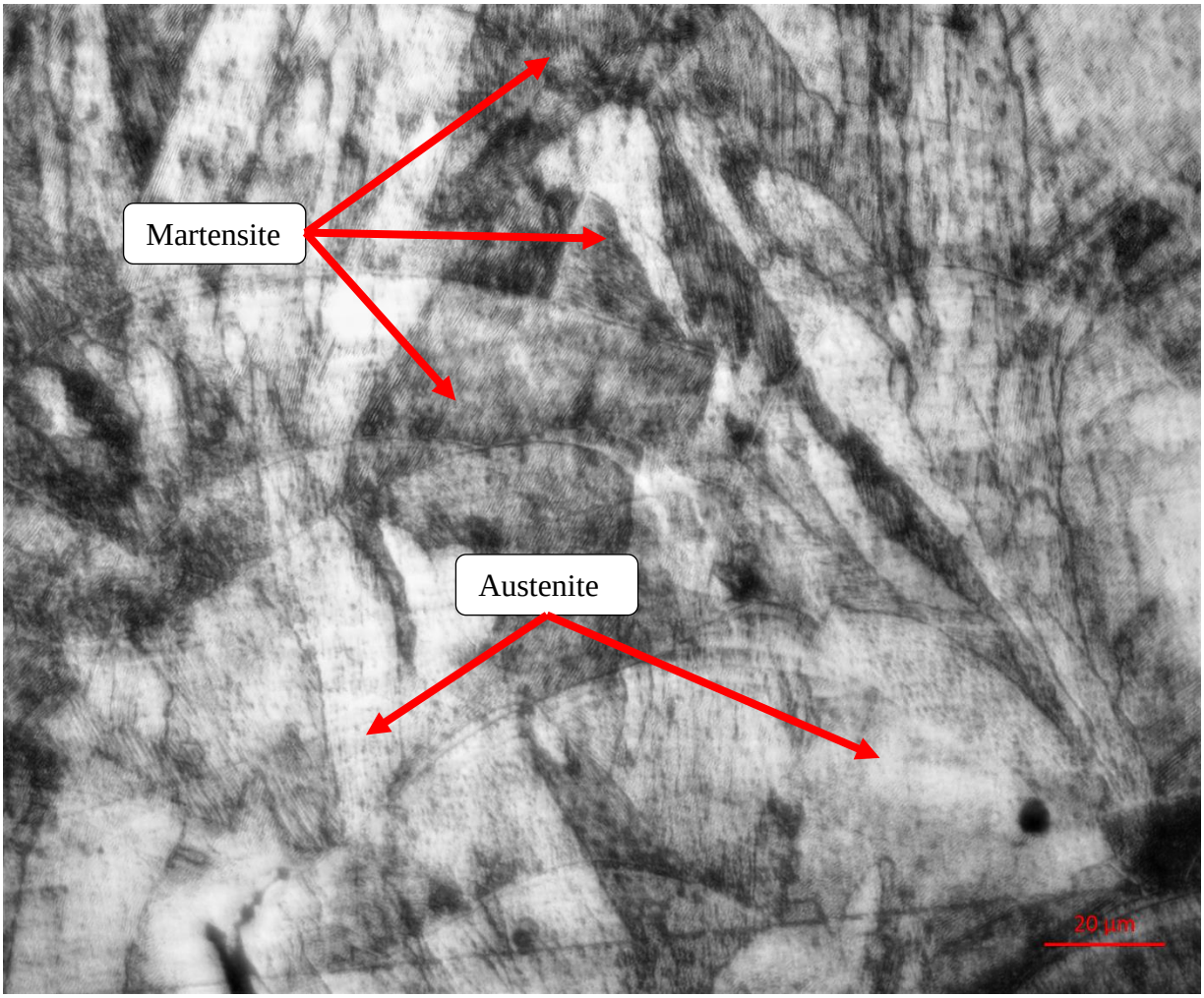

Figure 5.24. Micrograph (magnification 40×) of sample G2C2, with austenite and martensite areas highlighted.

Besides the micro-constituents, we acquired an image of the melt pool from the top and side surfaces. From the top, we can clearly see how the laser tracks are influencing the microstructure, as the grains are growing from the solidification of the laser track melt pool; and from the side we can see the melt pool depth. Figures 5.25 and 5.26 show the top surface of sample G2B3 and the side surface of sample G4B1, respectively.

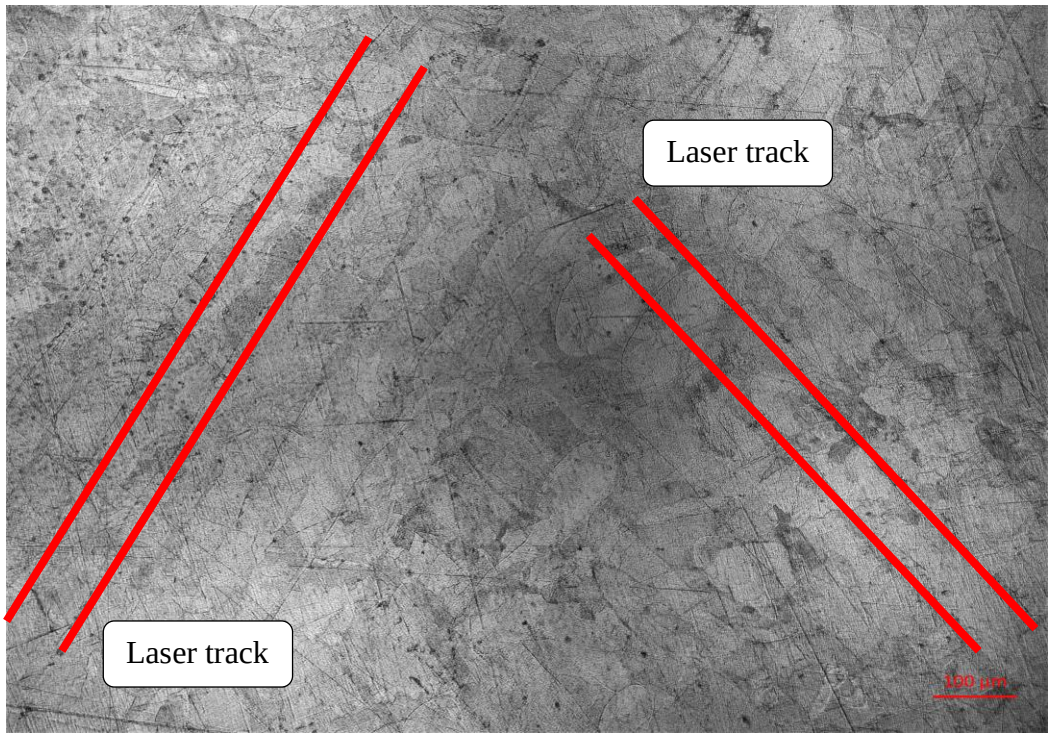

Figure 5.25. Laser track observed at top surface of sample G2B3.

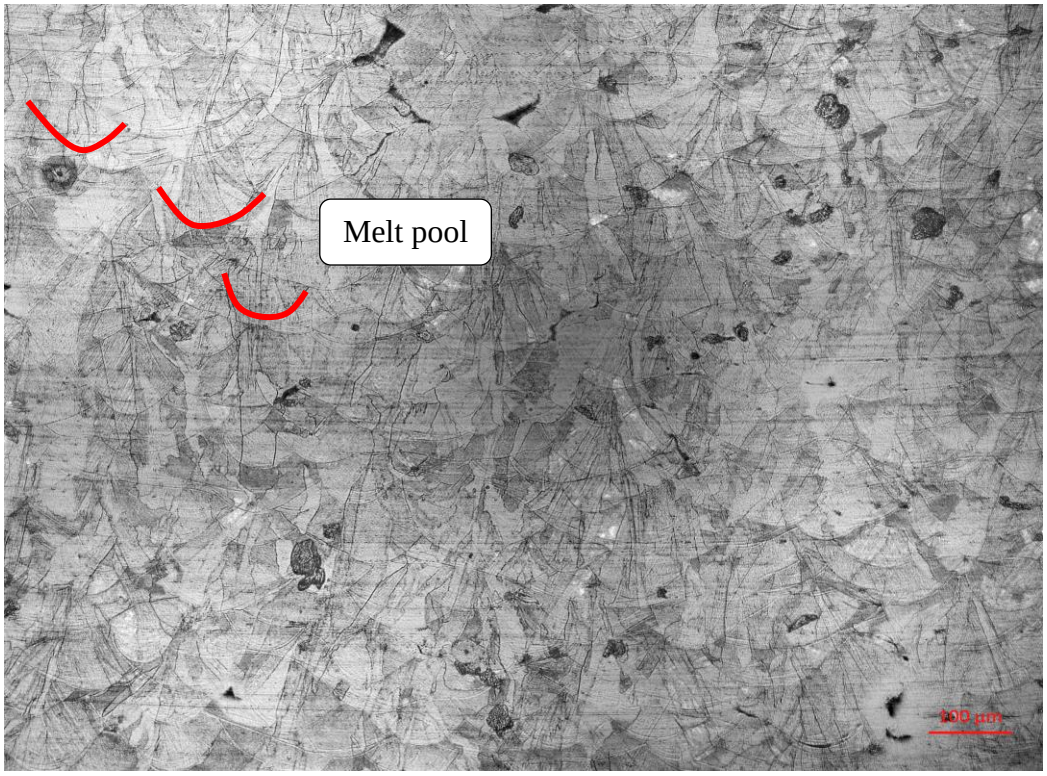

Figure 5.26. Melt pool track observed at side surface of sample G4B1.

5.8 Conclusion and Discussion

From the analysis of the relative density of the samples, we have drawn the following conclusions:

- By increasing the laser energy density, we have found that the final density of the samples tends to increase until a certain maximum value, at which point it starts to decrease, a phenomenon that was observed by Yakout et al. as well [34];
- In the range of 20–65 J/mm^3, the relative density of the samples increased substantially from around 78% to 99%;
- The highest relative density, 99.570%, was found in sample G1B1, which had a laser energy density of ~83.33 J/mm^3; however, we also found similar samples with high density (sample G2B1: 99.517% relative density and 66.667 J/mm^3 laser energy density; sample G1C2: 99.430% relative density and 66.667 J/mm^3 laser energy density);
- At 70–80 J/mm^3 laser energy density, the tendency curve started to have a negative slope, and consequently the relative density decreased; and
- The fitting curve has an exponential algorithm profile with a coefficient of determination (R^2) of 0.9702.

Overall, the behavior of relative density allowed us to confidently evaluate the effectiveness of each parameter in the manufacturing process. Three parameters showed a very small relative density spread among them, and thus a change in other parameters did not significantly alter the density value. Analyzing the parameters separately, P = 250 W, v = 750 mm/s, and s = 80 µm represented the best-case scenario with the lowest range in relative density. Combining all the mentioned parameters gave us sample G1B3, which had a 98.964% relative density. Although it

was not the highest value achieved (sample G1B1 had a relative density of 99.57%), its value was within an acceptable range for relative density. Figure 5.27 shows the relationship between relative density and laser energy density. The drawbacks mentioned are observed in the micrograph of the as-built sample surfaces. The porosity analysis showed that the maximum porosity achieved was for sample G4D1 (41.66% porosity).

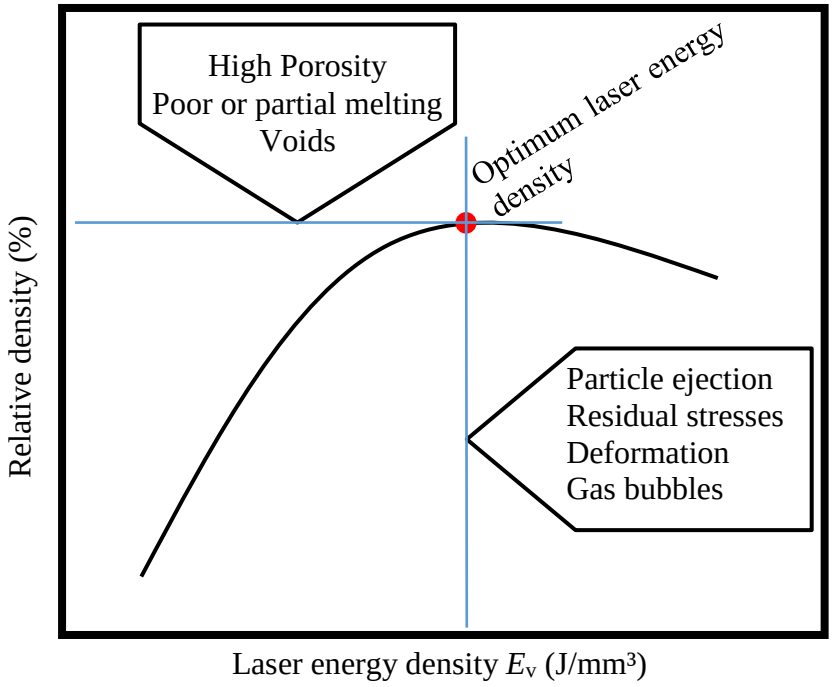

Figure 5.27. The relationship between relative density behavior and laser energy density. Adapted by permission from Springer Nature: *The International Journal of Advanced Manufacturing Technology* [34], Copyright © 2017.

In the residual stress analysis, we encountered some uncertainty; however, we were still able to observe some tendencies, especially when varying the power input, on which principal residual stresses increased in the built part with an increase in power. The residual stresses are the result of high temperature gradients and are caused to some degree by the martensitic formation within the

tracks and layers. The martensite was observed in several samples, especially the high laser energy density ones. For the low energy densities, we could not observe the formation owing to the high porosity present on the surface.

A similar comparison that we can infer between the finite element thermal model and the experimental data is the average melt pool size observed in Figure 5.26. The melt pool was 92 µm when parameters were set at P = 150 W, v = 750 mm/s, and s = 140 µm. Our finite element thermal model using P = 200 W and v = 1000 mm/s had a melt pool of 75 µm. However, the simulation only accounted for 1.5 ms, an infinitesimal time step of the samples' total processing time, which includes solidification, surface hardening, etc.

6 THESIS SUMMARY AND FUTURE WORK

6.1 Thesis Summary and Research Contribution

In this thesis we developed a low-cost thermal FEM capable of capturing the behavior of the temperature distributions, cooling rates, and temperature gradients present during a single layer and track of laser scanning through a powder bed during selective laser melting, a PBF process. In addition, we successfully measured effective powder thermal conductivity for different powder packing densities and diameters to observe the sensitivity of the same in the temperature field, and also studied the melt pool and substrate temperature effects. To emphasize the importance of this type of analysis for the evaluation of process parameters, we built a single batch of samples using DMLS, another PBF process found in the AM industry, to show the effects of the main parameters on the final built part. This parametric analysis is a fundamental tool to investigate the optimal parameters for employment of a new alloy, both for SLM and DMLS.

The main objectives of this thesis are reiterated below:

i. Effective thermal conductivity and emissivity of powders

The thermal conductivity of the powder placed in the bed is different from that of the same material in solid form. To account for that difference, effective thermal conductivity was determined; the impact of the packing density and powder diameter was studied as well. Beyond that, surface emissivity, an important parameter to consider when radiation is involved, was also determined for the powder.

ii. Thermal modeling and sensitivity analysis

Numerical analysis using FEM was conducted to characterize thermal distribution in the powder bed. The main focus was to analyze the behavior of the moving heat source in a single track and the impact of its parameters on the temperature gradient in the powder bed. The material utilized was SS-304L, which has not yet been validated for use in the PBF process. The model was constructed using the main parameters of SLM. The sensitivity in the final temperature distribution in the powder bed to power input, powder packing density, powder diameter, and substrate temperature were analyzed.

iii. Experimental setup, residual stress analysis, verification, and validation

The model was validated by performing residual stress analysis, taking a micrograph of the surface, and analyzing relative density and porosity of SS-316L samples manufactured by DMLS. Residual stresses in the built part result from a high temperature distribution or cooling rate imposed during the manufacturing process. Validation through temperature readings is not feasible given the high speed of the laser and the high temperature induced in the powder bed, leaving the measurement of residual stress as the more reliable parameter for the model. Further validation was conducted by comparing the simulated melt pool shape with values obtained from the experiments.

The results of the SLM analysis performed in Abaqus demonstrate that proper compaction and density distribution of the powder bed is important for keeping the cooling rates and temperature distributions within a desirable range. However, these effects were only perceivable outside the melt pool zone, below the melting point. The powder diameter — although it affected

the value of the effective thermal conductivity, as seen in chapter 3 — did not cause any change in the temperature distribution, and thus the model is not sensitive to changes in powder diameter.

On the other hand, we observed that a power input of 400 W induced very high temperatures at the surface and all the way through the layer thickness. The temperature gradient measured between the top and bottom surfaces was around 1150 K (for T_0 = 643 K), which is the main cause of warping and residual stresses after solidification. A power input of 400 W was enough to cause temperatures to reach 3200 K, at which point vaporization and ejection of metal particles are more common phenomena. The vaporization phenomenon is primarily associated with mass loss, which can bring undesired surface tolerancing due to material loss.

For P = 200 W, the temperature reached the melting point but did not go beyond it, which represents a desirable condition, given the lower temperature gradient achieved (380 K) when the substrate is at 643 K. The melt pool for this power input is ideal, since it does not melt through the entire layer thickness, with the bottom surface staying below the melting point.

Finally, for P = 100 W, we observed the lowest temperature distributions, which were not sufficient to reach the melting point, a phenomenon that influences the consolidation of the particles and the final porosity of the built part, as seen in chapter 5. We observed that poor melted tracks are the main reason for the high porosity of the samples, and thus this condition is not recommended.

The substrate temperature analysis results match the claims made by some authors, such as Parry et al. and others [31], [86]–[88]. Amongst all the substrate temperatures, T_0 = 643K is the highest temperature recommended for use to eliminate residual stresses. Although 643 K is not a high temperature for the powder, it is valid to mention that if higher temperatures are applied to

the substrate, it can start the sintering of the powder. Sintering would cause each particle to start necking with its neighboring particles, thus affecting the surrounding areas of the scanned surface and degrading the surface finish quality and tolerances. For lower substrate temperatures, the maximum temperature achieved in the simulation will obviously decrease; however, the overall temperature gradient will actually increase. The reason behind this behavior is that less heat has accumulated in the powder bed, which means the laser heat flux is not penetrating all the way through, leading to a higher temperature gradient.

The experimental setup demonstrated all the claims presented in the previous chapter. However, we used another PBF technology, DMLS, to do so. The relative density is fairly efficient for analyzing the mechanical integrity of the samples, since relative density and porosity are closely associated. It was found that relative density follows a "bell curve," with samples having small relative densities also having small laser energy density, until relative density reached an optimum value, at which point the relative densities started to go down, even with high laser energy densities. The reason is the metal ejection of particles, gas bubbles, and vaporization of material, all of which happen only when high laser energy densities are applied.

To further reinforce the analysis, residual stresses measurements were performed next. The relationship between residual stresses and laser energy density was evident based on the analysis, but only for a range of values. In the mentioned range, the residual stresses increased with an increase in laser energy density. The parameter effects on the principal residual stresses, on the other hand, demonstrated that power input plays an important role. Power tended to increase the residual stresses independently of the combination of other parameters in most cases, further supporting power input as the most influential parameter.

6.2 Research Contributions

The proposed model has proved to be a flexible tool to investigate temperature distributions of PBF processes, with special attention given to the laser power input. New alloy employment can take advantage of this low-cost tool for pre-evaluation of optimal parameters to be used in the equipment. Important findings were obtained in the analytical formulation for effective thermal conductivity, as well as analysis of the sensitivity of powder packing density and diameter to the temperature field during laser scanning. The experimental setup for parameter evaluation showed that relative density measurements were good for the initial parameter analysis; however, the setup was not enough to assess how good a set of parameters it was, and further analysis should be considered. Using laser energy density, we were able to associate the three main parameters (power, scanning speed, and hatch distance) into one variable, making it easier to interpret the trends. We further analyzed the batch with X-ray diffraction measurements to obtain residual stresses and concluded that power input was the major variable responsible for bringing residual stresses into the printed part, thus increasing deformation and warpage and compromising its mechanical properties.

6.3 Future Research

We developed a thermal finite element model for the PBF manufacturing process that can be used for parametric evaluation of several parameters and sensitivity analysis. The future work listed below represents a complementary analysis to the findings presented here:

1. Measure effective thermal conductivity of a powder by experimental setup. This would be an interesting investigation to validate further the analytical model presented in chapter 3. Different scenarios, such as packing densities SC, BCC, or FCC, plus different powder

size distributions, as were proposed here, would bring more data to the scientific community.

2. Conduct monodispersed and polydispersed powder bed analysis to see the effects on the melt pool and final mechanical properties of the built part. Although it is a challenge to perform a setup with monodispersed beds, it would be interesting to see the effect of different levels of polydispersity of powder beds.
3. Develop a multi-track and multi-layer thermal FEM to study the effect of hatch distance and layers in the temperature gradients of the powder bed.
4. Implement a thermomechanical model to evaluate stress fields in different scenarios. For that, a proper solidification model that is able to account for shrinking volume would be ideal. Since the objective is to maintain a low computational cost, an uncoupled FEM is recommended.
5. Use the data acquired from finite element thermal models and imaging obtained from a built-in thermal camera to develop an integrated system that can identify undesirable temperature fields and inform the operator about the occurrence of high temperatures, as well as actively increase or decrease substrate temperature or gas flow.
6. Evaluate the effect of multiple lasers on the quality (i.e., mechanical properties) of the built part, as multiple manufacturers are using this process to increase productivity.

BIBLIOGRAPHY

[1] McCue, "Wohlers report 2016: 3D printing industry surpassed $5.1 billion," *Forbes*, 2016. [Online]. Available: https://www.forbes.com/sites/tjmccue/2016/04/25/wohlers-report-2016-3d-printer-industry-surpassed-5-1-billion/#2d631bbf19a0.

[2] M. Baumers, P. Dickens, C. Tuck, and R. Hague, "The cost of additive manufacturing: Machine productivity, economies of scale and technology-push," *Technol. Forecast. Soc. Change*, vol. 102, pp. 193–201, 2016.

[3] I. Gibson, D. Rosen, and B. Stucker, *Additive Manufacturing Technologies*. 2010.

[4] W. E. Frazier, "Metal additive manufacturing: A review," *J. Mater. Eng. Perform.*, vol. 23, no. 6, pp. 1917–1928, 2014.

[5] J. J. Beaman and C. R. Deckard, "Selective laser sintering with assisted powder handling," 02-Jul-1990.

[6] M. Shellabear and O. Nyrhilä, "DMLS – Development History and State of the Art," *Lane 2004*, pp. 1–12, 2004.

[7] ASTM International, "F2792-12a - Standard Terminology for Additive Manufacturing Technologies," *Rapid Manuf. Assoc.*, pp. 10–12, 2013.

[8] C. R. Deckard, J. J. Beaman, and J. F. Darrah, "Method for selective laser sintering with layerwise cross-scanning," 1990.

[9] C. Y. Yap *et al.*, "Review of selective laser melting: Materials and applications," *Appl. Phys.*

Rev., vol. 2, no. 4, 2015.

[10] "SLM Solutions Group AG." [Online]. Available: https://slm-solutions.com/. [Accessed: 30-Dec-2017].

[11] "Arcam AB." [Online]. Available: http://www.arcam.com/. [Accessed: 01-Apr-2017].

[12] M. Brandt, *The role of lasers in additive manufacturing*. Elsevier Ltd, 2001.

[13] M. Cotteleer, J. Holdowsky, M. Mahto, and J. Coykendall, "3D opportunity in aerospace and defense: Additive manufacturing takes flight | Deloitte Insights," 2014. [Online]. Available: https://www2.deloitte.com/insights/us/en/focus/3d-opportunity/additive-manufacturing-3d-opportunity-in-aerospace.html. [Accessed: 04-Aug-2018].

[14] X. Ren, J. Shen, A. Ghaedizadeh, H. Tian, and Y. Min Xie, "Experiments and parametric studies on 3D metallic auxetic metamaterials with tuneable mechanical properties," *Smart Mater. Struct.*, vol. 24, no. 9, p. 095016, Sep. 2015.

[15] "How 3D Printing Will Change Manufacturing - GE Reports." [Online]. Available: https://www.ge.com/reports/epiphany-disruption-ge-additive-chief-explains-3d-printing-will-upend-manufacturing/. [Accessed: 21-Jul-2018].

[16] "RAMLAB designs the first boat propeller using additive manufacturing - 3Dnatives." [Online]. Available: https://www.3dnatives.com/en/ramlab-boat-propeller110520174/. [Accessed: 21-Jul-2018].

[17] "Eos GmbH." [Online]. Available: https://eos.info.

[18] "Tool & Diemaker Adopting Metal Additive Manufacturing." [Online]. Available:

http://www.foundrymag.com/moldscores/tool-diemaker-adopting-metal-additive-manufacturing. [Accessed: 21-Jul-2018].

[19] "Modular prototype production of gas turbines." [Online]. Available: http://www.metal-am.com/modular-prototype-production-metal-additive-manufacturing-enables-faster-gas-turbine-development/. [Accessed: 21-Jul-2018].

[20] "Renishaw Manufacturing Systems." [Online]. Available: https://renishaw.com/. [Accessed: 30-Dec-2017].

[21] "Concept-laser." [Online]. Available: https://www.concept-laser.de/home.html. [Accessed: 03-May-2017].

[22] B. Song, S. Dong, S. Deng, H. Liao, and C. Coddet, "Microstructure and tensile properties of iron parts fabricated by selective laser melting," *Opt. Laser Technol.*, vol. 56, pp. 451–460, 2014.

[23] B. Sustarsic, S. Dolinsek, M. Jenko, and V. Leskovšek, "Microstructure and Mechanical Characteristics of DMLS Tool-Inserts," *Mater. Manuf. Process.*, vol. 24, no. 7–8, pp. 837–841, May 2009.

[24] Y. Wang, J. Bergström, and C. Burman, "Thermal fatigue behavior of an iron-based laser sintered material," *Mater. Sci. Eng. A*, vol. 513, pp. 64–71, 2009.

[25] H. K. Rafi, T. L. Starr, and B. E. Stucker, "A comparison of the tensile, fatigue, and fracture behavior of Ti–6Al–4V and 15-5 PH stainless steel parts made by selective laser melting," *Int. J. Adv. Manuf. Technol.*, vol. 69, no. 5–8, pp. 1299–1309, Nov. 2013.

[26] A. B. Spierings, T. L. Starr, and K. Wegener, “Fatigue performance of additive manufactured metallic parts,” *Rapid Prototyp. J.*, vol. 19, no. 2, pp. 88–94, Mar. 2013.

[27] K. Guan, Z. Wang, M. Gao, X. Li, and X. Zeng, “Effects of processing parameters on tensile properties of selective laser melted 304 stainless steel,” *Mater. Des.*, vol. 50, pp. 581–586, 2013.

[28] A. B. Spierings, N. Herres, and G. Levy, “Influence of the particle size distribution on surface quality and mechanical properties in AM steel parts,” *Rapid Prototyp. J.*, vol. 17, no. 3, pp. 195–202, Apr. 2011.

[29] K. Kempen, E. Yasa, L. Thijs, J.-P. Kruth, and J. Van Humbeeck, “Microstructure and mechanical properties of Selective Laser Melted 18Ni-300 steel,” *Phys. Procedia*, vol. 12, pp. 255–263, 2011.

[30] H. Fayazfar *et al.*, “A critical review of powder-based additive manufacturing of ferrous alloys: Process parameters, microstructure and mechanical properties,” *Mater. Des.*, vol. 144, pp. 98–128, Apr. 2018.

[31] P. Mercelis and J.-P. Kruth, “Residual stresses in selective laser sintering and selective laser melting,” *Rapid Prototyp. J.*, vol. 12, no. 5, pp. 254–265, 2006.

[32] A. Ahmadi, N. Shayesteh Moghaddam, M. Elahinia, H. E. Karaca, and R. Mirzaeifar, “Finite element modeling of selective laser melting 316L stainless steel parts for evaluating the mechanical properties,” in *Volume 2: Materials; Biomanufacturing; Properties, Applications and Systems; Sustainable Manufacturing*, 2016, pp. 1–5.

[33] K. Abd- Elghany and D. L. Bourell, “Property evaluation of 304L stainless steel fabricated by selective laser melting,” *Rapid Prototyp. J.*, vol. 18, no. 5, pp. 420–428, 2012.

[34] M. Yakout, A. Cadamuro, M. A. Elbestawi, and S. C. Veldhuis, “The selection of process parameters in additive manufacturing for aerospace alloys,” *Int. J. Adv. Manuf. Technol.*, vol. 92, no. 5–8, pp. 2081–2098, 2017.

[35] C. Li, T. Tsai, and C. Tseng, “Numerical simulation for heat and mass transfer during selective laser melting of titanium alloys powder,” *Phys. Procedia*, vol. 83, pp. 1444–1449, 2016.

[36] D. A. de Moraes, “Thermal modeling of 304L stainless steel for selective laser melting: Laser power input evaluation,” in *International Mechanical Engineering Congress and Exposition*, 2017, vol. 6061, pp. 1–10.

[37] L.-C. Zhang and H. Attar, “Selective laser melting of titanium alloys and titanium matrix composites for biomedical applications: A review,” *Adv. Eng. Mater.*, vol. 18, no. 4, pp. 463–475, Apr. 2016.

[38] L.-C. Zhang, Y. Liu, S. Li, and Y. Hao, “Additive manufacturing of titanium alloys by electron beam melting: A review,” *Adv. Eng. Mater.*, vol. 20, no. 5, p. 1700842, May 2018.

[39] Y. J. Liu *et al.*, “Microstructure, defects and mechanical behavior of beta-type titanium porous structures manufactured by electron beam melting and selective laser melting,” *Acta Mater.*, vol. 113, pp. 56–67, Jul. 2016.

[40] Y. J. Liu, Z. Liu, Y. Jiang, G. W. Wang, Y. Yang, and L. C. Zhang, “Gradient in

microstructure and mechanical property of selective laser melted AlSi10Mg," *J. Alloys Compd.*, vol. 735, pp. 1414–1421, Feb. 2018.

[41] E. R. Denlinger, V. Jagdale, G. V. Srinivasan, T. El-Wardany, and P. Michaleris, "Thermal modeling of Inconel 718 processed with powder bed fusion and experimental validation using in situ measurements," *Addit. Manuf.*, vol. 11, pp. 7–15, 2016.

[42] Y. Huang, L. J. Yang, X. Z. Du, and Y. P. Yang, "Finite element analysis of thermal behavior of metal powder during selective laser melting," *Int. J. Therm. Sci.*, vol. 104, pp. 146–157, 2016.

[43] K. Dai and L. Shaw, "Thermal and stress modeling of multi-material laser processing," *Acta Mater.*, vol. 49, no. 20, pp. 4171–4181, 2001.

[44] B. Cheng, S. Shrestha, and K. Chou, "Stress and deformation evaluations of scanning strategy effect in selective laser melting," *Addit. Manuf.*, vol. 12, no. May, pp. 240–251, 2015.

[45] G. Vastola, G. Zhang, Q. X. Pei, and Y. W. Zhang, "Controlling of residual stress in additive manufacturing of Ti6Al4V by finite element modeling," *Addit. Manuf.*, vol. Volume 12, pp. 231–239, 2016.

[46] Y. J. Liu, S. J. Li, L. C. Zhang, Y. L. Hao, and T. B. Sercombe, "Early plastic deformation behaviour and energy absorption in porous β-type biomedical titanium produced by selective laser melting," *Scr. Mater.*, vol. 153, pp. 99–103, Aug. 2018.

[47] L.-E. Loh *et al.*, "Numerical investigation and an effective modelling on the Selective Laser

Melting (SLM) process with aluminium alloy 6061," *Int. J. Heat Mass Transf.*, vol. 80, pp. 288–300, Jan. 2015.

[48] M. Yakout, M. A. Elbestawi, and S. C. Veldhuis, "On the characterization of stainless steel 316L parts produced by selective laser melting," *Int. J. Adv. Manuf. Technol.*, vol. 95, no. 5, pp. 1–22, 2017.

[49] D. de Moraes and A. Czekanski, "Parametric thermal FE analysis on the laser power input and powder effective thermal conductivity during selective laser melting of SS304L," *J. Manuf. Mater. Process.*, vol. 2, no. 3, p. 47, Jul. 2018.

[50] O. B. Kovalev and A. V. Gusarov, "Modeling of granular packed beds, their statistical analyses and evaluation of effective thermal conductivity," *Int. J. Therm. Sci.*, vol. 114, pp. 327–341, 2017.

[51] A. V. Gusarov and E. P. Kovalev, "Model of thermal conductivity in powder beds," *Phys. Rev. B - Condens. Matter Mater. Phys.*, vol. 80, no. 2, 2009.

[52] K. L. Johnson, *Contact Mechanics*. Cambridge: Cambridge University Press, 1985.

[53] S. Sumin Sih and J. W. Barlow, "The prediction of the emissivity and thermal conductivity of powder beds," *Part. Sci. Technol.*, vol. 22, no. 3, pp. 291–304, 2004.

[54] A. M. Abyzov, A. V. Goryunov, and F. M. Shakhov, "Effective thermal conductivity of disperse materials. I. Compliance of common models with experimental data," *Int. J. Heat Mass Transf.*, vol. 67, pp. 752–767, Dec. 2013.

[55] R. G.N. Dul'nev, Yu.P. Zarichnyak, *Teploprovodnost' smesei i kompozitzionnykh*

materialov [Thermal conductivity of mixtures and composites]. Leningrad, Russia, 1974.

[56] C. S. Kim, "Thermophysical Properties of Stainless Steels," Argonne National Laboratory, 1975.

[57] G. G. Gubareff, J. E. Janssen, and R. H. Torborg, *Thermal radiation properties survey: a review of the literature*, no. 2nd ed. 1960.

[58] N. Wakao and S. Kagei, *Heat and Mass Transfer in Packed Beds*. Taylor & Francis, 1982.

[59] G. a Gordeev, V. E. Ankudinov, M. D. Krivilyov, and E. V Kharanzhevskiy, "Optimisation of processing parameters in laser sintering of metallic powders," *IOP Conf. Ser. Mater. Sci. Eng.*, vol. 27, p. 012079, 2012.

[60] M. R. Alkahari, T. Furumoto, T. Ueda, A. Hosokawa, R. Tanaka, and M. S. Abdul Aziz, "Thermal Conductivity of Metal Powder and Consolidated Material Fabricated via Selective Laser Melting," *Key Eng. Mater.*, vol. 523–524, pp. 244–249, Nov. 2012.

[61] J. N. Reddy and D. K. Gartling, *The Finite Element Method in Heat Transfer and Fluid Dynamics*, 3rd Editio. Boca Raton, FL: CRC PressI LLC, 2010.

[62] H. Liu, "Numerical analysis of thermal stress and deformation in multi-layer laser metal deposition processes," Missouri University, 2014.

[63] V. A. Vinokurov, *Welding stresses and distortion : determination and elimination*. British Library Lending Division, 1977.

[64] J. Romano, L. Ladani, and M. Sadowski, "Laser Additive Melting and Solidification of Inconel 718: Finite Element Simulation and Experiment," *Jom*, vol. 68, no. 3, pp. 967–977,

2016.

[65] B. Cheng and K. Chou, "Melt Pool Geometry Simulations for Powder-Based Electron Beam Additive Manufacturing," *Proc. Solid Free. Fabr. Symp.*, pp. 644–654, 2013.

[66] S. Lynch, "Melt Pool Evolution Study in Selective Laser Melting," *Dyn. Syst. with Appl. using MATLAB*, vol. 53, pp. 1182–1194, 2013.

[67] J. Wu, L. Wang, and X. An, "Numerical analysis of residual stress evolution of AlSi10Mg manufactured by selective laser melting," *Optik (Stuttg).*, vol. 137, pp. 65–78, 2017.

[68] "Abaqus Documentation." [Online]. Available: http://50.16.225.63/.

[69] P. W. Fuerschbach, J. T. Norris, X. He, and T. Debroy, "Understanding metal vaporization from laser welding," Albuquerque, 2003.

[70] M. T. Andani, "Modeling , aimulation , additive Manufacturing , and experimental evaluation of solid and porous NiTi," The university of Toledo, 2015.

[71] I. A. Roberts, C. J. Wang, R. Esterlein, M. Stanford, and D. J. Mynors, "A three-dimensional finite element analysis of the temperature field during laser melting of metal powders in additive layer manufacturing," *Int. J. Mach. Tools Manuf.*, vol. 49, no. 12–13, pp. 916–923, 2009.

[72] J. Goldak, A. Chakravarti, and M. Bibby, "A new finite element model for welding heat sources," *Metall. Trans. B*, vol. 15, no. 2, pp. 299–305, 1984.

[73] E. R. Denlinger, J. Irwin, and P. Michaleris, "Thermomechanical modeling of additive manufacturing large parts," *J. Manuf. Sci. Eng.*, vol. 136, no. 6, p. 061007, 2014.

[74] P. Michaleris, “Modeling metal deposition in heat transfer analyses of additive manufacturing processes,” *Finite Elem. Anal. Des.*, vol. 86, pp. 51–60, 2014.

[75] V. Nikolaos, “Linking Abaqus 6.13 / 6.12 With Intel Fortran Compiler And Microsoft Visual Studio (64-Bit Architecture Systems Only),” no. December, pp. 1–8, 2014.

[76] Z. Fan, “Numerical modeling of heat transfer and fluid flow in laser metal deposition by powder injection,” Missouri University, 2013.

[77] B. Brown, “Characterization of 304L stainless steel by means of minimum input energy on the selective laser melting platform,” Missouri University, 2015.

[78] D.-H. Cho, “Determining the temperature field of selective laser melting process for different heat source paths,” Northeastern University, 2016.

[79] X. P. Li, M. Roberts, Y. J. Liu, C. W. Kang, H. Huang, and T. B. Sercombe, “Effect of substrate temperature on the interface bond between support and substrate during selective laser melting of Al–Ni–Y–Co–La metallic glass,” *J. Mater.*, vol. 65, pp. 1–6, 2015.

[80] T. M. Mower and M. J. Long, “Mechanical behavior of additive manufactured, powder-bed laser-fused materials,” *Mater. Sci. Eng. A*, vol. 651, pp. 198–213, Jan. 2016.

[81] M. Ghasri-Khouzani *et al.*, “Direct metal laser-sintered stainless steel: comparison of microstructure and hardness between different planes,” *Int. J. Adv. Manuf. Technol.*, vol. 95, no. 9–12, pp. 4031–4037, 2018.

[82] D. D. Gu, W. Meiners, K. Wissenbach, and R. Poprawe, “Laser additive manufacturing of metallic components: materials, processes and mechanisms,” *Int. Mater. Rev.*, vol. 57, no.

3, pp. 133–164, 2012.

[83] S. W. Hughes, "Archimedes revisited: a faster, better, cheaper method of accurately measuring the volume of small objects," *Phys. Educ.*, vol. 40, no. 5, pp. 468–474, Sep. 2005.

[84] ASTM International, "Standard Test Methods for Density of Compacted or Sintered Powder Metallurgy (PM) Products Using Archimedes' Principle," *Astm B962-13*, vol. i, pp. 1–7, 2013.

[85] M. E. Fitzpatrick, A. T. Fry, P. Holdway, F. A. Kandil, J. Shackleton, and L. Suominen, "Determination of Residual Stresses by X-ray Diffraction - Issue 2," Teddington, UK, 2005.

[86] L. Parry, I. A. Ashcroft, and R. D. Wildman, "Understanding the effect of laser scan strategy on residual stress in selective laser melting through thermo-mechanical simulation," *Addit. Manuf.*, vol. 12, pp. 1–15, 2016.

[87] M. Simonelli, Y. Y. Tse, and C. Tuck, "On the Texture Formation of Selective Laser Melted Ti-6Al-4V," *Metall. Mater. Trans. A*, vol. 45, no. 6, pp. 2863–2872, Jun. 2014.

[88] N. T. Aboulkhair, N. M. Everitt, I. Ashcroft, and C. Tuck, "Reducing porosity in AlSi10Mg parts processed by selective laser melting," *Addit. Manuf.*, vol. 1–4, pp. 77–86, Oct. 2014.

APPENDIX

Abaqus Subroutine DFLUX and FILM

```
      SUBROUTINE DFLUX(FLUX,SOL,JSTEP,JINC,TIME,NOEL,NPT,COORDS,JLTYP,
     1    TEMP,PRESS,SNAME)

      INCLUDE 'ABA_PARAM.INC'
      DIMENSION COORDS(3),FLUX(2),TIME(2)
      CHARACTER*80 SNAME
      DOUBLE PRECISION af,ar,b,c,P,v,df,dr
      FLUX(1)=0
      P=6*0.4*200*1.732
      x0=0.00
      y0=0.00
      z0=0.000075

      x1=0.0015
      y1=0.0015
      z1=0

      pi=3.14159
      v=1
      b=0.00012
      c=0.00015
      af=0.00006
      ar=0.00022
      d=v*TIME(1)-COORDS(1)
      e=v*TIME(1)-COORDS(2)
      df=exp(-3*(((d)**2/af**2)+((COORDS(2))**2
     $   /b**2)+((COORDS(3))**2/c**2)))
      dr=exp(-3*(((d)**2/ar**2)+((COORDS(2))**2
     $   /b**2)+((COORDS(3))**2/c**2)))

      if(JSTEP.eq.1) then
        if((COORDS(1).ge.(v*TIME(1))).and.(COORDS(1).ge.0.000)
     $                                .and.(COORDS(1).le.0.0015))    then
         FLUX(1)=P*df*0.6/(pi*(c*b*af)*sqrt(pi))
         endif
        if((COORDS(1).le.(v*TIME(1))).and.(COORDS(1).ge.0.00)
     $                               .and.(COORDS(1).le.0.0015))    then
         FLUX(1)=P*dr*1.4/(pi*(c*b*ar)*sqrt(pi))
         endif

      RETURN
      END SUBROUTINE DFLUX


       SUBROUTINE FILM(H,SINK,TEMP,KSTEP,KINC,TIME,NOEL,NPT,
     1 COORDS,JLTYP,FIELD,NFIELD,SNAME,NODE,AREA)

      INCLUDE 'ABA_PARAM.INC'
      DIMENSION H(2),TIME(1),COORDS(3),FIELD(NFIELD)
      CHARACTER*80 SNAME

      SINK=643
      H(1)=0.001362132*(TEMP**1.61)      ! Film coefficient (Emiss=0.5652)
      H(2)=0.00219303*(TEMP**0.61)       ! Rate of change of the film coefficient (Emiss=0.5652)
      RETURN
      CONTINUE
      END
```

Input File of Abaqus

```
*Heading
** Job name: P=100-20micro-BCC Model name: Job-2
** Generated by: Abaqus/CAE 2016
*Preprint, echo=NO, model=NO, history=NO, contact=NO
**
** PARTS
**
*Part, name=PART-1-1
*Node
 1,          0., -0.000750000007,  7.50000036e-05
 2,          0., -0.000724999991,  7.50000036e-05
 3,          0., -0.000699999975,  7.50000036e-05
 4,          0., -0.000675000018,  7.50000036e-05
....
....
*End Assembly
**
** MATERIALS
**
*Material, name=POWDER_FCC
*Conductivity
0.007200104939668,300
0.008099424137992,400
0.008998743336316,500
0.009892511181564,600
0.010791830379888,700
0.011691149578212,800
0.012590468776537,900
0.013489787974861,1000
0.014383555820109,1100
0.015282875018433,1200
0.016182194216757,1300
0.017081513415081,1400
0.017980832613405,1500
0.018874600458653,1600
0.019801676422357,1703
17.92,1733.
18.14,1800.
18.46,1900.
18.79,2000.
19.11,2100.
19.44,2200.
19.76,2300.
20.09,2400.
```

20.41,2500.
20.73,2600.
21.06,2700.
21.38,2800.
*Density
7894., 300.
7860., 400.
7823., 500.
7783., 600.
7742., 700.
7698., 800.
7652., 900.
7603.,1000.
7552.,1100.
7499.,1200.
7444.,1300.
7386.,1400.
7326.,1500.
7264.,1600.
7197.,1703.
6905.,1733.
6862.,1800.
6795.,1900.
6725.,2000.
6652.,2100.
6576.,2200.
6498.,2300.
6416.,2400.
6331.,2500.
6243.,2600.
6152.,2700.
6058.,2800.
*Latent Heat
273790.,1703.,1733.
*Specific Heat
510.03, 300.
523.42, 400.
536.81, 500.
550.2, 600.
564., 700.
577.39, 800.
590.78, 900.
604.17,1000.
617.56,1100.
631.37,1200.
644.75,1300.

```
658.14,1400.
671.53,1500.
685.34,1600.
698.73,1703.
794.96,1733.
794.96,1800.
794.96,1900.
794.96,2000.
794.96,2100.
794.96,2200.
794.96,2300.
794.96,2400.
794.96,2500.
794.96,2600.
794.96,2700.
794.96,2800.
*Material, name="Steel plate (Sub)"
*Conductivity
 11.5,
*Density
5700.,
**
** INTERACTION PROPERTIES
**
*Film Property, name=INTPROP-1
10.
**
** PHYSICAL CONSTANTS
**
*Physical Constants, absolute zero=-273.15, stefan boltzmann=5.67e-08
**
** PREDEFINED FIELDS
**
** Name: Field-1   Type: Temperature
*Initial Conditions, type=TEMPERATURE
_PICKEDSET62, 300.
** ----------------------------------------------------------------
**
** STEP: Step-1
**
*Step, name=Step-1, nlgeom=NO, inc=1000
*Heat Transfer, end=PERIOD
0.0000015, 0.0015, , ,
**
** LOADS
**
```

```
** Name: BODYFLUX-1   Type: Body heat flux
*Dflux
PART-1-1.SET-1, BFNU, 1.
**
** INTERACTIONS
**
** Interaction: SURFFILM-1
*Sfilm
_PICKEDSURF60, FNU, 300., 1.
** Interaction: SURFRADIATE-1
*Sradiate
SURF-4, AVG, 0.0, 0.5652
**
** CONTROLS
**
*Controls, reset
*Controls, parameters=time incrementation
8, 10, , , , , , , , ,
*Controls, parameters=field, field=temperature
0.05, 0.5, , , , , ,
**
** OUTPUT REQUESTS
**
*Restart, write, frequency=0
**
** FIELD OUTPUT: F-Output-1
**
*Output, field
*Node Output
NT,
**
** FIELD OUTPUT: F-Output-2
**
*Node Output, nset=Middle
NT,
**
** FIELD OUTPUT: F-Output-3
**
*Node Output, nset=Surface
NT,
**
** FIELD OUTPUT: F-Output-4
**
*Node Output, nset=Surface-25
NT,
**
```

```
** FIELD OUTPUT: F-Output-5
**
*Node Output, nset=Surface-50
NT,
**
** FIELD OUTPUT: F-Output-6
**
*Node Output, nset=Middle-25
NT,
**
** FIELD OUTPUT: F-Output-7
**
*Node Output, nset=Middle-50
NT,
**
** FIELD OUTPUT: F-Output-8
**
*Node Output, nset=Middle-75
NT,
**
** FIELD OUTPUT: F-Output-9
**
*Node Output, nset=Bottom
NT,
**
** HISTORY OUTPUT: H-Output-2
**
*Output, history
*Radiation Output
FTEMP, RADFL, RADFLA, RADTL, RADTLA, VFTOT
**
** HISTORY OUTPUT: H-Output-1
**
*Contact Output
HFLA, HTL, HTLA, SJD, SJDA, SJDT, SJDTA, WEIGHT
*End Step
```